

Detecting Spatial Health Disparities Using Disease Maps

Luca Aiello*, Sudipto Banerjee†

Abstract

Epidemiologists commonly use regional aggregates of health outcomes to map mortality or incidence rates and identify geographic disparities. An approach to detect health disparities between regions is to identify “difference boundaries” that separate neighboring regions with significantly different spatial effects. With growing interest in studying disparities across multiple outcomes, cancer rates in California in the current investigation, we turn to accounting for dependence among diseases and across regions. We address detecting multivariate difference boundaries for possibly correlated diseases using a Bayesian nonparametric approach to balance smoothing with disparities across geographical neighbors. Specifically, we estimate posterior probabilities of neighboring spatial effects being different using multivariate Dirichlet process models that introduce spatial and inter-disease dependence. The model endows spatial effects with discrete probability laws, which allows control of false discoveries. We evaluated inferential performance using simulation studies over graphical model-based cancer dependencies. We detect difference boundaries for four cancers using data from the Surveillance, Epidemiology, and End Results Program of the National Cancer Institute.

Keywords — Difference Boundary Analysis; Disease mapping; False discovery rates; Spatial Dirichlet Processes; Spatial epidemiology.

1 Introduction

Health disparities, or inequities, broadly refer to sections of the population being deprived of fair and equal opportunities to seek healthcare or exhibiting different disease incidences and risks (see, e.g., the recent text by Rao, 2023). Spatial disparities in health manifest as variations in health outcomes in geographic regions and are often visually represented using disease maps (Koch, 2005). Spatial data analysis in epidemiological investigations is extensively documented (see, e.g., Waller and Gotway, 2004; Waller and Carlin, 2010; Lawson, 2013; Lawson et al., 2016, and further references therein). Detecting “boundaries” on disease maps is a

*Department of Economics, University of Bergamo, Italy, luca.aiello@unibg.it

†Department of Biostatistics, University of California, Los Angeles

specialized exercise directly relevant to the evaluation of health disparities. In public health, such *difference boundaries*, or *wombling boundaries* (so called after Womble, 1951), indicate significantly different disease mortality and incidence between neighbors and assist in decision making for disease prevention and control, geographic allocation of resources, etc. (see Jacquez and Greiling, 2003b,a; Lu and Carlin, 2005; Li et al., 2011; Ma and Carlin, 2007; Fitzpatrick et al., 2010, for some algorithmic approaches with applications). Model-based approaches aiming for full probabilistic uncertainty quantification have also received attention and include, but are not limited to, developments in Lu et al. (2007); Ma et al. (2010); Li et al. (2015, 2012); Hanson et al. (2015); Corpas-Burgos and Martinez-Beneito (2020); Gianella et al. (2023); Gao et al. (2023), and Pavani and Quintana (2024).

This manuscript builds on the above developments in what may be described as still a fledgling area. We devise a probabilistic learning mechanism for adjacency boundaries on a map when such information may become available. An administrative or political boundary separating two adjacent regions need not delineate them in terms of the health outcomes measured there. In fact, in spatial smoothing the customary approach is to assume that neighboring regions are similar to each other. This assumption runs counter to detecting health disparities, where we seek differences and not similarities. Therefore, modeling spatial disparities needs to balance the underlying processes that generate similarities based on geographic proximity with the processes that generate significant differences between neighbors. We specifically seek an effective manner of modeling the adjacency relations on a map. Our contribution is summarized in the context of the two broad themes. The first builds stochastic models for adjacency matrices (Lu et al., 2007; Ma et al., 2010; Lee and Mitchell, 2012; Liang, 2019; Corpas-Burgos and Martinez-Beneito, 2020) that, in principle, can accommodate information from explanatory variables to determine the presence of edges. Based upon the complexity of the resulting models and numerical difficulties in estimating such edges, a different approach forgoes introducing variables in the adjacency, but detects edges using multiple comparisons by estimating the spatial random effects and, subsequently, testing how many such pairs are significantly different. A Bayesian approach (Li et al., 2012, 2015; Gao et al., 2023) holds appeal as the posterior distribution of spatial effects produces an exact Bayesian false discovery rate (FDR, Müller et al., 2004) without recourse to asymptotic assumptions that are inappropriate in areal settings.

We offer a framework that melds the two themes. We build on Gao et al. (2023) embedding directed acyclic graphical autoregression (DAGAR) models (Datta et al., 2019) within a hierarchical Bayesian non-parametric framework. This nonparametric specification is critical as it introduces discrete probability masses on the spatial random effects and allows us to meaningfully calculate the posterior probabilities of two neighboring spatial effects being equal. This sets up boundary detection using Bayesian FDR. We further enrich the model by allowing the DAGAR adjacency matrix to learn from explanatory variables that may carry information regarding whether two neighboring regions are similar. Thus, each element of a binary adjacency matrix is modeled using an exponential threshold devised by Lee and Mitchell (2012). We develop joint models for multiple diseases (cancers), where the diseases are associated with each other and allow disease-specific learning of adjacency relationships. We allow difference

boundaries to vary by health outcomes and explain the impact of explanatory variables on such boundaries. Here, we consider unstructured disease dependencies and those posited by conditional dependencies in graphical models.

The data analytic innovation and merits of our approach are best appreciated in comparison to approaches that adhere to one, but not both, of the boundary detection themes discussed above. Methods that allow uncertainty through purely parametric adjacency relations (including regression models for adjacency matrices) within widely used conditional autoregression models often encounter numerical difficulties in convergence of iterative estimation algorithms, such as Markov chain Monte Carlo (MCMC). On the other hand, methods offering FDR based boundary detection without allowing adjacency learning from explanatory variables can lead to inflated detection rates of boundaries by failing to account for additional uncertainties in adjacency relations. We demonstrate this phenomenon in the cancer boundary detection rates reported recently by Gao et al. (2023).

The article develops as follows. Section 2 describes the data of interest. These data, extracted from the National Cancer Institute (NCI) Surveillance Epidemiology and End Results (SEER) database, record the occurrences of four different types of cancer in California counties, together with explanatory variables to model results and boundaries. Section 3 develops our multivariate Bayesian modeling framework using an areal stick-breaking process with a DA-GAR spatial distribution as its baseline measure for modeling difference boundaries. Section 4 presents simulation experiments to obtain information on the performance of our proposed model using various metrics. Section 5 applies spatial boundary detection to the SEER dataset, and we conclude with some remarks in Section 6. In the end, additional modeling and computational details, as well as results from simulation studies and data analyses, are provided in the appendices.

2 Multiple Cancer Data

We explore an areal data set extracted from the SEER*Stat database using the SEER*Stat statistical software (National Cancer Institute, 2019). The data record the occurrence of four potentially interrelated types of cancers: lung, esophageal, larynx, and colorectal. The occurrences of these cancers are aggregated from January 2012 through December 2016 and are presented as counts in each of the 58 counties of California. Previous research has shown that lung and esophageal cancers share common risk factors (Agrawal et al., 2018) and metabolic mechanisms (Shi and Chen, 2004). Furthermore, it has been found that lung cancer is one of the second most common primary cancers in patients with colon cancer (Kurishima et al., 2018). Patients with laryngeal cancer are also at high risk for developing a second primary lung cancer (Akhtar et al., 2010). Hence, we seek to account for the dependence between the cancers due to non-spatial factors.

Let (y_{id}) be the observed counts for cancer type d ($d = 1, 2, 3, 4$) in county i ($i = 1, 2, \dots, 58$). Our model, developed in Section 3, accounts for the expected number of cases (E_{id}) by adjusting for demographics of age and sex in each county. Specifically, we calculate the expected age-sex

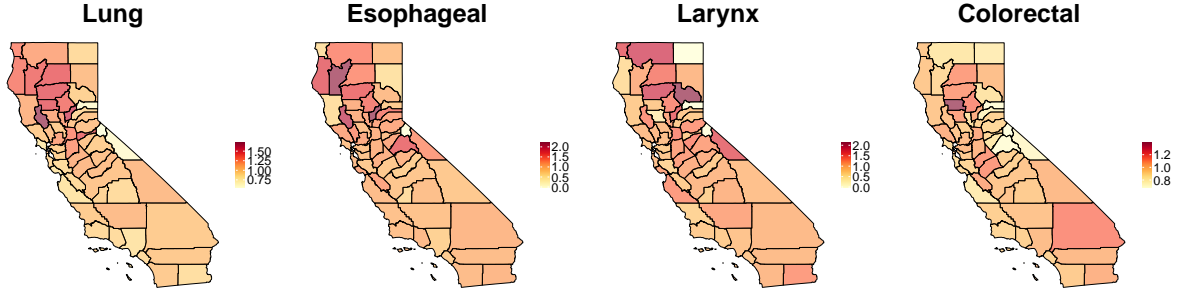


Figure 1: Maps of age-sex adjusted standardized incidence ratios (SIR) for lung, esophageal, larynx, and colorectal cancer in counties of California, 2012–2016.

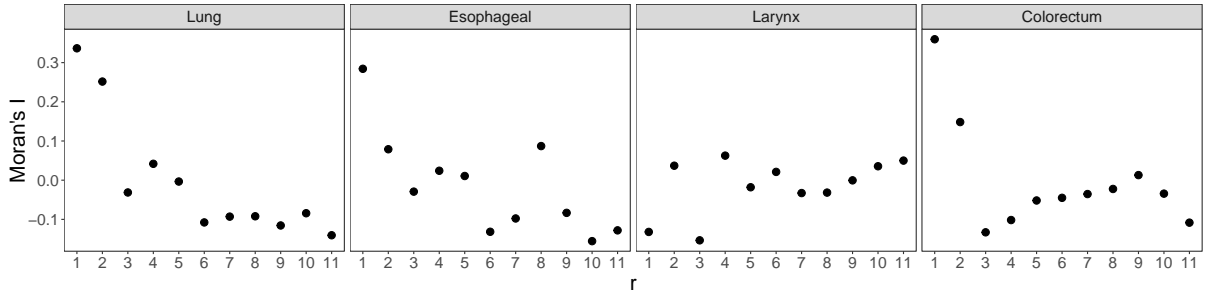


Figure 2: Moran's I statistic using r -th order neighbors for four cancers.

adjusted number of cases in county i for cancer d as $E_{id} = \sum_{k=1}^m c_d^k N_i^k$ (Jin et al., 2005), where $c_d^k = (\sum_{i=1}^{58} y_{id}^k) / (\sum_{i=1}^{58} N_i^k)$ is the age-specific incidence rate in the age-sex group k for cancer d in all California counties; y_{id}^k represents the incidence count in age-sex group k of county i for cancer d , and N_i^k represents the population in age-sex group k of county i . The age groups have been determined based on 5-year intervals up to 85 years or older. These age intervals are: less than 1 year, 1–4 years, 5–7 years, 10–14 years, etc., up to 80–84 years and 85+ years. This results in $m = 19 \times 2 = 38$ age-sex groups.

Figure 1 displays a map of California's counties, illustrating the age-sex adjusted standardized incidence ratios ($SIR_{id} = y_{id}/E_{id}$) for different types of cancer. The map reveals a notable pattern, in which regions exhibiting comparable SIRs tend to cluster geographically, forming distinct groups. This clustering is evident in the group of regions with the highest incidence rates for each cancer. The high SIR values for all types of cancer are concentrated in northern counties, with the only exception being the high SIR for colorectal cancer in a southern county (San Bernardino). Furthermore, in northern counties, we notice that several counties with high SIRs are located next to areas with low SIRs. Our proposed model, which detects boundaries, provides a robust, adaptable, interpretable, and clear analytical tool to identify these geographical clusters.

We used Pearson's correlation coefficient as an exploratory tool to evaluate the relationships between various types of cancer. In a preliminary analysis, we treated SIRs from different counties as independent samples. Our findings indicate a significant association in the incidence of lung cancer with each of esophageal (correlation coefficient 0.58), larynx (0.40), and colorectal (0.50) cancers. We also measured a correlation coefficient of 0.42 between esophageal and larynx

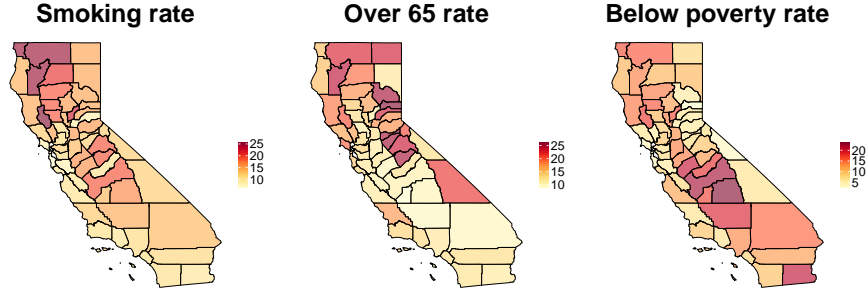


Figure 3: California’s county-level rates (as percentages of population) for smokers, elderly population (over 65) and individuals below poverty line in terms of annualized income.

cancer. Moreover, to assess the spatial relationships of each cancer type, we employed the Moran’s I statistic, which was computed based on the r -th order neighbors for each cancer. These calculations were then used to generate an areal correlogram, as described by Banerjee et al. (2014). Here, we construct 11 distance intervals or bins $(0, d_1], (d_1, d_2], (d_2, d_3], \dots$ using each $d_r = 0.01 \times r$ for $r = 1, \dots, 11$. We compute Euclidean distances between the county centroids from an Albers map projection of California and define r -th order neighbors as regions that fall within the bin $(d_{r-1}, d_r]$ of each other, i.e., they are separated by a distance greater than d_{r-1} but within a distance of d_r . These neighbors are then used to calculate Moran’s I statistic. Figure 2 shows the spatial associations for lung, esophageal, colorectal, and larynx cancers. As the order of neighbors (r) increases, spatial associations diminish notably for lung, esophageal, and colorectal cancers, but the observed pattern is less pronounced and clear for larynx cancer.

We introduce explanatory variables into our model to allow capturing the mean structure, accounting for risk factors, and identifying neighboring areas with significant differences in rates. A detailed analysis is presented in Section 5. Figure 3 presents the rates (in percentage scale) for smoking; population over 65; and below the poverty threshold rates for each county, organized from left to right. These plots reveal notable patterns: northern counties exhibit a higher concentration of smoking rates, with a few exceptions in central counties; both northern and eastern counties have higher rates of individuals over 65; and the northern and central counties have higher rates below the poverty threshold. In contrast, coastal regions demonstrate relatively lower rates in all covariates, indicating a distinct contrast between different geographical areas (see Doll et al., 2005, for similar findings). Interestingly, central and southern counties exhibit lower rates specifically in the over 65 variable. The significance and implications of these findings are discussed in Section 5.

3 Model Development

We construct a generalized linear mixed model for the disease outcome, y_{id} , using a distribution from the exponential family with a canonical link,

$$g(E(y_{id})) = \mathbf{x}_{id}^T \boldsymbol{\beta}_d + \phi_{id}, \quad (1)$$

for each areal unit $i = 1, \dots, n$ and disease $d = 1, \dots, q$. The large-scale trend is modeled using a regression, where \mathbf{x}_{id} is a vector of explanatory variables and $\boldsymbol{\beta}_d$ is the corresponding vector of slopes, while ϕ_{id} is the spatial random effect for disease d in region i . For detecting difference boundaries, we seek $P(\phi_{id} \neq \phi_{jd} | \mathbf{y}, i \sim j)$, which offers a fully model-based stochastic mechanism to calibrate difference boundaries Li et al. (2015), where \mathbf{y} is the collection of observed y_{id} 's and $i \sim j$ means that the regions i and j are neighbors. This approach also allows posterior probabilities to be interpreted as measures of uncertainty, indicating the chance that a difference between random effects occurs. While risks tend to fluctuate continuously across space, neighboring regions may exhibit discontinuities attributable to disparities arising from vastly different underlying factors (e.g., socioeconomic characteristics). This raises an issue about the prior distribution for the ϕ_{id} 's. A continuous probability distribution is inappropriate because $P(\phi_{id} \neq \phi_{jd} | \mathbf{y}, i \sim j) = 1$, which classifies all possible geographic boundaries as difference boundaries. This limitation underscores the need for a model that incorporates spatial dependence while assigning discrete probability masses to the spatial random effects. By assigning nonzero probabilities to the equality of random effects, such a model ensures in our approach that fewer boundaries are detected than the number of areas, n . The Dirichlet Process (DP) offers a natural way to cluster regions by endowing possibly positive mass on $P(\phi_{id} = \phi_{jd} | \mathbf{y}, i \sim j)$. The DP is especially appealing here as it still captures spatial associations in ϕ_{id} through the baseline covariance matrix. The model we develop here belongs to a subclass of stick-breaking process priors and includes the DP as a special instance.

3.1 Spatial Random Effects

Let $\boldsymbol{\phi} = (\boldsymbol{\phi}_1^T, \dots, \boldsymbol{\phi}_q^T)^T$ be the $N \times 1$ vector, where $N = nq$ and $\boldsymbol{\phi}_d = (\phi_{1d}, \dots, \phi_{nd})^T$ for each $d = 1, \dots, q$. Following Gao et al. (2023) we let $\{1, \dots, n, \dots, (q-1)n+1, \dots, N\}$ be an enumeration of the pairwise (i, d) indices corresponding to the ordering of $\boldsymbol{\phi}$, thereby dealing with a unique $N \times 1$ vector $\boldsymbol{\phi}$. We let $\boldsymbol{\phi} \sim G_N$, where G_N is an unknown distribution further specified by $G_N = \sum_{u_1, \dots, u_N} \pi_{u_1, \dots, u_N} \delta_{(\theta_{u_1}, \dots, \theta_{u_N})}$, where $u_1, \dots, u_N \in \{1, \dots, K\}$, $\theta_k | \tau \stackrel{iid}{\sim} \mathcal{N}(0, 1/\tau)$ for $k = 1, \dots, K$, $\delta_{(\theta_{u_1}, \dots, \theta_{u_N})}$ is the Dirac measure at $(\theta_{u_1}, \dots, \theta_{u_N})$ and

$$\pi_{u_1, \dots, u_N} = P \left(\sum_{k=1}^{u_1-1} p_k < F^{(1)}(\gamma_1) < \sum_{k=1}^{u_1} p_k, \dots, \sum_{k=1}^{u_N-1} p_k < F^{(N)}(\gamma_N) < \sum_{k=1}^{u_N} p_k \right)$$

with $\boldsymbol{\gamma} \sim \mathcal{N}_N(\mathbf{0}, \boldsymbol{\Sigma}_\boldsymbol{\gamma})$. The choice of i.i.d. atoms for the base distribution is driven by the need to establish ties across regions and cancers. Assigning different means to each cancer would

allow ties within regions but prevent ties across cancers, as the underlying base distribution would differ.

Priors for model parameters are specified as $\beta_d \stackrel{iid}{\sim} \mathcal{N}(\mathbf{0}, \Sigma_{\beta_d})$, while the variance $1/\tau \sim IG(a, b)$, where a is shape and b is scale. We specify the stick-breaking weights by $p_1 = V_1$ and $p_j = V_j \prod_{k < j} (1 - V_k)$ for $j = 2, \dots, K$, where $V_k \stackrel{iid}{\sim} Beta(1, \alpha)$ and $F^{(1)}(\cdot), \dots, F^{(N)}(\cdot)$ are cumulative distribution functions of the marginal distribution of the corresponding γ elements indexed in accordance with the elements of ϕ .

The weights in the distribution G_N are constructed by utilizing the marginal cumulative distribution function of the elements of γ . This construction combines two approaches: the hybrid Dirichlet process (Petroni et al., 2009), which involves the use of point-referenced continuous spatial copulas to model weight dependency, and the latent stick-breaking process (Rodríguez et al., 2010), which employs ordered atoms. Marginally, each $F^{(\cdot)}(\gamma_{\cdot})$ is $\mathcal{U}(0, 1)$ but they are dependent through the joint distribution of γ , and the distribution of each spatial random effect ϕ is a regular univariate DP, with the spatial dependence between these DPs introduced using a copula representation for the weights. In theory, $K = \infty$ yields a fully non-parametric model, but we follow the standard practice of replacing the infinite sum with the sum of the initial K ($K \leq n$) terms, as the probability masses diminish rapidly. Should concerns about truncation bias arise, an alternative method called slice-sampling (described in Kalli et al., 2011) is available for exact sampling. In particular, for areal data the value of K is naturally constrained by the number of areal units rendering the infinite representation redundant. See Müller et al. (2015) for further details on nonparametric models and their scope of inference.

The marginal covariance between spatial random effects ϕ_g and ϕ_h can be expressed as

$$\text{Cov}(\phi_g, \phi_h) = \frac{b}{a-1} \sum_{k=1}^K \pi_{kk}^{(g,h)}, \quad (2)$$

where $g, h = 1, \dots, N$ and

$$\pi_{kk}^{(g,h)} = P \left(\sum_{t=1}^{k-1} p_t < F^{(g)}(\gamma_i) < \sum_{t=1}^k p_t, \sum_{t=1}^{k-1} p_t < F^{(h)}(\gamma_j) < \sum_{t=1}^k p_t \right) \quad (3)$$

Equation (2) and (3) evinces how the spatially dependent elements of γ induce associations among the elements of ϕ . The covariance of ϕ also depends on the hyperparameters of the precision parameter prior of the base distribution. Higher values of the probabilities, i.e., $\pi_{kk}^{(g,h)}$, produce higher correlation between the random effects. Unsurprisingly, a higher likelihood of ϕ_g and ϕ_h exhibiting similar values implies a higher covariance in (2). Before modeling the full covariance matrix Σ_{γ} , we first introduce the spatial dependence model.

3.2 DAGAR Adjacency Modeling

To model spatial dependence, we use the DAGAR model, which is particularly appealing due to its inclusion of a proper spatial autocorrelation parameter, setting it apart from traditional models like Simultaneous (SAR) and Conditional Autoregressive (CAR) models. However, as

discussed in Section A of the appendices, where we review the DAGAR model, it remains unclear how information from explanatory variables, predictors, or risk factors can be incorporated into the adjacency structure. We achieve this by constructing a strictly lower triangular $n \times n$ adjacency matrix, $\widetilde{\mathbf{W}} = (w_{ij})$ based upon the fixed topological order of regions to assimilate information from preceding neighboring regions. This results in $w_{ij} = 0$ for $i \leq j$ or $i \not\sim j$ (i and j not neighbors). Hence, for each region i , its neighbors are $\{j : j < i, j \sim i\} \equiv \{j : w_{ij} = 1\}$. Introducing $\widetilde{\mathbf{W}}$ into the DAGAR precision matrix is then straightforward. Specifically,

$$\mathbf{Q}(\rho, \widetilde{\mathbf{W}}) = (\mathbf{I} - \mathbf{B})^T \boldsymbol{\Lambda} (\mathbf{I} - \mathbf{B})$$

where $\mathbf{B} = \widetilde{\mathbf{B}} \circ \widetilde{\mathbf{W}}$, $\widetilde{\mathbf{B}} = (\widetilde{b}_{ij})$ with elements $\widetilde{b}_{ij} = \rho / (1 + (n_{<i} - 1)\rho^2)$, $\lambda_i = (1 + (n_{<i} - 1)\rho^2) / (1 - \rho^2)$, $n_{<i} = \sum_{j=1}^n w_{ij}$ and \circ denotes the Hadamard (or elementwise) product.

The matrix $\widetilde{\mathbf{B}}$ is dense with all its elements being possibly non-zero. However, $\widetilde{\mathbf{B}} \circ \widetilde{\mathbf{W}}$ retains the sparse lower-triangular structure characteristic of DAGAR. Instead of directly setting the non-null elements of $\widetilde{\mathbf{W}}$ to fixed values, one possibility is to model each element of $\widetilde{\mathbf{W}}$ as a separate random quantity. For instance, Lu et al. (2007) employed a logistic model for the elements of a symmetric adjacency matrix in a CAR model while considering boundary-specific risk factors. In our DAGAR setting, a parallel approach would be to model the lower triangular elements $\widetilde{w}_{ij} | p_{ij} \stackrel{\text{ind}}{\sim} \text{Bernoulli}(p_{ij})$ and introducing a regression model in, for example, a logistic link $\log(p_{ij}/(1 - p_{ij}))$. Other possible approaches include adapting random adjacency models, such as in Ma et al. (2010), to DAGAR by leveraging an Ising model for elements of the adjacency. However, the information needed to estimate such models is rarely available and require informative prior distributions resulting in excessively parametrized covariance models for $\boldsymbol{\gamma}$ that inaccurately estimate uncertainties and produce biased inference for spatial boundaries (also see Li et al., 2011, who argue that effectively modeling geographical adjacency would require a separate parameter for every pair of neighbors resulting in overparametrized models).

In what follows, we adopt a simpler and more effective approach based on Lee and Mitchell (2012), who propose modeling the adjacency matrix as

$$\widetilde{w}_{ij}(\boldsymbol{\eta}) = \begin{cases} 1 & \text{if } \exp(-\mathbf{z}_{ij}^T \boldsymbol{\eta}) \geq 0.5 \text{ and } i \sim j \\ 0 & \text{otherwise,} \end{cases} \quad (4)$$

where \mathbf{z}_{ij} consist of explanatory variables specific to pairs of regions i and j and are assumed to be non-negative in each element. In practice, they could represent an absolute measure of discrepancy between the two regions with $\boldsymbol{\eta}$ being the vector of corresponding coefficients. Equation (4) encodes geographic neighbors so as to not represent disparities whenever $\mathbf{z}_{ij}^T \boldsymbol{\eta} \leq \log 2$. Furthermore, \mathbf{z}_{ij} excludes an intercept so regions with homogeneous populations, i.e., $\mathbf{z}_{ij} = \mathbf{0}$, are deemed adjacent. The coefficients in $\boldsymbol{\eta}$ act as disparity parameters and restricted to be nonnegative so the greater the dissimilarity between two regions, the more likely there is a difference boundary between them. Each element in $\boldsymbol{\eta}$ is assigned a Uniform prior distribution between 0 and a fixed positive constant such that at most 50% of geographic neighbors in the study region are classified as non-adjacent. This maintains some degree of smoothing; see Lee

and Mitchell (2012) for further details. Higher values in $\boldsymbol{\eta}$ assist in staying below the threshold, which results in a loss of a geographical boundary in the adjacencies to be smoothed over and, hence, indicates a spatial disparity.

A notable feature of the previous development is the assimilation of information from explanatory variables \boldsymbol{x}_{id} in (1) and \boldsymbol{z}_{ij} in (4). The former informs about the observed values of the health outcomes and captures large-scale trends through the mean structure, while the latter provides information on disparities among geographic neighbors. Vectors \boldsymbol{x}_{id} and \boldsymbol{z}_{ij} can share variables, but need to be indexed differently. For example, one could include the smoking rate for a region i in \boldsymbol{x}_{id} and the difference in smoking rates between regions i and j in \boldsymbol{z}_{ij} . The coefficients in $\boldsymbol{\eta}$ indicate if the corresponding variable in \boldsymbol{z}_{ij} indicates the disparity. They can be based on maps, such as the distance between the centroids of regions i and j or the discrepancies in the percentage of common boundaries shared by the two regions compared to their total geographical boundaries. Topographic data, such as the presence of challenging natural features such as mountain ranges or rivers that hinder travel between regions or to healthcare providers in neighboring regions, can be included. Other examples include sociodemographic information that compares the percentages of urban area between the two regions or the standardized absolute difference in a specific regional characteristic, such as the proportion of residents who smoke or even the expected age-adjusted disease count for the region. Including covariates in \boldsymbol{z}_{ij} , allows one to account for factors that influence the neighboring relationship between regions i and j .

3.3 Multivariate Framework

Recalling that our current data analysis goals involve accounting for dependence between multiple diseases and spatial dependence for each cancer, we build on a rich literature on multivariate areal models (Mardia, 1988; Gelfand and Vounatsou, 2003; Carlin and Banerjee, 2003; Jin et al., 2005, 2007; Zhang et al., 2009; Banerjee, 2016; MacNab, 2018; Gao et al., 2022). Given the computational benefits accrued by DAGAR detailed in Section B of the appendices, we build multivariate DAGAR (MDAGAR, Gao et al., 2022) models for $\boldsymbol{\gamma}$ using three different inter-disease association graphs shown in Figure 4.

3.3.1 Unstructured Graph

We introduce dependence between outcomes using linearly transformed latent variables resulting in an unstructured graph (left panel of Figure 4). Therefore, $\boldsymbol{\gamma}_1 = a_{11}\boldsymbol{f}_1$, $\boldsymbol{\gamma}_d = a_{d1}\boldsymbol{f}_1 + \dots + a_{dd}\boldsymbol{f}_d$ for each $d = 2, \dots, q$, where a_{dh} , $h = 1, \dots, d$, are unknown coefficients that associate spatial components for different diseases and for each $\boldsymbol{f}_d \stackrel{ind}{\sim} \mathcal{N}(\mathbf{0}, \boldsymbol{Q}(\rho_d, \widetilde{\boldsymbol{W}}_d)^{-1})$, where ρ_d and $\widetilde{\boldsymbol{W}}_d$ are the spatial autocorrelation parameter and the lower triangular spatial adjacency matrix, respectively, for disease d . Each $\boldsymbol{\gamma}_d$ is a linear combination of independent DAGAR random variables. This construction ensures that the model is independent of disease ordering as the association among diseases is $\boldsymbol{A}\boldsymbol{A}^T$, where \boldsymbol{A} is lower-triangular to elements a_{dh} . The precision

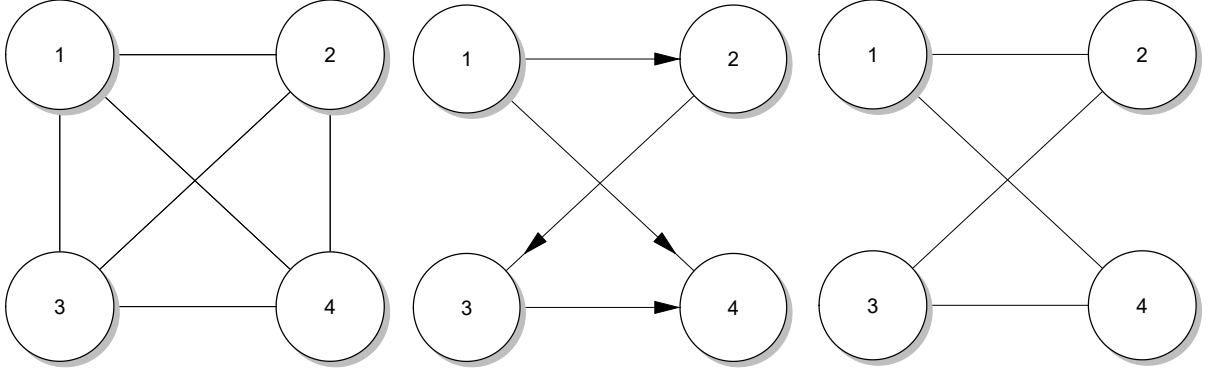


Figure 4: Left: unstructured graph, Center: directed acyclic graph. Right: undirected graph.

matrix of γ is

$$\Sigma_{\gamma}^{-1} = (\mathbf{A}^{-\top} \otimes \mathbf{I}_n) \left[\bigoplus_{d=1}^q \mathbf{Q}(\rho_d, \widetilde{\mathbf{W}}_d) \right] (\mathbf{A}^{-1} \otimes \mathbf{I}_n) \quad (5)$$

where \otimes is the Kronecker product and $\widetilde{\mathbf{W}}_d$ is specified through (4) with a different $\boldsymbol{\eta}_d$ for each disease d and $\bigoplus_{d=1}^q$ defines a block diagonal matrix. Therefore, we are incorporating a random adjacency matrix into the model for each type of cancer. We evaluate the model’s performance by accounting for the particular cancer under consideration, as well as the explanatory variables utilized in model (4) that inform the adjacency structure, which can vary for each type of cancer. Finally, we model $\mathbf{A}\mathbf{A}^{\top}$ using an inverse-Wishart distribution with \mathbf{A} identifying as the unique lower-triangular Cholesky factor.

Alternatively, we introduce a graphical model for multivariate dependencies across diseases (see, e.g., Cox and Wermuth, 1993, 1996). Such models distinguish between “directed” and “undirected” graphs (central and right panels in Figure 4, respectively). The lack of edges in the undirected graph immediately reveals conditional independence $\gamma_2 \perp \gamma_4 \mid \{\gamma_1, \gamma_3\}$ and $\gamma_1 \perp \gamma_3 \mid \{\gamma_2, \gamma_4\}$. However, the directed acyclic graph only imposes the first relation and not the second because γ_2 and γ_4 share a common parent (γ_1).

3.3.2 Directed Graph

Let $\mathcal{G}_{dis} = \{\mathcal{V}_{dis}, \mathcal{E}_{dis}\}$ be a directed acyclic disease graph (the suffix *dis* distinguishes this from the graph of the spatial map), where \mathcal{V}_{dis} consists of q nodes and \mathcal{E}_{dis} comprises directed edges from parents to children (center panel of Figure 4 with $q = 4$). Let

$$\gamma_1 = \mathbf{f}_1, \quad \gamma_d = \mathbf{A}_{d1}\gamma_1 + \cdots + \mathbf{A}_{dd-1}\gamma_{d-1} + \mathbf{f}_d, \quad \text{for } d = 2, \dots, q, \quad (6)$$

where each $\mathbf{f}_d \stackrel{ind}{\sim} \mathcal{N}(\mathbf{0}, \mathbf{Q}(\rho_d, \widetilde{\mathbf{W}}_d)^{-1})$ and $\mathbf{A}_{dd'}$ is $n \times n$ with $\mathbf{A}_{dd'} = \mathbf{O}$, the matrix with all null entries, whenever $d' \geq d$. The equations in (6) encode the conditional distributions $p(\gamma_d \mid \gamma_1, \dots, \gamma_{d-1})$ for $d = 2, \dots, q$. Setting $\mathbf{A}_{dd'} = \mathbf{O}$ whenever node d' is not a parent of d , i.e., there is no directed edge from d' to d , ensures that the model conforms to the conditional independence among diseases posited in \mathcal{G}_{dis} . If $\mathbf{A} = (\mathbf{A}_{dd'})$ is the $N \times N$ block matrix with the

$n \times n$ matrix $\mathbf{A}_{dd'}$ occupying block (d, d') , then \mathbf{A} is strictly lower triangular, hence $\mathbf{I}_N - \mathbf{A}$ is nonsingular and

$$\boldsymbol{\Sigma}_{\boldsymbol{\gamma}}^{-1} = (\mathbf{I}_N - \mathbf{A}^T) \left[\bigoplus_{d=1}^q \mathbf{Q}(\rho_d, \widetilde{\mathbf{W}}_d) \right] (\mathbf{I}_N - \mathbf{A}) \quad (7)$$

is positive definite no matter how we specify $\mathbf{A}_{dd'}$ for all $(d, d') \in \mathcal{E}_{dis}$ (d' is a parent of d).

Setting $\mathbf{A}_{dd'} = \alpha_{0dd'} \mathbf{I}_n + \alpha_{1dd'} \mathbf{W}$, where \mathbf{W} is the fixed geographic map, introduces parameters $\alpha_{0dd'}$ and $\alpha_{1dd'}$ that allow the dependence between diseases d and d' to vary across space. This flexibility is desirable because inter-disease dependencies, or lack thereof, are often manifestations of lurking shared risk factors that remain unaccounted for. Finally, inference from inter-disease DAGAR without depending on disease ordering is possible by using the Bayesian model averaging over all topological orders (Gao et al., 2022), but the method is computationally demanding and not our current focus.

3.3.3 Undirected Graph

In contrast to directed acyclic graphs, “undirected” graphs model relationships among nodes using conditional dependencies. An edge signifies conditional dependence given remaining nodes, while the absence of an edge indicates conditional independence given all other nodes (right panel in Figure 4 with $q = 4$). We specify a Markov random field using full conditional distributions,

$$\boldsymbol{\gamma}_d | \boldsymbol{\gamma}_{(-d)} \sim \mathcal{N}_n \left(\sum_{h=1}^q \mathbf{A}_{dh} \boldsymbol{\gamma}_h, \mathbf{Q}(\rho_d, \widetilde{\mathbf{W}}_d)^{-1} \right), \quad (8)$$

where $\boldsymbol{\gamma}_{(-d)}$ is the collection of all random effects except for the d -th disease type. Each \mathbf{A}_{dh} is $n \times n$ and encodes the relationships between various diseases, while $\mathbf{Q}(\rho_d, \widetilde{\mathbf{W}}_d)$ refers to the univariate precision matrix of the DAGAR model applied to the d -th cancer, capturing the spatial correlation for each cancer. By exploiting a multivariate extension of Brook’s Lemma (see, e.g., Mardia, 1988; Banerjee et al., 2014), the collection of distributions in (8) yield a possible joint Gaussian distribution with zero mean and precision matrix $\boldsymbol{\Sigma}_{\boldsymbol{\gamma}}^{-1} = \left[\bigoplus_{d=1}^q \mathbf{Q}(\rho_d, \widetilde{\mathbf{W}}_d) \right] (\mathbf{I}_N - \mathbf{A})$ provided this matrix is symmetric and positive definite. This is achieved by carefully specifying $\mathbf{A} = (\mathbf{A}_{dh})$.

Let $\boldsymbol{\Lambda}_{dis} = (\mathbf{D}_{dis} - \rho_{dis} \mathbf{W}_{dis})$ be $q \times q$, where \mathbf{W}_{dis} is the $q \times q$ binary adjacency matrix of the inter-disease graph, \mathbf{D}_{dis} is diagonal with the number of edges incident on each node as its diagonal element, and $\rho_{dis} \in (1/\zeta_{min}, \zeta_{max})$ with $\zeta_{min} < 0$ and $\zeta_{max} = 1$ denoting the smallest and largest eigenvalues of $\mathbf{D}_{dis}^{-1/2} \mathbf{W}_{dis} \mathbf{D}_{dis}^{-1/2}$, respectively; all eigenvalues are real, $\zeta_{max} = 1$ since $\mathbf{D}_{dis}^{-1} \mathbf{W}_{dis}$ is row-stochastic and $\zeta_{min} < 0$ since the trace of $\mathbf{D}_{dis}^{-1/2} \mathbf{W}_{dis} \mathbf{D}_{dis}^{-1/2}$ is zero. The interval for ρ_{dis} ensures that $\boldsymbol{\Lambda}_{dis}$ is positive definite.

Setting $\mathbf{U}_d = (\mathbf{I} - \mathbf{B}_d)^T \boldsymbol{\Lambda}_d^{1/2}$ and $\mathbf{A}_{dh} = -\lambda_{dis,dh} \mathbf{U}_d^{-T} \mathbf{U}_h^T$ yields

$$\boldsymbol{\Sigma}_{\boldsymbol{\gamma}}^{-1} = \left[\bigoplus_{d=1}^q \mathbf{U}_d \right] (\boldsymbol{\Lambda}_{dis} \otimes \mathbf{I}_n) \left[\bigoplus_{d=1}^q \mathbf{U}_d^T \right], \quad (9)$$

which is symmetric and positive definite. Since $\mathbf{U}_d \mathbf{U}_d^T = \mathbf{Q}(\rho_d, \widetilde{\mathbf{W}}_d)$, we are using the square-

root of the DAGAR precision $\mathbf{Q}(\rho_d, \widetilde{\mathbf{W}}_d)$ for each disease. This avoids the Cholesky decomposition. Constructing precision matrices avoids matrix inversion. The joint distribution $\boldsymbol{\gamma} \sim \mathcal{N}_n(\mathbf{0}, \boldsymbol{\Sigma}_\gamma)$ serves as a proper prior for the spatial effects conforming to the conditional independence posited by the undirected disease-graph.

3.4 Difference Boundaries Through FDR

We treat spatial boundary analysis as an exercise in multiple-hypothesis testing, although a formal null hypothesis is not required in Bayesian inference. Instead, we pursue full stochastic quantification to derive a threshold to detect spatial disparities specific to cancer. For each pair of adjacent regions, i.e., $i \sim j$, and each cancer d , we seek the posterior probability of $\phi_{id} = \phi_{jd}$ and its complement $\phi_{id} \neq \phi_{jd}$ for region-disease pairs (i, d) and (j, d) . We designate an edge (i, j) as a difference boundary if the posterior probability of $\phi_{id} \neq \phi_{jd}$ given \mathbf{y} exceeds a predefined threshold t .

The most general difference boundary we report is the *cross-difference* boundary based on $v_{(i,d)(j,d')} = P(\phi_{id} \neq \phi_{jd'}, \phi_{id'} \neq \phi_{jd} | \mathbf{y})$. We derive a threshold t that controls the false discovery rate (FDR) below a level $\zeta = 0.05$. To this end, we define

$$\text{FDR}_{d,d'}(t) = \frac{\sum_{i \sim j} I(\phi_{id} = \phi_{jd'}) I(v_{(i,d)(j,d')} > t)}{\sum_{i \sim j} I(v_{(i,d)(j,d')} > t)} \quad (10)$$

every disease pair d and d' . The quantity in (10) is evaluated as

$$\widehat{\text{FDR}}_{d,d'}(t) = \mathbb{E}[\text{FDR}_{d,d'} | \mathbf{y}] = \frac{\sum_{i \sim j} (1 - v_{(i,d)(j,d')}) I(v_{(i,d)(j,d')} > t)}{\sum_{i \sim j} I(v_{(i,d)(j,d')} > t)}.$$

Following Müller et al. (2004), we define

$$t^* = \sup \left\{ t : \widehat{\text{FDR}}_{d,d'}(t) \leq \zeta \right\}, \quad (11)$$

which is based upon the optimal decision that minimizes the estimated false negative rate (FNR), $\widehat{\text{FNR}}_{d,d'}(t) = \left(\sum_{i \sim j} v_{(i,d)(j,d')} (1 - I(v_{(i,d)(j,d')} > t)) \right) / \left(m - \sum_{i \sim j} I(v_{(i,d)(j,d')} > t) \right)$, where m is the total number of geographic boundaries, subject to $\widehat{\text{FDR}} \leq \zeta$ (also see Sun et al., 2015, who proffer a similar approach). Here, ζ serves as an error threshold that must be controlled and, in this sense, is not case-specific. Common choices for this value include the conventional levels 0.01, 0.05, and 0.1. This estimate is based on a bivariate loss function $L_{2R} = (\widehat{\text{FDR}}, \widehat{\text{FNR}})$. The single disease setting is obtained by substituting $v_{i,j}^{(d)} = P(\phi_{id} \neq \phi_{jd}, \phi_{id'} \neq \phi_{jd} | \mathbf{y})$ in the above expressions. This is analogous to Li et al. (2015), with the added flexibility of adjacency and inter-disease dependence modeling.

4 Simulation Experiments

We generate Gaussian data for $q = 4$ diseases using (1) with $y_{id} \stackrel{\text{ind}}{\sim} \mathcal{N}(\mathbf{x}_i^\top \boldsymbol{\beta}_d + \phi_{id}, 1/\tau_d^2)$ in $N = 58$ counties in California. In each replicate, the data are generated after simulating spatial effects $\boldsymbol{\phi} = (\boldsymbol{\phi}_1^\top, \boldsymbol{\phi}_2^\top, \boldsymbol{\phi}_3^\top, \boldsymbol{\phi}_4^\top)^\top \sim G_N$ with parameters fixed as $K = 15$, $\alpha = 5$, $\beta_1 = (2, 8)^\top$, $\beta_2 = (3, 7)^\top$, $\beta_3 = (4, 6)^\top$, $\beta_4 = (5, 5)^\top$, $\tau_d^2 = 500$ for every d and $\tau = 0.1$. Each \mathbf{x}_i is 2×1 consisting of a 1 and a value generated from a standard normal distribution. We generate 100 different replicates of data using the above parameters and generating the spatial effects ϕ_{id} using distributions corresponding to each of the 3 graphs illustrated in Figure 4: (i) unstructured, (ii) directed, and (iii) undirected. These correspond to the three specifications for $\boldsymbol{\Sigma}_\gamma$ in (5), (7) and (9). For each of the above models, $\boldsymbol{\Sigma}_\gamma$ depends on the DAGAR parameters and the inter-disease covariances. The spatial correlation parameters for the different cancers are fixed as $\boldsymbol{\rho} = (0.2, 0.8, 0.4, 0.6)^\top$. For the lower triangular adjacency matrices, $\widetilde{\mathbf{W}}_d$, the elements z_{ij} of \mathbf{Z} are calculated as the standardized absolute difference of a generated covariate $|x_i - x_j|/\sigma$ where σ represents the standard deviation of all absolute differences between the values of x_i in all pairs of contiguous areas. The unknown parameters associated with these variables were fixed at $\boldsymbol{\eta} = (0.4, 0.2, 0.3, 0.5)^\top$. In addition to specifying the DAGAR parameters for each disease, for (i) we specify \mathbf{A} as lower triangular with all elements set to 1. For (ii) we fix $(\alpha_{021}, \alpha_{121})^\top = (0.3, 0.5)^\top$, $(\alpha_{041}, \alpha_{141})^\top = (0.5, 0.4)^\top$, $(\alpha_{032}, \alpha_{132})^\top = (0.4, 0.4)^\top$, and $(\alpha_{043}, \alpha_{143})^\top = (0.8, 0.1)^\top$, and for (iii) we fix $\rho_{dis} = 0.25$. For each of these specifications, we produce a single instance of $\boldsymbol{\Sigma}_\gamma$, which is used to generate a different instance of $\boldsymbol{\gamma}$ in every replication. This yields the 100 sets of random effects used to generate the 100 datasets.

For data analysis, we specify the prior using $\tau_\beta = 0.001$, $a = 2$, $b = 0.1$, $a_\epsilon = 2$, $b_\epsilon = 0.1$, $\alpha = 1$ and $M = -\log(0.5)/\mathbf{Z}_{0.5}$, where $\mathbf{Z}_{0.5}$ represents the 0.5th quantile of elements of \mathbf{Z} . For the unstructured or unconstrained inter-disease graph (left panel in Figure 4) we use the Wishart distribution in (15) with $\nu = 2$ and $\boldsymbol{\Psi} = \text{diag}(0.1, 0.1, 0.1, 0.1)$. For the directed graph (center panel in Figure 4), \mathbf{A} is determined through $\boldsymbol{\alpha} \sim \mathcal{N}(\mathbf{0}, 100\mathbf{I})$, while for the undirected graph (right panel in Figure 4) we specify $\rho_{dis} \sim \mathcal{U}(-1, 1)$. We fit the three models to each of the $3 \times 100 = 300$ datasets and present inference based on 10,000 posterior samples using MCMC algorithms after discarding the initial 10,000 iterations as burn-in. Details on the implementation of the model and the MCMC algorithm are available in Section C of the Supplement.

Each data is analyzed by one correctly specified model and two misspecified models. We evaluate these models with correct and incorrect specifications by computing the Widely Applicable Information Criterion (Watanabe and Opper, 2010; Vehtari et al., 2017) for each model using the `loo` R package (Vehtari et al., 2024). This score measures the extent of information loss in a model with lower values indicating better performance by effectively addressing the risks of both overfitting and underfitting. Table 1 presents the relative differences in WAIC scores. For each disease graph model, we compute the standardized relative difference between the mean WAIC of the misspecified models and the true model, normalized by the mean WAIC of the true model. Not surprisingly, the model corresponding to the true data generating

Table 1: WAIC relative differences for the 3×3 simulation grid.

True/Fit	Unstructured	Directed	Undirected
Unstructured	0.00	+0.26	-0.91
Directed	-0.36	0.00	-0.96
Undirected	+48.49	+57.10	0.00

scheme has the lowest WAIC scores (denoted 0% in the standardized relative difference). However, Table 1 shows that the graphical models perform similarly when analyzing data from the unstructured model. In contrast, for data generated from a misspecified model, the undirected model outperforms both the unstructured and directed models.

Turning to boundary detection, we compute the conditional probability $P(\phi_{id} \neq \phi_{jd} | \mathbf{y})$, for diseases d and d' and geographically neighboring regions i and j . We use these posterior probabilities to obtain sensitivity and specificity for all pairs of regions and for all disease graph models. In each simulation, sensitivity and specificity are determined by selecting a fixed number of edges with the highest T posterior probabilities, where $T \in \{85, 90, 95, 100, 105\}$. This method accounts for false positives across all other T values for the diseases. Table 2 presents the corresponding results for the unstructured model fitted with data generated from the true model (the unstructured model) and the misspecified models (directed and undirected models). The values in Table 2 represent the average sensitivity and specificity of 100 simulated data sets using the unstructured disease graph to fit the model in three different choices of the true disease graph.

With T set to 105, we achieve sensitivities of approximately 90% for all diseases. Despite introducing uncertainty into the adjacency matrix and adopting a much more complex simulation setting compared to Gao et al. (2023), we achieve similar levels of sensitivity. This added uncertainty in the adjacency structure propagates through the model, leading to a notably broader posterior distribution for spatial random effects. A wider posterior distribution indicates a greater incidence of ties between random effects in different cancers and regions. Consequently, with the detection of more boundaries, the specificity decreases. However, the decrease is not huge since in all cases it is still greater than 0.7.

With regard to the adjacency model in (4), Table 3 presents specificity and sensitivity values to detect adjacencies. Here, sensitivity and specificity are evaluated by comparing adjacencies determined by the true value of $\boldsymbol{\eta}$ with estimated adjacencies using the posterior mean of $\boldsymbol{\eta}$ in (4). It appears that higher sensitivity values are achieved across all disease and disease graph models, while specificity values, though slightly lower, remain at satisfactory levels. The high sensitivity coupled with lower specificity suggests that our model excels in identifying true positives but may occasionally incorrectly classify negative cases as positive (false positives).

We conclude this section with a brief remark. For analyzing our data over the map of California, computational costs for the MDAGAR model averaged approximately 0.006 seconds per iteration for the unstructured disease graph, 0.013 for the directed and 0.009 for the unstructured. In comparison, the MCAR took about 0.043 iterations per second for the unstructured disease graph, 0.049 for the directed graph, and 0.045 for the undirected graph. In summary,

Table 2: Boundary detection results in the simulation study under the three disease graph models using the unstructured graph to fit.

True Disease graph	T	Disease 1		Disease 2		Disease 3		Disease 4	
		Specificity	Sensitivity	Specificity	Sensitivity	Specificity	Sensitivity	Specificity	Sensitivity
Unstructured	85	0.835	0.860	0.824	0.886	0.848	0.902	0.909	0.908
	90	0.821	0.872	0.796	0.899	0.813	0.915	0.892	0.915
	95	0.798	0.888	0.764	0.915	0.789	0.922	0.869	0.923
	100	0.762	0.904	0.727	0.926	0.755	0.931	0.832	0.934
	105	0.715	0.920	0.676	0.938	0.706	0.945	0.782	0.943
Directed	85	0.840	0.862	0.805	0.917	0.752	0.934	0.766	0.940
	90	0.818	0.872	0.773	0.927	0.712	0.944	0.707	0.948
	95	0.791	0.882	0.734	0.938	0.639	0.951	0.642	0.955
	100	0.755	0.898	0.654	0.949	0.572	0.959	0.565	0.961
	105	0.714	0.914	0.580	0.958	0.491	0.969	0.492	0.967
Undirected	85	0.855	0.865	0.829	0.848	0.861	0.867	0.915	0.868
	90	0.840	0.878	0.810	0.862	0.847	0.876	0.906	0.877
	95	0.821	0.888	0.787	0.880	0.835	0.889	0.887	0.890
	100	0.786	0.905	0.769	0.892	0.814	0.899	0.866	0.900
	105	0.747	0.920	0.729	0.910	0.784	0.912	0.836	0.917

Table 3: Adjacencies detection for the three disease graph models using the unstructured graph to fit.

True Disease graph	Disease 1		Disease 2		Disease 3		Disease 4	
	Specificity	Sensitivity	Specificity	Sensitivity	Specificity	Sensitivity	Specificity	Sensitivity
Unstructured	0.321	0.987	0.647	0.927	0.625	0.961	0.283	1.000
Directed	0.340	0.988	0.604	0.919	0.645	0.957	0.264	0.999
Undirected	0.273	0.990	0.636	0.924	0.553	0.95	0.301	0.999

MDAGAR is substantially more efficient (gains of 86%, 73%, and 80% for the unstructured, directed, and undirected, respectively) than MCAR while offering very similar inference for boundary detection. Section D in the appendices offers additional results from the simulations, including root median squared error, sensitivity, and specificity tables for models fitted under the true model and their WAIC values.

5 SEER Cancers Analysis

We analyze the data set introduced in Section 2 using a Poisson spatial regression model. Specifically, we model the incidence counts observed for each county and for each cancer as $y_{id} | \beta_d, \phi_{id} \stackrel{ind}{\sim} Pois(E_{id} \exp(\beta_d + \phi_{id}))$ for $i = 1, \dots, 58$ and $d = 1, \dots, 4$, thus putting the covariates only in the adjacency model as shown in Section 3.2. We employ the unstructured model with Σ_γ^{-1} , as in (5), since a prior graphical model of cancer dependence is lacking. Here, we draw diagnostic inference based upon 50,000 posterior iterations, retaining one every 5 samples, using MCMC algorithms after discarding an initial 50,000 iterations as burn-in. Throughout this Section, it is worth noting, we comment on the results by directly referring to specific counties by their names. For a visual reference of the corresponding county names, we refer the reader to the map provided in Figure 16 and to the appendices. Section E there includes a table of posterior means, plots of the credible intervals 95%, and an evaluation of the Monte Carlo standard errors for the model.

We employ a threshold to control for FDR as specified in (11) to detect difference boundaries

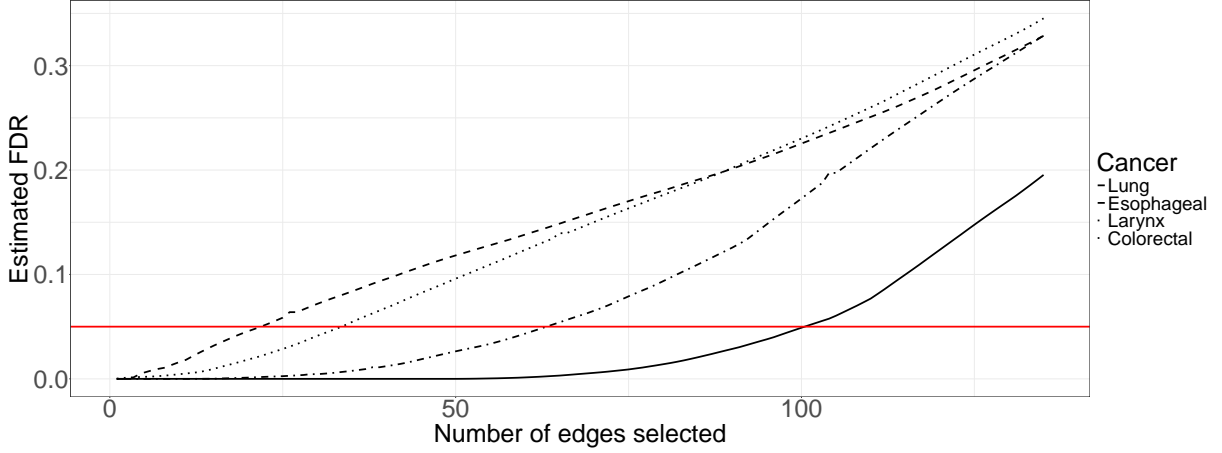


Figure 5: Estimated FDR curves plotted against the number of selected difference boundaries for four cancers

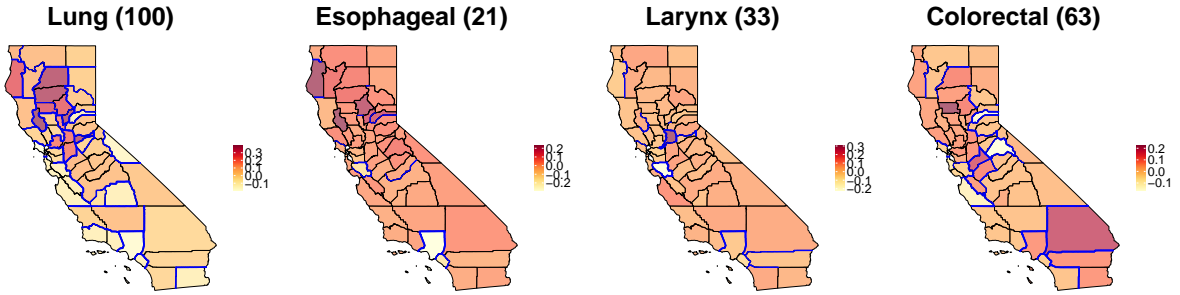


Figure 6: Estimated difference boundaries (bold borders, their numbers in parenthesis) for 4 cancers among counties in California based on posterior mean of ϕ_{id} when $\zeta = 0.05$.

for each cancer. Figure 5 plots the estimated FDR against varying numbers of selected edges as difference boundaries for the four cancers individually. We observe analogous FDR curves for esophageal and larynx cancers, causing us to select a similar number of boundaries for these two cancers with a threshold of $\zeta = 0.05$. We detect a much larger number of boundaries for lung cancer and a much smaller number for colorectal cancer using the same threshold, indicating considerable variation in spatial disparities among these cancers.

Setting $\zeta = 0.05$ in (11), Figure 6 illustrates the identified difference boundaries (highlighted in blue) in the California maps for the four types of cancer, colored according to the posterior means of the corresponding ϕ_{id} . The width of the lines on the boundaries signify higher probabilities of detection. In particular, lung cancer exhibits the highest number of detected boundaries, i.e., 100, with colorectal cancer showing a much higher number of boundaries, i.e., 63, compared to esophageal and larynx cancer with 21 and 33 boundaries, respectively. It should be noted that the detected boundaries for the different cancers tend to form geographical groups, which include regions with similar random effects.

In northern California, for example, we observe that 10 counties (Tehama, Glenn, Butte, Yuba, Lake, Colusa, Shasta, Trinity, Humboldt and Del Norte) form a “group” with high posterior medians of spatial effects for lung cancer, where “group” indicates that these counties do not exhibit disparities (or difference boundaries) among themselves, but do so with other

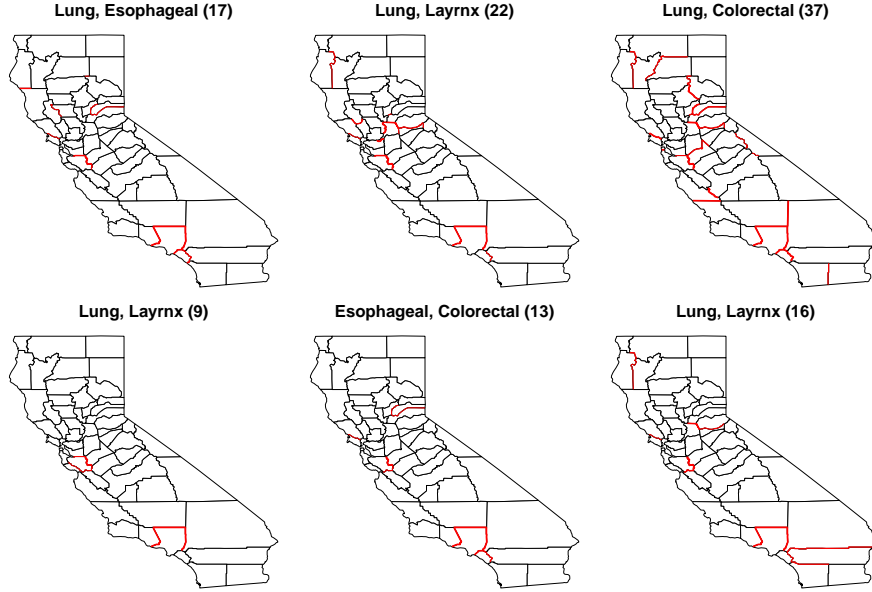


Figure 7: Shared difference boundaries (bold borders) detected for each pair of cancers in California map when $\zeta = 0.05$. The numbers in parenthesis indicate the difference boundaries detected.

neighbors. A similar grouping appears in the central regions for Solano (Bay Area), Sacramento, and San Joaquin, with elevated posterior random-effects estimates for lung cancer. Moving to central California, we find Stanislaus, Merced, Tuolumne, Mariposa, Madera, and Fresno counties forming a group with moderately elevated spatial effects while not exhibiting disparities among them. Colorectal cancer offers a similar story in central counties. In contrast, maps for esophageal and larynx cancers reveal different patterns. Identifying spatial patterns for larynx and esophageal cancer is more difficult, and detected boundaries are less pronounced compared to lung cancer. However, the model identifies boundaries in Santa Clara County based on posterior means of random effects for esophageal cancer and similarly for Los Angeles County, which depicts the lowest posterior mean for random effects and is surrounded by counties with higher values. These disparities are likely due to the inclusion of differences standardized for smoking in our adjacency model, which significantly influences lung, esophageal, and larynx cancers (Doll et al., 2005).

To distinguish boundaries between cancers, we examine shared difference boundaries and mutual cross-cancer boundaries. The boundaries of shared differences refer to those detected in common in different cancers. Figure 7 illustrates the shared boundaries for each pair of cancers, denoted as $P(\phi_{id} \neq \phi_{jd}, \phi_{id'} \neq \phi_{jd'} | \mathbf{y})$ where $d \neq d'$. We have observed a consistent detection of specific boundaries whenever the lung is affected. For example, Los Angeles reveals disparities with Ventura, Kern, and San Bernardino. Similarly, when examining all cancers, disparities are observed between Santa Clara and Stanislaus. In particular, all the Los Angeles geographic neighbors are consistently identified.

We introduce mutual cross-cancer boundaries by evaluating $P(\phi_{id} \neq \phi_{jd'}, \phi_{id'} \neq \phi_{jd} | \mathbf{y})$, where $i \sim j$ and $i < j$, to determine the boundaries for cross-cancer differences. This boundary effectively segregates the effects related to distinct cancers between adjacent counties (see

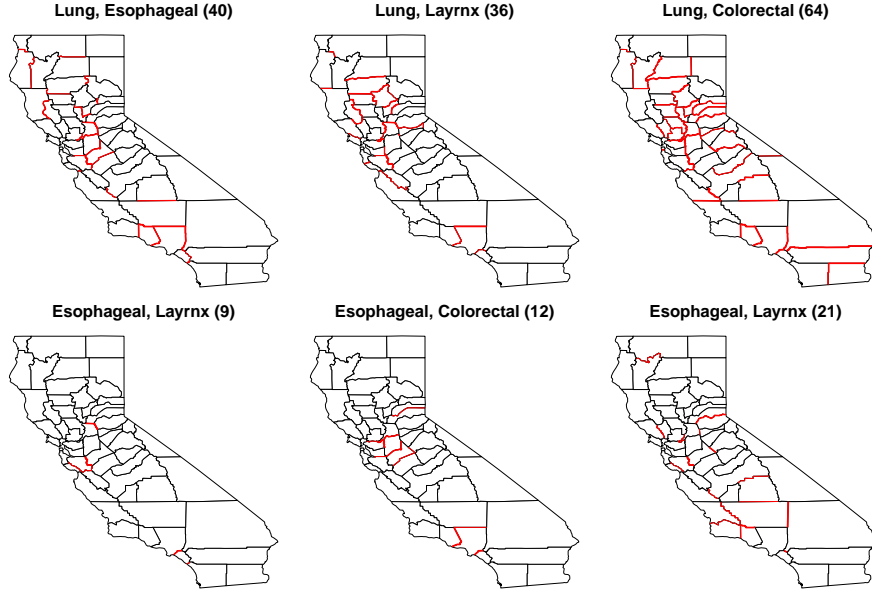


Figure 8: Mutual cross-difference boundaries (bold borders) detected by the model for each pair of cancers in California map when $\zeta = 0.05$. The values in brackets are the number of difference boundaries detected.

Figure 8). We observe analogous detection between counties for lung-esophageal and lung-larynx differences. It is clear that the number of detected borders is significantly higher for lung-esophageal, lung-larynx, and lung-colorectal cancers compared to other types. In addition, Stanislaus is clearly separated from Santa Clara and Los Angeles from Ventura, indicating notable differences when these cancer relationships are taken into account.

Including explanatory variables affects difference boundary detection, leading to either larger or smaller numbers of such boundaries. This depends on whether a covariate intensifies the disparity in residual spatial effects between two adjacent counties, whence a difference boundary is more likely to be observed between them. Conversely, if a covariate explains or absorbs the disparity in residual spatial effects between two neighboring counties, then the presence of a difference boundary diminishes. The former occurs individually, for example, for lung, esophageal, and larynx boundary detection, while the latter is seen for colorectal for which we detect fewer boundaries. The impact of covariates on the number of difference boundaries depends on how they affect the variation in rates between neighboring counties. We note that while covariates always absorb some spatial effects, relationships among cancers, regions, and covariates are intricate, and a definitive pattern can remain elusive.

Turning to adjacency models, non-adjacency is detected based on the following:

$$P(w_{d,ij} = 0 | \mathbf{y}, i \sim j) \quad (12)$$

where $w_{d,ij}$ represents the (i, j) -th element of the adjacency matrix corresponding to the d -th cancer. Figure 9 presents a map of California where the thickness of the boundaries indicates the associated probabilities. The blue highlighted county boundaries signify that (12) is not negligible and are identified as “not adjacent”. The northern and central counties exhibit higher

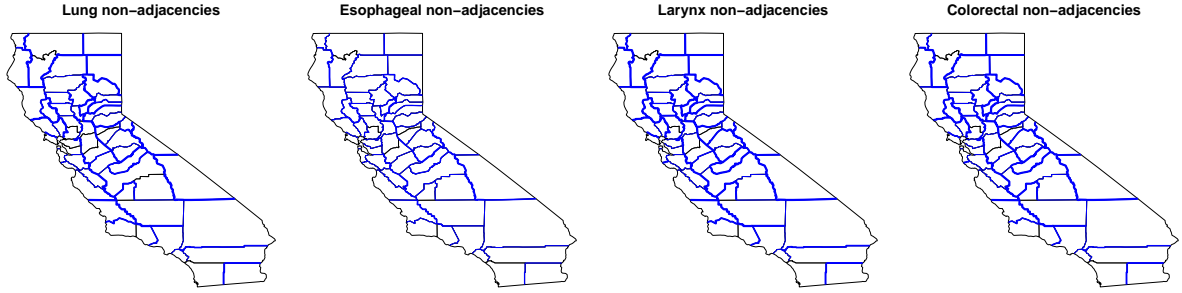


Figure 9: Non-adjacencies (bold borders) over the California map. The thickness of the lines is proportional to the probability of being considered as a non-adjacency

values of (12). Figure 9 suggests that this phenomenon probably reflects the greater differences in covariates between neighboring counties in these regions than in the South. Taking into account the four cancers, the number of adjacencies having probability (12) less than 0.1 is 67 for the lung, 5 for the esophageal, 79 for the larynx, and 67 for colorectal. These correspond to approximately 48%, 4%, 57% and 48% of the total number of county boundaries, respectively.

In general, non-adjacencies with the highest probabilities are predominantly between counties with large differences in covariates, especially in smoking rates, while esophageal cancer seems to exhibit lower probabilities. Conversely, counties with lower differences in covariates exhibit zero detected non-adjacencies. This strongly suggests that smoking, more than the other covariates, serves as a dissimilarity metric for identifying disparities, as the estimated limits align closely with significant variations in smoking rates.

Sections F.1 and F.2 in the appendices present results from two additional settings. The former introduces covariates as fixed effects and in the adjacencies, while the latter does so only in the regression while fixing the adjacencies. Difference boundary maps show the impact of differences among covariates on *defining* the adjacency rather than fix it as a geographic neighbor. Introducing covariates as fixed effects and in adjacency explains how specific factors contribute to the mean and the spatial patterns. Similarly, including covariates solely in the mean structure, with fixed adjacencies, enables assessing the influence of these variables on the overall mean values of the observed phenomena.

6 Discussion

We address the need for formal modeling to determine health disparities, which has been articulated in the literature (see, e.g., Rao, 2023, and references therein). We achieve full probabilistic uncertainty quantification by endowing random effects with discrete masses to detect disparities among neighbors while also allowing spatial smoothing across neighbors as is customary in disease mapping.

As in Gao et al. (2023), we deal with multiple diseases, possibly associated among themselves, but now explicitly address multivariate dependencies flexibly using the graphical models presented. Second, we address a possible limitation of Gao et al. (2023) in which factors informing about disparities need to be evaluated using their inclusion and exclusion in models

with subsequent model assessment. Instead, we introduce such factors in the adjacency model. This enriches previous statistical frameworks for “areal wombling” that have attempted similar adjacency models with limited effectiveness, since the statistical significance of boundary effects is difficult to establish with hierarchically embedded information. Our framework, on the other hand, enables flexible modeling of boundaries, but uses a Bayesian FDR approach to ascertain spatial difference boundaries.

Our application to the SEER database leads to data-driven discoveries with regard to detecting spatial disparities while accounting for inter-disease dependence. Associations among lung, esophageal, and larynx cancers have significant implications for public health and cancer prevention initiatives. These associations suggest that interventions targeting one of these malignancies could potentially have a positive impact on reducing the incidence and burden of the others. By recognizing shared patterns and risk factors, healthcare professionals and policy makers can develop more targeted and effective interventions. In response to our findings, a multifaceted approach can be used to reduce the overall burden of these cancers. Such an approach would encompass public awareness campaigns to educate people about shared risk factors and promote healthy lifestyle choices.

Finally, we note future avenues for research. We do not claim that our inferential framework is unique in detecting spatial disparities. We noted a substantial relevant literature in areal “wombling” that offers ample scope for developing alternative inferential methods based on an explicit threshold on the difference of neighboring outcomes (referred to as “boundary likelihood values” in “wombling”). Wu and Banerjee (2024) offer a Bayesian linear regression framework that calibrates the threshold using Shannon entropy. Extending such approaches to multivariate and non-Gaussian outcomes and comparing with our current approach, while beyond the scope of the current manuscript, will shape future investigations.

References

- Agrawal, K., Markert, R. J., and Agrawal, S. (2018). Risk factors for adenocarcinoma and squamous cell carcinoma of the esophagus and lung. *Hypertension*, 61(46):0–09.
- Akhtar, J., Bhargava, R., Shameem, M., Singh, S. K., Baneen, U., Khan, N. A., Hassan, J., and Sharma, P. (2010). Second primary lung cancer with glottic laryngeal cancer as index tumor—a case report. *Case reports in oncology*, 3(1):35–39.
- Banerjee, S. (2016). Multivariate spatial models. In Lawson, A. B., Banerjee, S., Haining, R. P., and Ugarte, M. D., editors, *Handbook of Spatial Epidemiology*, pages 375–397. Taylor & Francis/CRC Press, Boca Raton, FL.
- Banerjee, S., Carlin, B. P., and Gelfand, A. E. (2014). *Hierarchical Modeling And Analysis For Spatial Data*. CRC press.
- Carlin, B. P. and Banerjee, S. (2003). Hierarchical multivariate car models for spatio-temporally correlated survival data. *Bayesian Statistics*, 7(7):45–63.

- Corpas-Burgos, F. and Martinez-Beneito, M. A. (2020). On the use of adaptive spatial weight matrices from disease mapping multivariate analyses. *Stochastic Environmental Research and Risk Assessment*, 34:531–544.
- Cox, D. and Wermuth, N. (1996). *Multivariate Dependencies*. Chapman & Hall/CRC, Boca Raton, FL.
- Cox, D. R. and Wermuth, N. (1993). Linear Dependencies Represented by Chain Graphs. *Statistical Science*, 8(3):204 – 218.
- Datta, A., Banerjee, S., Hodges, J. S., and Gao, L. (2019). Spatial disease mapping using directed acyclic graph auto-regressive (DAGAR) models. *Bayesian analysis*, 14(4):1221.
- Doll, R., Peto, R., Boreham, J., and Sutherland, I. (2005). Mortality from cancer in relation to smoking: 50 years observations on british doctors. *British journal of cancer*, 92(3):426–429.
- Eddelbuettel, D. and Sanderson, C. (2014). Rcpparmadillo: Accelerating r with high-performance c++ linear algebra. *Computational Statistics and Data Analysis*, 71:1054–1063.
- Fitzpatrick, M. C., Preisser, E. L., Porter, A., Elkinton, J., Waller, L. A., Carlin, B. P., and Ellison, A. M. (2010). Ecological boundary detection using Bayesian areal wombling. *Ecology*, 91(12):3448–3455.
- Flegal, J. M., Hughes, J., Vats, D., Dai, N., Gupta, K., and Maji, U. (2021). *mcmcse: Monte Carlo Standard Errors for MCMC*. Riverside, CA, and Kanpur, India. R package version 1.5-0.
- Gamerman, D. and Lopes, H. F. (2006). *Markov chain Monte Carlo: stochastic simulation for Bayesian inference*. CRC press.
- Gao, L., Banerjee, S., and Ritz, B. (2023). Spatial difference boundary detection for multiple outcomes using Bayesian disease mapping. *Biostatistics*, 24(4):922–944.
- Gao, L., Datta, A., and Banerjee, S. (2022). Hierarchical multivariate directed acyclic graph autoregressive models for spatial diseases mapping. *Statistics in Medicine*, 41(16):3057–3075.
- Gelfand, A. E. and Vounatsou, P. (2003). Proper multivariate conditional autoregressive models for spatial data analysis. *Biostatistics*, 4(1):11–15.
- Gianella, M., Beraha, M., and Guglielmi, A. (2023). Bayesian nonparametric boundary detection for income areal data. *arXiv preprint arXiv:2312.13992*.
- Gong, L. and Flegal, J. M. (2016). A practical sequential stopping rule for high-dimensional markov chain monte carlo. *Journal of Computational and Graphical Statistics*, 25(3):684–700.
- Hanson, T., Banerjee, S., Li, P., and McBean, A. (2015). Spatial boundary detection for areal counts. In *Nonparametric Bayesian Inference in Biostatistics*, pages 377–399. Springer.

- Jacquez, G. M. and Greiling, D. A. (2003a). Geographic boundaries in breast, lung and colorectal cancers in relation to exposure to air toxics in long island, new york. *International Journal of Health Geographics*, 2(1):1–22.
- Jacquez, G. M. and Greiling, D. A. (2003b). Local clustering in breast, lung and colorectal cancer in long island, new york. *International Journal of Health Geographics*, 2(1):1–12.
- Jin, X., Banerjee, S., and Carlin, B. P. (2007). Order-free co-regionalized areal data models with application to multiple-disease mapping. *Journal of the Royal Statistical Society: Series B (Statistical Methodology)*, 69(5):817–838.
- Jin, X., Carlin, B. P., and Banerjee, S. (2005). Generalized hierarchical multivariate car models for areal data. *Biometrics*, 61(4):950–961.
- Kalli, M., Griffin, J. E., and Walker, S. G. (2011). Slice sampling mixture models. *Statistics and computing*, 21:93–105.
- Koch, T. (2005). *Cartographies of disease: maps, mapping, and medicine*. Esri Press Redlands, CA.
- Kurishima, K., Miyazaki, K., Watanabe, H., Shiozawa, T., Ishikawa, H., Satoh, H., and Hizawa, N. (2018). Lung cancer patients with synchronous colon cancer. *Molecular and clinical oncology*, 8(1):137–140.
- Lawson, A. B. (2013). *Statistical methods in spatial epidemiology*. John Wiley & Sons.
- Lawson, Andrew, B., Banerjee, S., Haining, R., and Ugarte, Maria, D. (2016). *Handbook of Spatial Epidemiology*. CRC press, Boca Raton, FL.
- Lee, D. and Mitchell, R. (2012). Boundary detection in disease mapping studies. *Biostatistics*, 13(3):415–426.
- Li, P., Banerjee, S., Carlin, B. P., and McBean, A. M. (2012). Bayesian areal wombling using false discovery rates. *Statistics and its Interface*, 5(2):149–158.
- Li, P., Banerjee, S., Hanson, T. A., and McBean, A. M. (2015). Bayesian models for detecting difference boundaries in areal data. *Statistica Sinica*, 25(1):385.
- Li, P., Banerjee, S., and McBean, A. M. (2011). Mining boundary effects in areally referenced spatial data using the Bayesian information criterion. *Geoinformatica*, 15(3):435–454.
- Liang, Y. (2019). Graph-based multivariate conditional autoregressive models. *Statistical Theory and Related Fields*, 3(2):158–169.
- Lu, H. and Carlin, B. P. (2005). Bayesian areal wombling for geographical boundary analysis. *Geographical Analysis*, 37(3):265–285.

- Lu, H., Reilly, C. S., Banerjee, S., and Carlin, B. P. (2007). Bayesian areal wombling via adjacency modeling. *Environmental and ecological statistics*, 14:433–452.
- Ma, H. and Carlin, B. P. (2007). Bayesian multivariate areal wombling for multiple disease boundary analysis. *Bayesian Analysis*, 2(2):281–302.
- Ma, H., Carlin, B. P., and Banerjee, S. (2010). Hierarchical and joint site-edge methods for medicare hospice service region boundary analysis. *Biometrics*, 66(2):355–364.
- MacNab, Y. C. (2018). Some recent work on multivariate Gaussian Markov random fields (with discussion). *TEST: An Official Journal of the Spanish Society of Statistics and Operations Research*, 27(3):497–541.
- Mardia, K. (1988). Multi-dimensional multivariate gaussian markov random fields with application to image processing. *Journal of Multivariate Analysis*, 24(2):265–284.
- Miasojedow, B., Moulines, E., and Vihola, M. (2013). An adaptive parallel tempering algorithm. *Journal of Computational and Graphical Statistics*, 22(3):649–664.
- Müller, P., Parmigiani, G., Robert, C., and Rousseau, J. (2004). Optimal sample size for multiple testing: the case of gene expression microarrays. *Journal of the American Statistical Association*, 99(468):990–1001.
- Müller, P., Quintana, F. A., Jara, A., and Hanson, T. (2015). *Bayesian Nonparametric Data Analysis*. Springer.
- National Cancer Institute (2019). Seer*stat software.
- Olkin, I. and Sampson, A. R. (1972). Jacobians of matrix transformations and induced functional equations. *Linear Algebra and its applications*, 5(3):257–276.
- Pavani, J. and Quintana, F. A. (2024). A Bayesian multivariate model with temporal dependence on random partition of areal data. *arXiv preprint arXiv:2401.08303*.
- Petrone, S., Guindani, M., and Gelfand, A. E. (2009). Hybrid dirichlet mixture models for functional data. *Journal of the Royal Statistical Society: Series B (Statistical Methodology)*, 71(4):755–782.
- Rao, J. S. (2023). *Statistical Methods in Health Disparity Research*. Chapman & Hall/CRC, Boca Raton, FL.
- Rodríguez, A., Dunson, D. B., and Gelfand, A. E. (2010). Latent stick-breaking processes. *Journal of the American Statistical Association*, 105(490):647–659.
- Shi, W.-X. and Chen, S.-Q. (2004). Frequencies of poor metabolizers of cytochrome p450 2c19 in esophagus cancer, stomach cancer, lung cancer and bladder cancer in chinese population. *World journal of gastroenterology: WJG*, 10(13):1961.

- Sun, W., Reich, B. J., Tony Cai, T., Guindani, M., and Schwartzman, A. (2015). False discovery control in large-scale spatial multiple testing. *Journal of the Royal Statistical Society Series B: Statistical Methodology*, 77(1):59–83.
- Vats, D., Flegal, J. M., and Jones, G. L. (2019). Multivariate output analysis for markov chain monte carlo. *Biometrika*, 106(2):321–337.
- Vehtari, A., Gabry, J., Magnusson, M., Yao, Y., Bürkner, P.-C., Paananen, T., and Gelman, A. (2024). loo: Efficient leave-one-out cross-validation and waic for Bayesian models. R package version 2.8.0.
- Vehtari, A., Gelman, A., and Gabry, J. (2017). Practical Bayesian model evaluation using leave-one-out cross-validation and waic. *Statistics and Computing*, 27:1413–1432.
- Waller, L. and Carlin, B. (2010). Disease mapping. In Gelfand, A. E., Diggle, P., Guttorp, P., and Fuentes, M., editors, *Handbook Of Spatial Statistics*, page 217–243. CRC Press, Boca Raton, FL.
- Waller, L. A. and Gotway, C. A. (2004). *Applied spatial statistics for public health data*, volume 368. John Wiley & Sons.
- Watanabe, S. and Opper, M. (2010). Asymptotic equivalence of Bayes cross validation and widely applicable information criterion in singular learning theory. *Journal of machine learning research*, 11(12).
- Womble, W. H. (1951). Differential systematics. *Science*, 114(2961):315–322.
- Wu, K. L. and Banerjee, S. (2024). Assessing spatial disparities: A Bayesian linear regression approach. arXiv:2407.19171.
- Zhang, Y., Hodges, J. S., and Banerjee, S. (2009). Smoothed anova with spatial effects as a competitor to mcar in multivariate spatial smoothing. *The Annals of Applied Statistics*, 3(4):1805.

Appendix A: Univariate DAGAR Review

We briefly review the univariate DAGAR that uses a fixed set of arbitrarily ordered regions that yield a *topologically ordered* set of vertices, $\mathcal{V} = \{1, \dots, n\}$, and a set \mathcal{E} of directed edges that encode “neighbors” of every region. Rather than defining all geographically adjacent regions as neighbors, DAGAR defines neighbors of a given region i as regions that (i) are geographically adjacent to i and (ii) precede i in topological order. The directed graph $\mathcal{G} = (\mathcal{V}, \mathcal{E})$ is constructed from this definition. The precision matrix of a DAGAR random variable is $\mathbf{Q}(\rho) = (\mathbf{I} - \mathbf{B})^\top \mathbf{\Lambda} (\mathbf{I} - \mathbf{B})$, where $\mathbf{B} = (b_{ij})$ is $n \times n$ with elements $b_{ij} = \rho / (1 + (n_{<i} - 1)\rho^2)$ if there is a directed edge $(i, j) \in \mathcal{E}$ for $i \geq 2$, where $n_{<i}$ is the number of neighboring regions

preceding i and $b_{ij} = 0$ if $(i, j) \notin \mathcal{E}$. In DAGAR, $(i, j) \in \mathcal{E}$ if $j < i$ is in topological order and the regions i and j are geographically adjacent. This implies that $b_{ii} = 0$ and $b_{ij} = 0$ for all $i \leq j$ so \mathbf{B} is strictly lower triangular. The diagonal matrix $n \times n$ $\mathbf{\Lambda} = \text{diag}(\lambda_i)$ has elements $\lambda_i = (1 + (n_{<i} - 1)\rho^2)/(1 - \rho^2)$ along its diagonal for $i = 1, \dots, n$, where $n_{<1} = 0$. Datta et al. (2019) showed that ρ can be interpreted as a spatial autocorrelation parameter and that the ordering is irrelevant or does not impact the analysis in most applications. DAGAR holds further appeal as it accounts for all edges without any omissions, while still yielding a computationally efficient precision matrix.

Two extensions of DAGAR are relevant to our current data-analytic objectives. First, as mentioned in Section 1, we intend to model the adjacency matrix rather than specify it purely from the map. Geographic adjacency, by itself, is not enough to infer similarities or disparities, and we accommodate learning about adjacency relationships using risk factors or other explanatory variables. We adopt one possible fully model-based approach for inferring about spatial disparities by statistically estimating difference boundaries. We use spatially oriented risk factors and explanatory variables to drive inference on difference boundaries. Second, while extending to joint models for dependent cancer occurrences, we allow the impact of the factors informing about the edges to vary by the diseases under consideration. This synthesizes the approaches in Lee and Mitchell (2012) and Gao et al. (2023).

For a complete overview of the DAGAR model (Datta et al., 2019), its precision matrix has the following structure:

$$\begin{aligned} \mathbf{Q}(\rho) &= (\mathbf{I} - \mathbf{B})^\top \mathbf{\Lambda} (\mathbf{I} - \mathbf{B}) \\ &= \begin{bmatrix} 1 & -b_{12} & \cdots & -b_{1n} \\ 0 & 1 & \cdots & -b_{2n} \\ \vdots & \vdots & \ddots & \vdots \\ 0 & 0 & \cdots & 1 \end{bmatrix} \begin{bmatrix} \lambda_1 & 0 & \cdots & 0 \\ 0 & \lambda_2 & \cdots & 0 \\ \vdots & \vdots & \ddots & \vdots \\ 0 & 0 & \cdots & \lambda_n \end{bmatrix} \begin{bmatrix} 1 & 0 & \cdots & 0 \\ -b_{12} & 1 & \cdots & 0 \\ \vdots & \vdots & \ddots & \vdots \\ -b_{1n} & -b_{2n} & \cdots & 1 \end{bmatrix} \\ &= \begin{bmatrix} \lambda_1 + \sum_{i=2}^n \lambda_i b_{1i}^2 & -\lambda_2 b_{12} + \sum_{i=3}^n \lambda_i b_{1i} b_{2i} & \cdots & -\lambda_n b_{1n} \\ -\lambda_2 b_{12} + \sum_{i=3}^n \lambda_i b_{1i} b_{2i} & \lambda_2 + \sum_{i=3}^n \lambda_i b_{2i}^2 & \cdots & -\lambda_n b_{2n} \\ \vdots & \vdots & \ddots & \vdots \\ -\lambda_n b_{1n} & -\lambda_n b_{2n} & \cdots & \lambda_n \end{bmatrix} \end{aligned}$$

One of the main advantages of the DAGAR formulation is the computation of the determinant and the quadratic form in the multivariate normal probability density function. Specifically:

$$\begin{aligned} |\mathbf{Q}(\rho)| &= |\mathbf{I} - \mathbf{B}| |\mathbf{\Lambda}| |\mathbf{I} - \mathbf{B}| = \prod_{i=1}^n \lambda_i \\ \boldsymbol{\gamma}^\top \mathbf{Q}(\rho) \boldsymbol{\gamma} &= \boldsymbol{\gamma}^\top (\mathbf{I} - \mathbf{B})^\top \mathbf{\Lambda} (\mathbf{I} - \mathbf{B}) \boldsymbol{\gamma} = \lambda_1 \gamma_1^2 + \sum_{i=1}^n \lambda_i (\gamma_i - \sum_{j<i} \gamma_j b_{ij})^2 \end{aligned}$$

which are easier to compute. In particular the determinant computation reduces to computing a product of n terms while the quadratic form is lighter since it takes into account the sparsity

of the structure and the strictly lower triangular structure of \mathbf{B} .

Appendix B: MDAGAR details

In this section, we first give some remarks about the multivariate framework. Then, we explain the computational advantages of the proposed approaches using simplified algebraic expressions.

B.1 Remarks on Multivariate Models

The constructions of Σ_γ^{-1} in (5), (7) and (9) offer some appealing features for analyzing multivariate spatial data. All three introduce spatial dependence, and the latter two conform to dependencies posited by graphs. They retain DAGAR's computationally efficient structure and accommodate further modeling of the spatial adjacency matrix as in (4). The structure affords parsimony in storage and computation. For the practicing spatial analyst, these structures offer an inferential tool to aid in understanding localized spatial disease patterns. This tool becomes particularly valuable when adjacencies are identified despite visible disparities. In such cases, investigators can investigate deeper into these regions to explore additional contributing factors to the observed disparity.

In particular, our implementation minimizes computational burden compared to the MCAR model, by avoiding the need to invert matrices, except in the case of the unstructured graph where only a $q \times q$ lower triangular matrix inversion is required, and by simplifying the computation of determinants. In most applications, typically, the value of q is not an issue for computational efficiency. Section B.2 offers further details on the computational benefits of these approaches.

B.2 Computational advantages

Taking into account the multiple disease framework, our model allow for the following multivariate gaussian log-density evaluation:

$$\begin{aligned} \log(p(\boldsymbol{\gamma} | \Sigma_\gamma)) &= \log(2\pi)^{-N/2} \left(|\Sigma_\gamma|^{-1/2} \exp\left(-\frac{1}{2}\boldsymbol{\gamma}^\top \Sigma_\gamma^{-1} \boldsymbol{\gamma}\right) \right) \\ &= -\frac{nq}{2} \log(2\pi) + \frac{1}{2} \log |\Sigma_\gamma^{-1}| - \frac{1}{2} \boldsymbol{\gamma}^\top \Sigma_\gamma^{-1} \boldsymbol{\gamma} \end{aligned}$$

Unstructured graph We first need to compute $|\Sigma_\gamma^{-1}|$:

$$|\Sigma_\gamma^{-1}| = |\mathbf{A}^\top \otimes \mathbf{I}|^{-1} \prod_{d=1}^q |\mathbf{Q}_d| |\mathbf{A} \otimes \mathbf{I}|^{-1} = |\mathbf{A}|^{-2n} \prod_{d=1}^q |\mathbf{Q}_d| = \left(\prod_{d=1}^q \mathbf{A}_{dd} \right)^{-2n} \prod_{d=1}^q \prod_{i=1}^n (\Lambda_d)_{ii}$$

where $|\mathbf{Q}_d| = |\mathbf{I} - \mathbf{B}_d|^2 |\mathbf{\Lambda}_d| = |\mathbf{\Lambda}_d|$ is motivated by the strictly lower-triangularity of \mathbf{B}_d and $|\mathbf{A}| = \prod_{d=1}^q \mathbf{A}_{dd}$ by the lower-triangularity of \mathbf{A} . Then we need to compute $\boldsymbol{\gamma}^\top \boldsymbol{\Sigma}_\gamma^{-1} \boldsymbol{\gamma}$:

$$\begin{aligned} \boldsymbol{\gamma}^\top \boldsymbol{\Sigma}_\gamma^{-1} \boldsymbol{\gamma} &= \boldsymbol{\gamma}^\top (\mathbf{A}^{-1} \otimes \mathbf{I})^\top \left[\bigoplus_d^q \mathbf{Q}_d \right] (\mathbf{A}^{-1} \otimes \mathbf{I}) \boldsymbol{\gamma} \\ &= [(\mathbf{A}^{-1} \otimes \mathbf{I}) \boldsymbol{\gamma}]^\top \left[\bigoplus_d^q \mathbf{Q}_d \right] [(\mathbf{A}^{-1} \otimes \mathbf{I}) \boldsymbol{\gamma}] \end{aligned}$$

Here we need some algebra to simplify the expression. Let's start by defining $\boldsymbol{\Gamma} = [\boldsymbol{\gamma}_1 | \cdots | \boldsymbol{\gamma}_q]$ and by exploiting some properties of the Kronecker product:

$$(\mathbf{A}^{-1} \otimes \mathbf{I}) \boldsymbol{\gamma} = (\mathbf{A}^{-1} \otimes \mathbf{I}) \text{vec}(\boldsymbol{\Gamma}) = \text{vec}(\mathbf{I} \boldsymbol{\Gamma} \mathbf{A}^{-\top}) = \text{vec}(\boldsymbol{\Gamma} \mathbf{A}^{-\top}) = \text{vec}(\mathbf{C})$$

Here, matrix \mathbf{C} is computed as:

$$\begin{aligned} \mathbf{C} &= [\boldsymbol{\gamma}_1 | \boldsymbol{\gamma}_2 | \cdots | \boldsymbol{\gamma}_q] \begin{bmatrix} \tilde{a}_{11} & \tilde{a}_{21} & \cdots & \tilde{a}_{q1} \\ 0 & \tilde{a}_{22} & \cdots & \tilde{a}_{q2} \\ \vdots & \vdots & \ddots & \vdots \\ 0 & 0 & \cdots & \tilde{a}_{qq} \end{bmatrix} \\ &= [\tilde{a}_{11} \boldsymbol{\gamma}_1 | \tilde{a}_{21} \boldsymbol{\gamma}_1 + \tilde{a}_{22} \boldsymbol{\gamma}_2 | \cdots | \tilde{a}_{q1} \boldsymbol{\gamma}_1 + \cdots + \tilde{a}_{qq} \boldsymbol{\gamma}_q] \\ &= [\mathbf{c}_1 | \mathbf{c}_2 | \cdots | \mathbf{c}_q] \end{aligned}$$

where \tilde{a}_{dh} are the elements of the lower triangular matrix \mathbf{A}^{-1} . Hence,

$$\boldsymbol{\gamma}^\top \boldsymbol{\Sigma}_\gamma^{-1} \boldsymbol{\gamma} = [\mathbf{c}_1^\top, \mathbf{c}_2^\top, \dots, \mathbf{c}_q^\top] \begin{bmatrix} \mathbf{Q}_1 & \mathbf{O} & \cdots & \mathbf{O} \\ \mathbf{O} & \mathbf{Q}_2 & \cdots & \mathbf{O} \\ \vdots & \vdots & \ddots & \vdots \\ \mathbf{O} & \mathbf{O} & \cdots & \mathbf{Q}_q \end{bmatrix} \begin{bmatrix} \mathbf{c}_1 \\ \mathbf{c}_2 \\ \vdots \\ \mathbf{c}_q \end{bmatrix} = \sum_{d=1}^q \mathbf{c}_d^\top \mathbf{Q}_d \mathbf{c}_d$$

The log-density of $\boldsymbol{\gamma}$ finally results in:

$$\log(p(\boldsymbol{\gamma} | \boldsymbol{\Sigma}_\gamma)) = -\frac{nq}{2} \log(2\pi) - n \sum_{d=1}^q \log(\mathbf{A}_{dd}) + \frac{1}{2} \sum_{d=1}^q \sum_{i=1}^n \log((\mathbf{\Lambda}_d)_{ii}) - \frac{1}{2} \sum_{d=1}^q \mathbf{c}_d^\top \mathbf{Q}_d \mathbf{c}_d \quad (13)$$

This log-density evaluation is computationally efficient because it requires only one matrix inversion, which pertains to \mathbf{A} . In applications similar to this work, the dimensions of \mathbf{A} are typically small ($q \leq 10$).

Directed graph In this case the determinant of $\boldsymbol{\Sigma}_\gamma^{-1}$ is very simple:

$$|\boldsymbol{\Sigma}_\gamma^{-1}| = |\mathbf{I}_N - \mathbf{A}| \prod_{d=1}^q |\mathbf{Q}_d| |\mathbf{I}_N - \mathbf{A}| = \prod_{d=1}^q |\mathbf{Q}_d| = \prod_{d=1}^q \prod_{i=1}^n (\mathbf{\Lambda}_d)_{ii}$$

where we have exploited the strictly lower triangularity of the $N \times N$ block matrix \mathbf{A} . Now we need to compute $\gamma^T \Sigma_\gamma^{-1} \gamma$:

$$\gamma^T \Sigma_\gamma^{-1} \gamma = \gamma^T (\mathbf{I}_N - \mathbf{A})^T \left[\bigoplus_{d=1}^q \mathbf{Q}_d \right] (\mathbf{I}_N - \mathbf{A}) \gamma$$

where

$$(\mathbf{I}_N - \mathbf{A}) \gamma = \begin{bmatrix} \mathbf{I}_n & \mathbf{O} & \cdots & \mathbf{O} \\ -\mathbf{A}_{21} & \mathbf{I}_n & \cdots & \mathbf{O} \\ \vdots & \vdots & \ddots & \vdots \\ -\mathbf{A}_{q1} & -\mathbf{A}_{q2} & \cdots & \mathbf{I}_n \end{bmatrix} \begin{bmatrix} \gamma_1 \\ \gamma_2 \\ \vdots \\ \gamma_q \end{bmatrix} = \begin{bmatrix} \gamma_1 \\ -\mathbf{A}_{21} \gamma_1 + \gamma_2 \\ \vdots \\ -\mathbf{A}_{q1} \gamma_1 - \cdots - \mathbf{A}_{qq-1} \gamma_{q-1} + \gamma_q \end{bmatrix}$$

Hence

$$\begin{aligned} \gamma^T \Sigma_\gamma^{-1} \gamma &= \begin{bmatrix} \gamma_1 \\ -\mathbf{A}_{21} \gamma_1 + \gamma_2 \\ \vdots \\ -\mathbf{A}_{q1} \gamma_1 - \cdots - \mathbf{A}_{qq-1} \gamma_{q-1} + \gamma_q \end{bmatrix}^T \begin{bmatrix} \mathbf{Q}_1 & \mathbf{O} & \cdots & \mathbf{O} \\ \mathbf{O} & \mathbf{Q}_2 & \cdots & \mathbf{O} \\ \vdots & \vdots & \ddots & \vdots \\ \mathbf{O} & \mathbf{O} & \cdots & \mathbf{Q}_q \end{bmatrix} \begin{bmatrix} \gamma_1 \\ -\mathbf{A}_{21} \gamma_1 + \gamma_2 \\ \vdots \\ -\mathbf{A}_{q1} \gamma_1 - \cdots - \mathbf{A}_{qq-1} \gamma_{q-1} + \gamma_q \end{bmatrix} \\ &= \sum_{d=1}^q \left[\left(\gamma_d - \sum_{h=1}^{d-1} \mathbf{A}_{dh} \gamma_h \right)^T \mathbf{Q}_d \left(\gamma_d - \sum_{h=1}^{d-1} \mathbf{A}_{dh} \gamma_h \right) \right] \end{aligned}$$

In this case the log-density is defined as

$$\begin{aligned} \log(p(\gamma | \Sigma_\gamma)) &= -\frac{nq}{2} \log(2\pi) + \frac{1}{2} \sum_{d=1}^q \sum_{i=1}^n \log((\Lambda_d)_{ii}) \\ &\quad - \frac{1}{2} \sum_{d=1}^q \left[\left(\gamma_d - \sum_{h=1}^{d-1} \mathbf{A}_{dh} \gamma_h \right)^T \mathbf{Q}_d \left(\gamma_d - \sum_{h=1}^{d-1} \mathbf{A}_{dh} \gamma_h \right) \right] \end{aligned}$$

where, it is clear that there is no need to invert any matrices.

Undirected graph Again, the first thing we need to compute is $|\Sigma_\gamma^{-1}|$:

$$|\Sigma_\gamma^{-1}| = \left| \bigoplus_{d=1}^q \mathbf{U}_d \right| |\Lambda_{dis} \otimes \mathbf{I}_n| \left| \bigoplus_{d=1}^q \mathbf{U}_d^T \right| = |\Lambda_{dis}|^n \left(\prod_{d=1}^q |\mathbf{U}_d| \right)^2 = |\Lambda_{dis}|^n \prod_{d=1}^q \prod_{i=1}^n (\Lambda_d)_{ii}$$

where for the computation of $|\mathbf{U}_d|$ we have exploited $\mathbf{U}_d = (\mathbf{I} - \mathbf{B}_d)^T \Lambda_d^{1/2}$ and consequently $|\mathbf{U}_d| = |\mathbf{I} - \mathbf{B}_d| |\Lambda_d^{1/2}| = \prod_{i=1}^n \sqrt{(\Lambda_d)_{ii}}$. Then, it is the turn of $\gamma^T \Sigma_\gamma^{-1} \gamma$:

$$\begin{aligned} \gamma^T \Sigma_\gamma^{-1} \gamma &= \gamma^T \left[\bigoplus_{d=1}^q \mathbf{U}_d \right] (\Lambda_{dis} \otimes \mathbf{I}_n) \left[\bigoplus_{d=1}^q \mathbf{U}_d^T \right] \gamma \\ &= \left(\left[\bigoplus_{d=1}^q \mathbf{U}_d^T \right] \gamma \right)^T (\Lambda_{dis} \otimes \mathbf{I}_n) \left(\left[\bigoplus_{d=1}^q \mathbf{U}_d^T \right] \gamma \right) \end{aligned}$$

In this case, to simplify the expression we need to develop the computations regarding

$$\left[\bigoplus_{d=1}^q \mathbf{U}_d^T \right] \boldsymbol{\gamma} = \begin{bmatrix} \mathbf{U}_1^T & \mathbf{O} & \cdots & \mathbf{O} \\ \mathbf{O} & \mathbf{U}_2^T & \cdots & \mathbf{O} \\ \vdots & \vdots & \ddots & \vdots \\ \mathbf{O} & \mathbf{O} & \cdots & \mathbf{U}_q^T \end{bmatrix} \begin{bmatrix} \gamma_1 \\ \gamma_2 \\ \vdots \\ \gamma_q \end{bmatrix} = \begin{bmatrix} \mathbf{U}_1^T \gamma_1 \\ \mathbf{U}_2^T \gamma_2 \\ \vdots \\ \mathbf{U}_q^T \gamma_q \end{bmatrix}$$

Hence,

$$\begin{aligned} \boldsymbol{\gamma}^T \boldsymbol{\Sigma}_\gamma^{-1} \boldsymbol{\gamma} &= [\boldsymbol{\gamma}_1^T \mathbf{U}_1, \boldsymbol{\gamma}_2^T \mathbf{U}_2, \dots, \boldsymbol{\gamma}_q^T \mathbf{U}_q] \begin{bmatrix} \lambda_{dis,11} \mathbf{I} & \lambda_{dis,12} \mathbf{I} & \cdots & \lambda_{dis,1q} \mathbf{I} \\ \lambda_{dis,21} \mathbf{I} & \lambda_{dis,22} \mathbf{I} & \cdots & \lambda_{dis,2q} \mathbf{I} \\ \vdots & \vdots & \ddots & \vdots \\ \lambda_{dis,q1} \mathbf{I} & \lambda_{dis,q2} \mathbf{I} & \cdots & \lambda_{dis,qq} \mathbf{I} \end{bmatrix} \begin{bmatrix} \mathbf{U}_1^T \gamma_1 \\ \mathbf{U}_2^T \gamma_2 \\ \vdots \\ \mathbf{U}_q^T \gamma_q \end{bmatrix} \\ &= \sum_{d=1}^q \sum_{h=1}^q \lambda_{dis,dh} \boldsymbol{\gamma}_d^T \mathbf{U}_d \mathbf{U}_h^T \boldsymbol{\gamma}_h \end{aligned}$$

Finally the log-density in this case results in:

$$\begin{aligned} \log(p(\boldsymbol{\gamma} | \boldsymbol{\Sigma}_\gamma)) &= -\frac{nq}{2} \log(2\pi) + \frac{1}{2} \sum_{d=1}^q \sum_{i=1}^n \log((\boldsymbol{\Lambda}_d)_{ii}) + \frac{n}{2} \log |\boldsymbol{\Lambda}_{dis}| \\ &\quad - \frac{1}{2} \sum_{d=1}^q \sum_{h=1}^q \lambda_{dis,dh} \boldsymbol{\gamma}_d^T \mathbf{U}_d \mathbf{U}_h^T \boldsymbol{\gamma}_h \end{aligned}$$

Also in this case no matrix inversion is required, since we exploit the DAGAR construction of each spatial precision matrix.

Advantages of the MDAGAR with respect to the MCAR specification When dealing with spatial random effects, computations involving large covariance matrices can be prohibitively expensive, especially due to the cost of evaluating the determinant and quadratic form in the multivariate Gaussian density. The CAR model, with precision matrix $\mathbf{Q} = (\mathbf{D} - \rho \mathbf{W})$, where \mathbf{D} is a diagonal matrix of region-specific neighbor counts and \mathbf{W} is the geographic adjacency matrix, often leverages a computational shortcut: the eigenvalues ω_i of $\mathbf{D}^{-1/2} \mathbf{W} \mathbf{D}^{-1/2}$ are precomputed, allowing the determinant to be expressed as $|\mathbf{Q}| \propto \prod_{i=1}^n (1 - \rho \omega_i)$. This makes density evaluations efficient, provided that the adjacency matrix remains fixed across MCMC iterations. However, if the adjacency structure changes at each iteration, the eigen-decomposition must be recomputed every time, incurring a computational complexity of $\mathcal{O}(n^3)$.

In contrast, the DAGAR model defines the precision matrix as $\mathbf{Q} = (\mathbf{I} - \mathbf{B})^T \boldsymbol{\Lambda} (\mathbf{I} - \mathbf{B})$, where the determinant simplifies to the product of the diagonal entries of $\boldsymbol{\Lambda}$, yielding a computational complexity of only $\mathcal{O}(n)$. While \mathbf{B} and $\boldsymbol{\Lambda}$ must be updated at each MCMC iteration (depending on the current value of a possibly changing adjacency matrix $\widetilde{\mathbf{W}}$), no spectral decomposition is required, allowing for much faster density evaluations. These advantages are further amplified

in the multi-disease setting.

Indeed, in the MDAGAR framework, all spatial log-densities, structured, directed, or undirected, benefit from this simplification: the log-determinant of each disease-specific spatial precision matrix \mathbf{Q}_d reduces to the log of the product of the diagonal entries of $\mathbf{\Lambda}_d$, maintaining an overall complexity of $\mathcal{O}(qn)$ for q diseases and n regions. This is in sharp contrast to the MCAR case, where each $\mathbf{Q}_d = \mathbf{D}_d - \rho_d \mathbf{W}_d$ necessitates the computation of eigenvalues ω_{di} of $\mathbf{D}_d^{-1/2} \mathbf{W}_d \mathbf{D}_d^{-1/2}$, with determinant $|\mathbf{Q}_d| \propto \prod_{i=1}^n (1 - \rho_d \omega_{di})$. Again, if \mathbf{W}_d changes across iterations, the computational cost becomes $\mathcal{O}(qn^3)$ due to the repeated eigendecompositions.

Regarding the quadratic form evaluations, computational complexities diverge based on graph structure. For the undirected MDAGAR, the specific construction of each \mathbf{Q}_d permits an efficient evaluation with complexity $\mathcal{O}(q^2 n^2)$. In contrast, the MCAR formulation requires Cholesky factorization of each \mathbf{Q}_d , leading to a higher complexity of $\mathcal{O}(qn^3 + q^2 n^2)$, where the first term captures the Cholesky cost. In all other cases, the quadratic form computation under MCAR also scales as $\mathcal{O}(q^2 n^2)$, yet without the determinant simplification afforded by the DAGAR approach.

Appendix C: Computational details

C.1 Model Implementation

Letting $\boldsymbol{\eta} = (\boldsymbol{\eta}_1^\top, \dots, \boldsymbol{\eta}_q^\top)^\top$ and $\boldsymbol{\beta} = (\boldsymbol{\beta}_1^\top, \dots, \boldsymbol{\beta}_q^\top)^\top$ for the unstructured disease graph we evaluate the following joint posterior distribution,

$$p(\boldsymbol{\theta}, \boldsymbol{\beta}, \tau, \mathbf{V}, \boldsymbol{\gamma}, \boldsymbol{\rho}, \boldsymbol{\eta}, \mathbf{A} \mid \mathbf{y}) \propto p(\boldsymbol{\theta}, \boldsymbol{\beta}, \tau, \mathbf{V}, \boldsymbol{\gamma}, \boldsymbol{\rho}, \boldsymbol{\eta}, \mathbf{A}) \times \prod_{i=1}^n \prod_{d=1}^q p(y_{id} \mid \boldsymbol{\beta}_d, \phi_{id}), \quad (14)$$

where $\mathbf{y} = (\mathbf{y}_1^\top, \dots, \mathbf{y}_q^\top)^\top$ is $N \times 1$ with $N = nq$, n is the number of geographic regions, and $\mathbf{y}_d = (y_{1d}, \dots, y_{nd})^\top$ and each y_{id} being modeled independently conditional on the spatial random effects using a member from the exponential family. For example, in our simulation experiments in Section 4 of the main manuscript we assume $y_{id} \mid \boldsymbol{\beta}_d, \phi_{id}, \tau_d \stackrel{ind}{\sim} \mathcal{N}(\mathbf{x}_{id}^\top \boldsymbol{\beta}_d + \phi_{id}, 1/\tau_d)$ and specify the joint prior distribution, $p(\boldsymbol{\beta}, \tau_d, \boldsymbol{\theta}, \mathbf{V}, \tau, \boldsymbol{\gamma}, \boldsymbol{\rho}, \boldsymbol{\eta}, \mathbf{A})$ proportional to

$$\begin{aligned} & \mathcal{N}_{qp}(\boldsymbol{\beta} \mid \mathbf{0}, 1/\tau_\beta \mathbf{I}_{qp}) \times \prod_{d=1}^q IG(1/\tau_d \mid a_\epsilon, b_\epsilon) \times \prod_{k=1}^K \{\mathcal{N}(\theta_k \mid 0, 1/\tau) \times \text{Beta}(V_k \mid 1, \alpha)\} \\ & \times IG(1/\tau \mid a, b) \times \mathcal{N}(\boldsymbol{\gamma} \mid \mathbf{0}, \boldsymbol{\Sigma}_\gamma) \times \mathcal{W}^{-1}(\mathbf{A} \mathbf{A}^\top \mid \nu, \boldsymbol{\Psi}) \times \left| \frac{\partial \mathbf{A} \mathbf{A}^\top}{\partial a_{dh}} \right| \\ & \times \prod_{d=1}^q \left\{ \prod_{r=1}^{R_d} \mathcal{U}(\eta_{dr} \mid 0, M_r) \times \mathcal{U}(\rho_d \mid 0, 1) \right\}, \end{aligned} \quad (15)$$

where $\left| \frac{\partial \mathbf{A} \mathbf{A}^\top}{\partial a_{dh}} \right| = 2^q \prod_{d=1}^q a_{dd}^{q-d+1}$ is the Jacobian transformation for the prior on $\mathbf{A} \mathbf{A}^\top$ in terms of the Cholesky factor \mathbf{A} (Olkin and Sampson, 1972), and R_d is the dimension of $\boldsymbol{\eta}_d$. We employ Markov Chain Monte Carlo (MCMC) with Gibbs sampling and random walk Metropo-

lis implemented in `RcppArmadillo` (Eddelbuettel and Sanderson, 2014) statistical computing environment, to draw samples from the posterior distribution, as defined in (14).

The different graphical models discussed above provide parametric structures for \mathbf{A} . Therefore, $\mathcal{W}(\mathbf{A}\mathbf{A}^T | \cdot, \cdot)$ in (15) is replaced with priors in the parameters in \mathbf{A} . In the directed graph, we further model \mathbf{A}_{dh} in terms of parameters $\{\alpha_{0dd'}\}$ and $\alpha_{1dd'}$. These parameters are assigned independent Gaussian prior distributions $\alpha_{0dd'} \stackrel{ind}{\sim} \mathcal{N}(\cdot, \cdot)$ and $\alpha_{1dd'} \stackrel{ind}{\sim} \mathcal{N}(\cdot, \cdot)$, respectively, resulting in a joint prior distribution for $\boldsymbol{\alpha} = (\alpha_{0dd'}, \alpha_{1dd'})_{dd'}$, i.e., $\boldsymbol{\alpha} \sim \mathcal{N}(\mathbf{0}, 100\mathbf{I})$. In the undirected model, the unknown parameter $\rho_{dis} \stackrel{ind}{\sim} \mathcal{U}(\cdot, \cdot)$ completely specifies \mathbf{A} .

C.2 MCMC algorithm

Our models rely on posterior inference, which is achieved through MCMC posterior simulations. To accomplish this, we employ the blocked Gibbs Sampler with some adaptive and some classic Metropolis-Hastings steps, based on the work by Gamerman and Lopes (2006) and Miasojedow et al. (2013). This approach allows us to achieve the desired acceptance rates while updating all random parameters in our model. It is important to note that ϕ_i corresponds to θ_{u_i} , and we update ϕ_i by updating both $\boldsymbol{\theta}$ and u_i , and, ultimately, that $\boldsymbol{\eta}$ is constrained to be between 0 and a positive constant M . The MCMC algorithm proceeds through the following steps, with a noteworthy observation that step 8 is further subdivided into three parts, depending on the selected model used to represent disease dependence. Here, we present the algorithm used for the data analysis described in Section 5. In the simulation setting, there would be an additional step to calculate the error variances, along with the closed-form full conditionals for the error variances, as well as for $\boldsymbol{\beta}$ and $\boldsymbol{\theta}$.

Algorithm 1: Posterior inference of $\boldsymbol{\theta}$, $\boldsymbol{\beta}$, τ_s , \mathbf{V} , $\boldsymbol{\gamma}$, $\boldsymbol{\rho}$, $\boldsymbol{\eta}$ and \mathbf{A} or $\boldsymbol{\alpha}$ or ρ_{dis} based on our models

1: update $\boldsymbol{\beta} | \boldsymbol{\theta}$

- (a) sample candidate $\boldsymbol{\beta}^*$ from $\mathcal{N}(\boldsymbol{\beta}, \xi_{\boldsymbol{\beta}})$
- (b) accept $\boldsymbol{\beta}^*$ with probability

$$\min \left\{ 1, \frac{\exp \left(\sum_{k=1}^K \sum_{i,d:\phi_{id}=\theta_k} y_{id} (\mathbf{x}_{id}^T \boldsymbol{\beta}_d^* + \phi_{id}) - E_{id} \exp (\mathbf{x}_{id}^T \boldsymbol{\beta}_d^* + \phi_{id}) - \frac{\boldsymbol{\beta}_d^{*T} \boldsymbol{\beta}_d^*}{2\sigma_{\boldsymbol{\beta}}^2} \right)}{\exp \left(\sum_{k=1}^K \sum_{i,d:\phi_{id}=\theta_k^*} y_{id} (\mathbf{x}_{id}^T \boldsymbol{\beta}_d + \phi_{id}) - E_{id} \exp (\mathbf{x}_{id}^T \boldsymbol{\beta}_d + \phi_{id}) - \frac{\boldsymbol{\beta}_d^T \boldsymbol{\beta}_d}{2\sigma_{\boldsymbol{\beta}}^2} \right)} \right\}$$

- (c) adapt $\xi_{\boldsymbol{\beta}}$

2: update $\boldsymbol{\theta} | \boldsymbol{\beta}, \tau_s$

- (a) sample candidate $\boldsymbol{\theta}^*$ from $\mathcal{N}(\boldsymbol{\theta}, \xi_{\boldsymbol{\theta}})$
- (b) accept $\boldsymbol{\theta}^*$ with probability

$$\min \left\{ 1, \frac{\exp \left(\sum_{k=1}^K \sum_{i,d:\phi_{id}=\theta_k^*} y_{id} (\mathbf{x}_{id}^T \boldsymbol{\beta}_d + \phi_{id}) - E_{id} \exp (\mathbf{x}_{id}^T \boldsymbol{\beta}_d + \phi_{id}) - \frac{\theta_k^{*2}}{2} \tau_s \right)}{\exp \left(\sum_{k=1}^K \sum_{i,d:\phi_{id}=\theta_k} y_{id} (\mathbf{x}_{id}^T \boldsymbol{\beta}_d + \phi_{id}) - E_{id} \exp (\mathbf{x}_{id}^T \boldsymbol{\beta}_d + \phi_{id}) - \frac{\theta_k^2}{2} \tau_s \right)} \right\}$$

- (c) adapt $\xi_{\boldsymbol{\theta}}$

3: update $\gamma_{id} | \boldsymbol{\beta}, \boldsymbol{\theta}, \boldsymbol{\rho}, \boldsymbol{\eta}, \mathbf{A}$, $i = 1, \dots, n$, $d = 1, \dots, q$

- (a) sample candidate γ_{id}^* from $\mathcal{N}(\gamma_{id}, \xi_{\gamma_{id}})$
- (b) compute the corresponding candidate $u_{id}^* = \sum_{k=1}^K k I \left(\sum_{t=1}^{k-1} p_t < F^{(id)}(\gamma_{id}^*) < \sum_{t=1}^k p_t \right)$
- (c) accept γ_{id}^* with probability

$$\min \left\{ 1, \frac{\exp \left(y_{id} (\mathbf{x}_{id}^T \boldsymbol{\beta}_d + \theta_{u_{id}^*}) - E_i \exp (\mathbf{x}_{id}^T \boldsymbol{\beta}_d + \theta_{u_{id}^*}) - \frac{\boldsymbol{\gamma}^{*T} \boldsymbol{\Sigma}_{\boldsymbol{\gamma}}^{-1} \boldsymbol{\gamma}^*}{2} \right)}{\exp \left(y_{id} (\mathbf{x}_{id}^T \boldsymbol{\beta}_d + \theta_{u_{id}}) - E_{id} \exp (\mathbf{x}_{id}^T \boldsymbol{\beta}_d + \theta_{u_{id}}) - \frac{\boldsymbol{\gamma}^T \boldsymbol{\Sigma}_{\boldsymbol{\gamma}}^{-1} \boldsymbol{\gamma}}{2} \right)} \right\}$$

- (d) adapt $\xi_{\gamma_{id}}$

4: update $\mathbf{V} | \boldsymbol{\beta}, \boldsymbol{\theta}$

- (a) let $\tilde{\mathbf{V}} = \text{logit}(\mathbf{V})$ and sample $\tilde{\mathbf{V}}^*$ from $\mathcal{N}(\tilde{\mathbf{V}}, \xi_{\tilde{\mathbf{V}}})$ then $\mathbf{V}^* = \frac{\exp(\tilde{\mathbf{V}}^*)}{1 + \exp(\tilde{\mathbf{V}}^*)}$
- (b) compute the corresponding candidate $\mathbf{p}^* = (p_1^*, \dots, p_K^*)$ and $\mathbf{u} = \{u_{id}^*\}$
- (c) accept \mathbf{V}^* with probability

$$\min \left\{ 1, \frac{\exp \left(\sum_{i,d} y_{id} (\mathbf{x}_{id}^T \boldsymbol{\beta}_d + \theta_{u_{id}^*}) - E_{id} \exp (\mathbf{x}_{id}^T \boldsymbol{\beta}_d + \theta_{u_{id}^*}) \right) \prod_{k=1}^K (1 - V_k^*)^{(\alpha-1)} \prod_{k=1}^K V_k^* (1 - V_k^*)}{\exp \left(\sum_{i,d} y_{id} (\mathbf{x}_{id}^T \boldsymbol{\beta}_d + \theta_{u_{id}}) - E_{id} \exp (\mathbf{x}_{id}^T \boldsymbol{\beta}_d + \theta_{u_{id}}) \right) \prod_{k=1}^K (1 - V_k)^{(\alpha-1)} \prod_{k=1}^K V_k (1 - V_k)} \right\}$$

- (d) adapt $\xi_{\tilde{\mathbf{V}}}$

5: sample $\tau_s | \boldsymbol{\theta}, \beta_0$ from

$$\Gamma \left(a_s + \frac{K}{2}, b_s + \frac{\sum_{k=1}^K \theta_k^2}{2} \right)$$

6: update $\rho | \gamma, \eta, \mathbf{A}$

- (a) let $\tilde{\rho} = \text{logit}(\rho)$ and sample $\tilde{\rho}^*$ from $\mathcal{N}(\tilde{\rho}, \xi_{\tilde{\rho}})$ then $\rho^* = \frac{\exp(\tilde{\rho}^*)}{1 + \exp(\tilde{\rho}^*)}$
- (b) update Σ_{γ}^* with the proposed ρ^*
- (c) accept $\tilde{\rho}^*$ with probability

$$\min \left\{ 1, \frac{|\Sigma_{\gamma}^*|^{-\frac{N}{2}} \exp\left(-\frac{\gamma^T \Sigma_{\gamma}^{*-1} \gamma}{2}\right) \prod_{d=1}^q \rho_d^* (1 - \rho_d^*)}{|\Sigma_{\gamma}|^{-\frac{N}{2}} \exp\left(-\frac{\gamma^T \Sigma_{\gamma}^{-1} \gamma}{2}\right) \prod_{d=1}^q \rho_d (1 - \rho_d)} \right\}$$

- (d) adapt $\xi_{\tilde{\rho}}$

7: update $\eta | \gamma, \rho, \mathbf{A}$

- (a) let $\tilde{\eta} = \log\left(\frac{\eta}{M - \eta}\right)$ and sample $\tilde{\eta}^*$ from $\mathcal{N}(\tilde{\eta}, \xi_{\tilde{\eta}})$ then $\eta^* = \frac{M \exp(\tilde{\eta}^*)}{1 + \exp(\tilde{\eta}^*)}$
- (b) update Σ_{γ}^* with the proposed η^*
- (c) accept $\tilde{\eta}^*$ with probability

$$\min \left\{ 1, \frac{|\Sigma_{\gamma}^*|^{-\frac{N}{2}} \exp\left(-\frac{\gamma^T \Sigma_{\gamma}^{*-1} \gamma}{2}\right) \prod_{d=1}^q \frac{\exp(\tilde{\eta}_d^*)}{(1 + \exp(\tilde{\eta}_d^*))^2}}{|\Sigma_{\gamma}|^{-\frac{N}{2}} \exp\left(-\frac{\gamma^T \Sigma_{\gamma}^{-1} \gamma}{2}\right) \prod_{d=1}^q \frac{\exp(\tilde{\eta}_d)}{(1 + \exp(\tilde{\eta}_d))^2}} \right\}$$

- (d) adapt $\xi_{\tilde{\eta}}$

8: **Unstructured** update $\mathbf{A} | \gamma, \rho, \eta$

- (a) let diagonal elements $\tilde{a}_{dd} = \log(a_{dd})$ and off-diagonal elements $\tilde{a}_{dh} = a_{dh}$ for $h < d$. Then sample candidates $\tilde{\mathbf{a}}^*$ (lower triangular elements of \mathbf{A}) from $\mathcal{N}(\tilde{\mathbf{a}}, \xi_{\tilde{\mathbf{a}}})$ and set $a_{dd}^* = \exp(\tilde{a}_{dd}^*)$ and for $h < d$, $a_{dh}^* = \tilde{a}_{dh}^*$
- (b) construct the proposed \mathbf{A}^* and update Σ_{γ}^* accordingly
- (c) accept \mathbf{A}^* with probability

$$\min \left\{ 1, \frac{|\Sigma_{\gamma}^*|^{-\frac{N}{2}} \exp\left(-\frac{\gamma^T \Sigma_{\gamma}^{*-1} \gamma}{2}\right) p(\mathbf{A}^*) \prod_{d=1}^q a_{dd}^*}{|\Sigma_{\gamma}|^{-\frac{N}{2}} \exp\left(-\frac{\gamma^T \Sigma_{\gamma}^{-1} \gamma}{2}\right) p(\mathbf{A}) \prod_{d=1}^q a_{dd}} \right\}$$

- (d) adapt $\xi_{\tilde{\mathbf{a}}}$

Directed sample $\alpha_d | \gamma, \rho_d$ from

$$\mathcal{N}(\mathbf{H}_d \mathbf{h}_d, H_d)$$

where $\mathbf{H}_d = (\delta_d^T Q_d \delta_d + \Sigma_{\alpha}^{-1})^{-1}$ and $\mathbf{h}_d = \delta_d^T Q_d \gamma_d + \Sigma_{\alpha}^{-1} \mu_{\alpha}$. Here $\delta_d = (F_h)_{h \in N_d}$, $F_h = (\gamma_h, \zeta_h)$, $N_d = \{h : h \sim d, h < d\}$ and $\zeta_h = (\sum_{j \sim 1} \gamma_{h,j}, \dots, \sum_{j \sim n} \gamma_{h,j})$. Then update $\mathbf{A}_{d,h}$ matrices and consequently Σ_{γ} .

Undirected update $\rho_{dis} | \gamma, \rho, \eta$

- (a) let $\tilde{\rho}_{dis} = \log\left(\frac{\rho_{dis} + 1}{1 - \rho_{dis}}\right)$ and sample $\tilde{\rho}_{dis}^*$ from $\mathcal{N}(\tilde{\rho}_{dis}, \xi_{\tilde{\rho}_{dis}})$ then $\rho_{dis}^* = \frac{\exp(\tilde{\rho}_{dis}^*) - 1}{1 + \exp(\tilde{\rho}_{dis}^*)}$
- (b) update Λ_{dis}^* with the proposed ρ_{dis}^* and then Σ_{γ}^*
- (c) accept $\tilde{\rho}_{dis}^*$ with probability

$$\min \left\{ 1, \frac{|\Sigma_{\gamma}^*|^{-\frac{N}{2}} \exp\left(-\frac{\gamma^T \Sigma_{\gamma}^{*-1} \gamma}{2}\right) \frac{\exp(\tilde{\rho}_{dis}^*)}{(1 + \exp(\tilde{\rho}_{dis}^*))^2}}{|\Sigma_{\gamma}|^{-\frac{N}{2}} \exp\left(-\frac{\gamma^T \Sigma_{\gamma}^{-1} \gamma}{2}\right) \frac{\exp(\tilde{\rho}_{dis})}{(1 + \exp(\tilde{\rho}_{dis}))^2}} \right\}$$

- (d) adapt $\xi_{\tilde{\rho}_{dis}}$

Appendix D: Simulations

Table 4: Root median squared error for all the model parameters under all the simulation settings.

True graph	Unstructured			Directed			Undirected		
Fitted graph	Unstructured	Directed	Undirected	Unstructured	Directed	Undirected	Unstructured	Directed	Undirected
β	1.877	1.513	1.411	1.867	1.733	1.364	1.791	1.691	1.435
ϕ_1	9.803	7.030	30.906	9.094	8.640	7.547	8.187	7.684	6.765
ϕ_2	9.829	6.868	30.574	7.253	8.633	6.747	8.722	8.101	6.774
ϕ_3	8.865	6.994	30.337	7.140	8.595	6.989	8.034	8.033	6.710
ϕ_4	8.245	9.182	30.608	7.041	8.888	7.127	7.782	8.750	6.591
γ_1	7.840	8.312	8.304	8.168	8.119	7.845	7.610	8.158	7.726
γ_2	12.553	11.250	11.033	14.883	13.881	13.516	4.647	5.233	4.409
γ_3	14.564	13.726	13.772	31.599	27.919	28.247	7.321	7.372	6.935
γ_4	17.855	17.845	15.431	47.202	44.768	44.390	7.312	7.455	6.513
θ	15.566	15.470	16.032	15.510	15.716	15.457	15.328	15.857	15.599
τ_{dis}	793.454	799.987	814.658	763.119	758.193	766.614	839.689	845.071	835.940
\mathbf{V}	0.752	0.645	0.605	0.746	0.617	0.603	0.745	0.605	0.623
τ	0.046	0.053	0.044	0.044	0.047	0.050	0.043	0.042	0.039
ρ	0.836	0.852	0.867	0.840	0.852	0.842	0.853	0.877	0.907
η	0.359	0.381	0.383	0.374	0.408	0.428	0.347	0.400	0.417
\mathbf{A}	7.346	-	-	-	-	-	-	-	-
α	-	-	-	-	2.112	-	-	-	-
ρ_{dis}	-	-	-	-	-	-	-	-	0.250

Table 5: Boundary detection results in the simulation study with DAGAR spatial dependence for the three disease graph models with data generated under the corresponding true model.

Disease graph	T	Disease 1		Disease 2		Disease 3		Disease 4	
		Specificity	Sensitivity	Specificity	Sensitivity	Specificity	Sensitivity	Specificity	Sensitivity
Unstructured	85	0.835	0.860	0.824	0.886	0.848	0.902	0.909	0.908
	90	0.821	0.872	0.796	0.899	0.813	0.915	0.892	0.915
	95	0.798	0.888	0.764	0.915	0.789	0.922	0.869	0.923
	100	0.762	0.904	0.727	0.926	0.755	0.931	0.832	0.934
	105	0.715	0.920	0.676	0.938	0.706	0.945	0.782	0.943
Directed	85	0.899	0.871	0.859	0.927	0.746	0.937	0.744	0.929
	90	0.875	0.878	0.830	0.934	0.681	0.943	0.696	0.934
	95	0.856	0.890	0.773	0.941	0.636	0.949	0.639	0.943
	100	0.827	0.901	0.722	0.950	0.563	0.955	0.572	0.952
	105	0.790	0.917	0.650	0.956	0.486	0.961	0.490	0.962
Undirected	85	0.961	0.891	0.956	0.891	0.957	0.893	0.954	0.885
	90	0.954	0.898	0.949	0.898	0.950	0.898	0.947	0.890
	95	0.942	0.905	0.939	0.906	0.937	0.902	0.936	0.898
	100	0.922	0.914	0.922	0.914	0.919	0.910	0.912	0.909
	105	0.897	0.925	0.895	0.926	0.888	0.921	0.888	0.922

Table 6: Boundary detection results in the simulation study with CAR spatial dependence for the three disease graph models with data generated under the corresponding true model.

Disease graph	T	Disease 1		Disease 2		Disease 3		Disease 4	
		Specificity	Sensitivity	Specificity	Sensitivity	Specificity	Sensitivity	Specificity	Sensitivity
Unstructured	85	0.859	0.897	0.855	0.890	0.843	0.874	0.832	0.879
	90	0.838	0.905	0.834	0.899	0.820	0.885	0.817	0.887
	95	0.821	0.915	0.818	0.907	0.795	0.895	0.798	0.895
	100	0.800	0.925	0.790	0.916	0.771	0.908	0.777	0.906
	105	0.769	0.936	0.751	0.927	0.738	0.920	0.741	0.922
Directed	85	0.902	0.873	0.920	0.897	0.843	0.895	0.783	0.873
	90	0.894	0.880	0.897	0.908	0.808	0.908	0.737	0.890
	95	0.884	0.891	0.876	0.918	0.758	0.920	0.685	0.903
	100	0.860	0.902	0.840	0.929	0.691	0.934	0.623	0.918
	105	0.822	0.915	0.791	0.942	0.623	0.946	0.538	0.935
Undirected	85	0.950	0.880	0.926	0.893	0.936	0.894	0.938	0.889
	90	0.942	0.888	0.904	0.903	0.925	0.900	0.924	0.897
	95	0.929	0.899	0.873	0.913	0.908	0.908	0.904	0.906
	100	0.906	0.912	0.837	0.924	0.876	0.917	0.872	0.916
	105	0.868	0.924	0.789	0.938	0.833	0.928	0.823	0.929

Table 7: Adjacencies detection with DAGAR spatial dependence for the three disease graph models with data generated under the corresponding true model.

Disease graph	Disease 1		Disease 2		Disease 3		Disease 4	
	Specificity	Sensitivity	Specificity	Sensitivity	Specificity	Sensitivity	Specificity	Sensitivity
Unstructured	0.321	0.987	0.647	0.927	0.625	0.961	0.283	1.000
Directed	0.341	0.994	0.580	0.943	0.464	0.969	0.173	1.000
Undirected	0.327	0.991	0.580	0.935	0.512	0.950	0.177	1.000

Table 8: Adjacencies detection with CAR spatial dependence for the three disease graph models with data generated under the corresponding true model.

Disease graph	Disease 1		Disease 2		Disease 3		Disease 4	
	Specificity	Sensitivity	Specificity	Sensitivity	Specificity	Sensitivity	Specificity	Sensitivity
Unstructured	0.204	0.995	0.440	0.959	0.463	0.955	0.342	1.000
Directed	0.132	1.000	0.389	0.964	0.225	0.986	0.153	1.000
Undirected	0.285	0.979	0.466	0.923	0.376	0.946	0.164	1.000

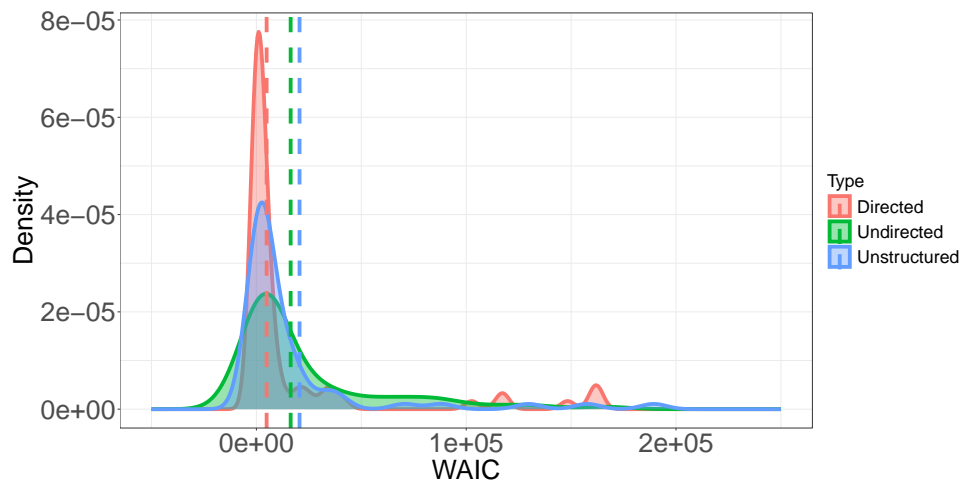


Figure 10: WAIC densities along with the median values (dotted lines) in the DAGAR spatial dependence case for different choices of the disease graph with data generated under the corresponding true model.

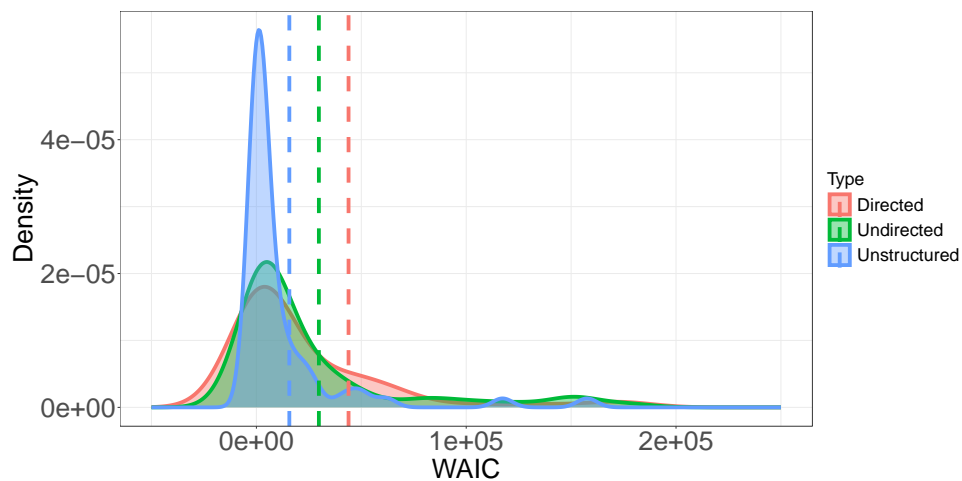


Figure 11: WAIC densities along with the median values (dotted lines) in the CAR spatial dependence case for different choices of the disease graph with data generated under the corresponding true model.

Appendix E: Posterior summaries for SEER data analysis

We present further analysis for the model used in Section 5 of the main article. In this section the regression model $\mathbf{x}_{ij}^T \boldsymbol{\beta}_j$ consists of only cancer-specific intercepts while z_{ij} in the adjacency model is built from the absolute differences between geographic neighbors for the three covariates described in Section 2 of the main article. We present posterior means and standard deviations in Table 9 and credible intervals in Fig. 12, 13, 14 and 15.

Monte Carlo estimates, whether for Markov chain Monte Carlo output or any other purpose, should be accompanied by Monte Carlo standard error as a measure of reliability of posterior inference based on the estimates from the Monte Carlo samples. If the central limit theorem applies, then the corresponding covariance matrices' estimates must be reported, either directly or indirectly. Due to the correlation between the obtained samples, these quantities necessitate more advanced tools compared to typical sample estimators. The validity of a central limit theorem is not guaranteed in all cases because it depends on the convergence rate of the underlying Markov chain. Nonetheless, this assumption is also made when employing various convergence diagnostics. We use the `mcmcse` R package (Flegal et al., 2021) to compute Monte Carlo standard errors and the effective sample size, based on Gong and Flegal (2016) to demonstrate that we can maintain control over the Monte Carlo error by applying a predefined threshold Vats et al. (2019).

Table 9 presents the estimates of the model described in Section 5 including only cancer-specific intercepts in the regression model and the 3 covariates described in Section 2 of the main article in the adjacency model. The last column of Table 9 presents Monte Carlo standard errors with the only value higher than 0.05, the usual threshold, being 0.061. We compute the multivariate effective sample size of the chain to be 1847.068 using the formula $B \frac{|\Lambda|^{1/p}}{|\Sigma|^{1/p}}$. Here, B is the total number of iterations post burn-in, Λ represents the sample covariance matrix, and Σ is an estimate of the Monte Carlo standard error. This computation accounts for the multivariate dependence structure of the process. Comparing our effective sample size to the minimum requirement of 7,619 for achieving a precision level relative to the variability in the target distribution of 0.05, we observe that ours is significantly lower. However, it is important to note that we computed the precision level of our estimate, obtained with an estimated effective sample size of 1847.068, which amounts approximately to 0.01 and, while higher than precision levels used in simpler models, is still deemed acceptable for the inference we draw using these complex hierarchical models.

Table 9: Posterior estimates, posterior standard deviations and Monte Carlo standard errors for the regression coefficients, atoms and their precision in the hierarchical model described (14) using the Poisson regression model described in Section 5 of the main article. Here, β_1 through β_4 denote the intercepts corresponding to lung, esophageal, larynx and colorectal, respectively. The θ 's denote the atoms and τ is the precision in the prior of the θ_k 's as described in Section 3.1. While none of the intercepts are significant, we note that lung and esophageal cancers reveal positive estimates indicating higher expected counts than the standardized rates, E_{id} defined in Section 2 and introduced in the model in Section 5, while larynx and colorectal exhibit negative estimates indicating lower expected counts than their standardized rates.

Variable	Estimate	Standard deviation	Monte Carlo Standard Errors
β_1	0.022	0.027	0.006
β_2	0.075	0.033	0.005
β_3	-0.026	0.037	0.005
β_4	-0.045	0.030	0.007
θ_1	0.072	0.030	0.007
θ_2	-0.283	0.043	0.007
θ_3	-0.098	0.029	0.006
θ_4	-0.020	0.031	0.007
θ_5	0.156	0.162	0.027
θ_6	-0.072	0.175	0.061
θ_7	0.365	0.041	0.009
θ_8	-0.115	0.085	0.020
θ_9	0.312	0.086	0.023
θ_{10}	0.178	0.062	0.019
θ_{11}	-0.149	0.170	0.029
θ_{12}	-0.158	0.028	0.006
θ_{13}	0.184	0.037	0.007
θ_{14}	0.095	0.139	0.032
θ_{15}	0.010	0.029	0.006
τ	7.246	2.368	0.024

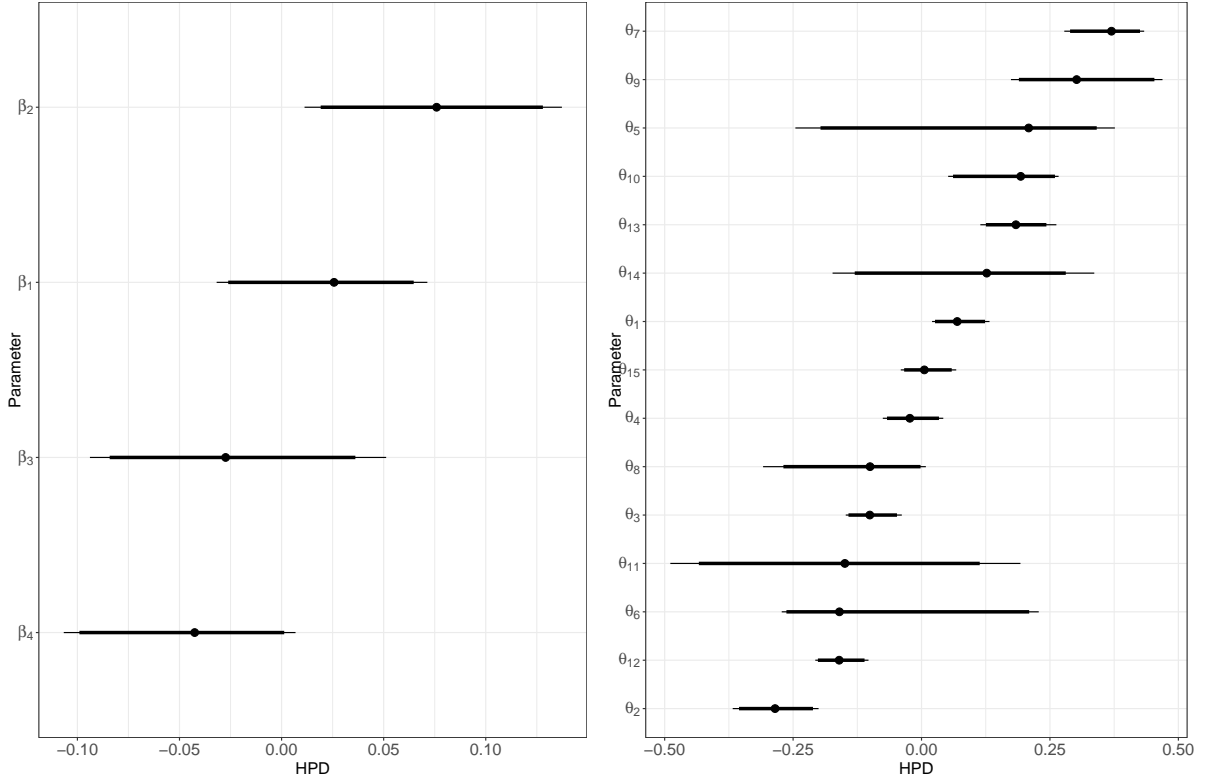


Figure 12: Highest posterior density (HPD) intervals at 90% (thick lines) and 95% (thin lines) levels for β (left panel) and θ (right panel). These are ordered according to their posterior medians. As with the posterior means in Table 9, we see β_1 (lung) and β_2 (esophageal) having positive posterior medians with substantial mass greater than 0, while β_3 (larynx) and β_4 (colorectal) having negative posterior medians with substantial mass less than 0. The 90% interval for colorectal cancer is almost entirely to the left of 0. Turning to the right panel, we see about 4 atoms (θ_2 , θ_{12} , θ_3 and θ_8) to have their HPD intervals almost entirely to the left of 0, while 5 atoms (θ_1 , θ_{13} , θ_{10} , θ_9 and θ_7) have intervals situated entirely to the right of 0. The remaining 6 atoms (out of a total of $K = 15$) are not significantly different from 0. The variation in the posterior distribution of these atoms reflect substantial posterior learning and information from the data that propagates to the spatial random effects.

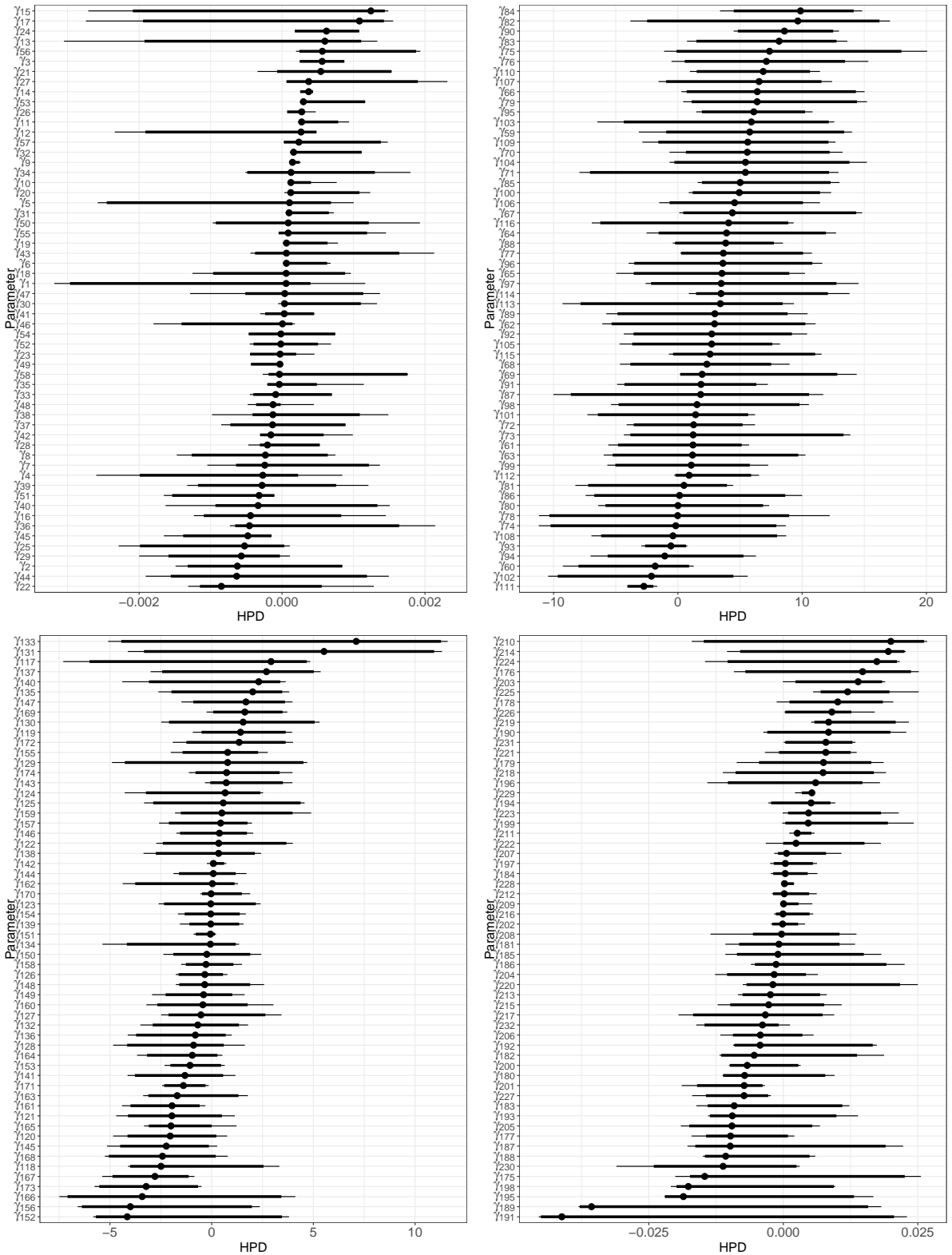


Figure 13: Highest posterior density (HPD) intervals at 90% (thick lines) and 95% (thin lines) levels for the elements of the disease-specific spatial effects in γ using the MDAGAR specification in Section 3.3.1 and the precision matrix given in Eq. 5. The four panels correspond to the 4 cancers: lung (top left), esophageal (top right), larynx (bottom left) and colorectal (bottom right). The intervals are arranged in increasing order of value for posterior medians. It is expected that the intervals for these random effects will mostly not be significantly different from 0, but they reveal substantial variation indicating enough information in the data to discern spatial patterns. It is worth pointing out that the dispersion varies substantially among the cancers with the intervals for lung and colorectal spanning a range much smaller than esophageal and larynx.

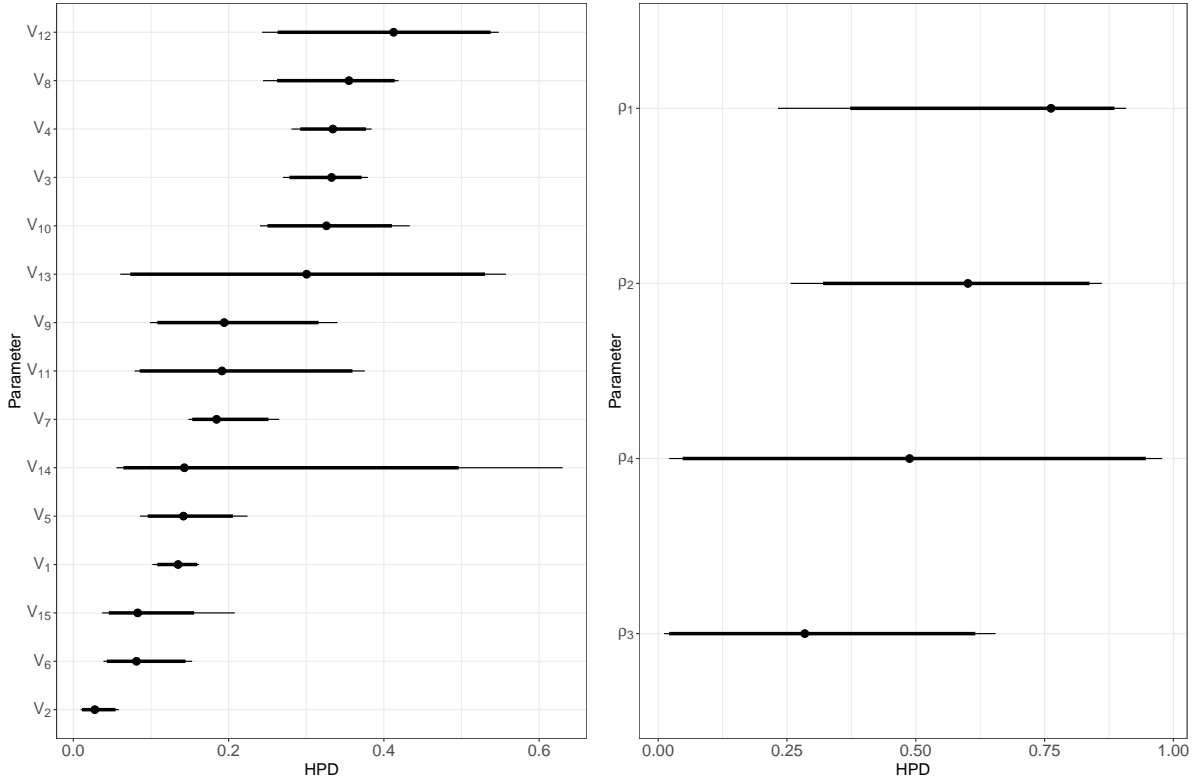


Figure 14: Highest posterior density (HPD) intervals at 90% (thick lines) and 95% (thin lines) levels for \mathbf{V} (left panel), which consists of the 15 stick-breaking weights used in Eq. (3.1), and for $\boldsymbol{\rho}$ (right panel), which consists of the 4 spatial autocorrelation parameters (one for each disease) in the MDAGAR model. These intervals are arranged in increasing order of posterior medians. The variations among these posterior intervals indicate substantial learning from the data that informs the joint distribution of the spatial effects through the stick-breaking probabilities and the baseline MDAGAR distribution in the DP.

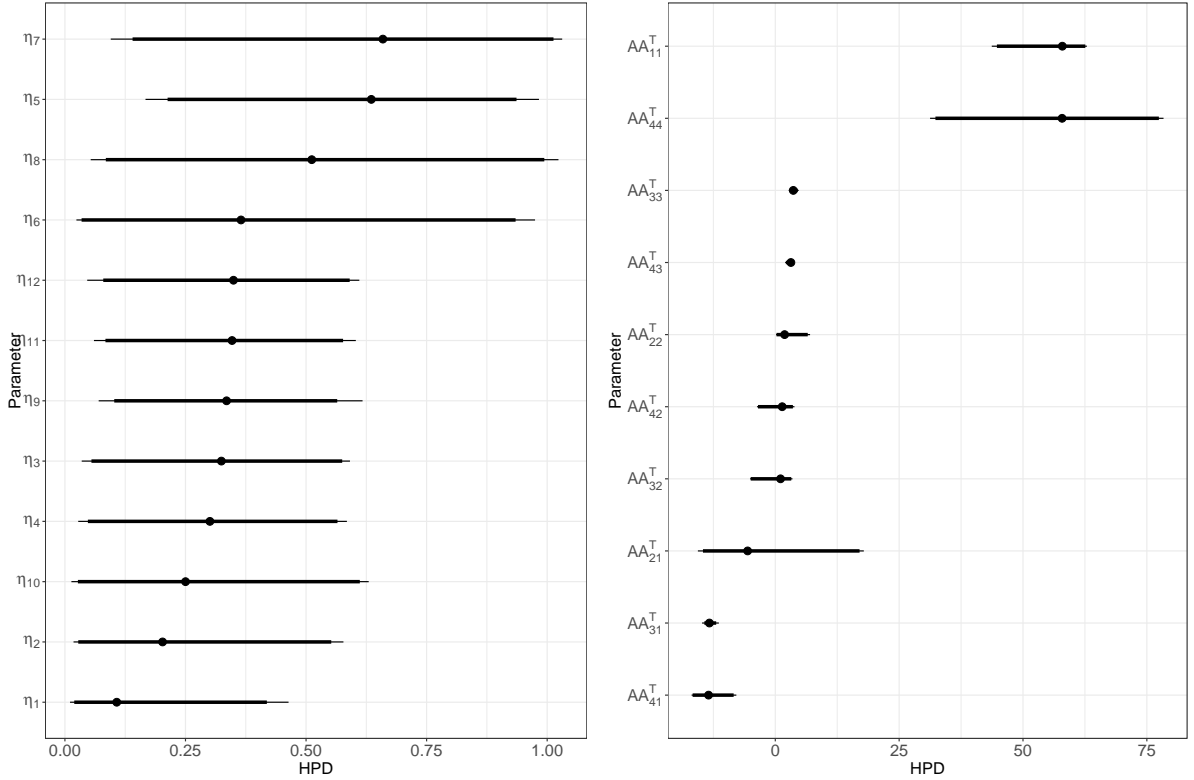


Figure 15: Highest posterior density (HPD) intervals at 90% (thick lines) and 95% (thin lines) levels for $\boldsymbol{\eta}$ (left panel) and \mathbf{A} (right panel). The 12 coefficients in $\boldsymbol{\eta}$ include 3 slopes for each of the 4 cancer types corresponding to the covariates shown in Figure 3. For each of the 4 cancers, these parameters appear in (4) as coefficients of the 3×1 vector \mathbf{z}_{ij} , where the elements of \mathbf{z}_{ij} are $|z_{ki} - z_{kj}|$ for $k = 1, 2, 3$ corresponding to the 3 covariates. The four slopes corresponding to smoking are denoted as η_1, η_4, η_7 , and η_{10} . For the variable 'population over 65', the corresponding slopes are η_2, η_5, η_8 , and η_{11} . The slopes related to poverty levels are η_3, η_6, η_9 , and η_{12} . For all cancers considered, these coefficients correspond respectively to lung, esophageal, laryngeal, and colorectal cancers. Here, the greater the η 's, the more likely two regions are not considered to be adjacent by the model. For instance, the smoking covariate plays a significant role in determining adjacencies for larynx cancer (η_7), while the over 65 covariate has a similar impact for both esophageal and larynx cancers (η_5 and η_8). Additionally, the below poverty covariate appears to have a notable effect on the adjacencies related to esophageal cancer (η_6). In the right panel, the HPD intervals for the elements of $\mathbf{A}\mathbf{A}^T$ are shown, representing the non-spatial covariance among the cancers. Lung and larynx cancers exhibit the highest variances $(\mathbf{A}\mathbf{A}^T)_{11}$ and $(\mathbf{A}\mathbf{A}^T)_{44}$, with larynx showing the widest interval. The non-spatial association between lung and larynx captured by $(\mathbf{A}\mathbf{A}^T)_{41}$ and that between lung and colorectal captured by $(\mathbf{A}\mathbf{A}^T)_{31}$ are negative with the 95% intervals situated entirely below 0. It is important to interpret the non-spatial component of these associations with caution. What can, perhaps, be gleaned from these negative non-spatial associations is a phenomenon of spatial confounding at the residual scale, where much of the positive associations among these aggregated data are absorbed by the spatial associations arising from geographic proximity.

Appendix F: Additional figures and tables



Figure 16: California map with county names. This will be helpful in detecting the boundaries.

F.1 Analysis with covariates in the mean and adjacency model

We present inference from the model used in Section 5 of the main article, where we include cancer-specific intercepts and slopes for the three covariates described in Section 2 of the main article and also include the covariates in the adjacency model. Table 10 presents the estimates of the model described in Section 5 including only cancer-specific intercepts in the regression model and the 3 covariates described in Section 2 of the main article in the adjacency model. The last column of Table 10 presents Monte Carlo standard errors corresponding to the parameter estimates.

Table 10: Posterior estimates, standard deviations and their Monte Carlo standard errors for the regression coefficients, atoms and their precision in the hierarchical model in (14). Here, β_1 through β_4 denote the regression coefficient corresponding to lung, β_5 through β_8 to esophageal, β_9 through β_{12} to larynx and β_{13} through β_{16} colorectal, respectively. The θ 's denote the atoms and τ is the precision in the prior of the θ_k 's as described in Section 3.1. While the intercepts regarding esophageal, larynx and colorectal (β_5 , β_9 and β_{13}) are significant, we note that lung intercept is not. Moreover, across cancers the smoking covariate always reveal positive estimates (β_2 , β_6 , β_{10} and β_{14}) while over 65 and below poverty covariates do not show such a consistent behavior. This indicates that the smoking covariate has a positive impact on the count means across the cancers.

Variable	Estimate	Standard deviation	Monte Carlo Standard Error
β_1	-0.068	0.037	0.003
β_2	0.029	0.002	$< 10^{-3}$
β_3	-0.011	0.002	$< 10^{-3}$
β_4	-0.009	0.002	$< 10^{-3}$
β_5	-0.361	0.109	0.009
β_6	0.034	0.007	$< 10^{-3}$
β_7	0.010	0.007	$< 10^{-3}$
β_8	-0.010	0.006	$< 10^{-3}$
β_9	-0.394	0.132	0.008
β_{10}	0.032	0.008	0.001
β_{11}	0.000	0.009	$< 10^{-3}$
β_{12}	0.004	0.007	$< 10^{-3}$
β_{13}	0.156	0.052	0.007
β_{14}	0.013	0.002	$< 10^{-3}$
β_{15}	-0.018	0.004	$< 10^{-3}$
β_{16}	-0.006	0.002	$< 10^{-3}$
θ_1	0.021	0.024	0.005
θ_2	0.190	0.077	0.011
θ_3	-0.223	0.060	0.010
θ_4	0.168	0.198	0.029
θ_5	-0.082	0.234	0.030
θ_6	0.209	0.136	0.018
θ_7	-0.081	0.290	0.030
θ_8	0.259	0.139	0.015
θ_9	0.061	0.307	0.036
θ_{10}	-0.071	0.241	0.034
θ_{11}	0.115	0.034	0.007
θ_{12}	-0.144	0.029	0.007
θ_{13}	0.175	0.048	0.008
θ_{14}	0.132	0.145	0.018
θ_{15}	-0.082	0.025	0.005
τ	6.979	2.336	0.026

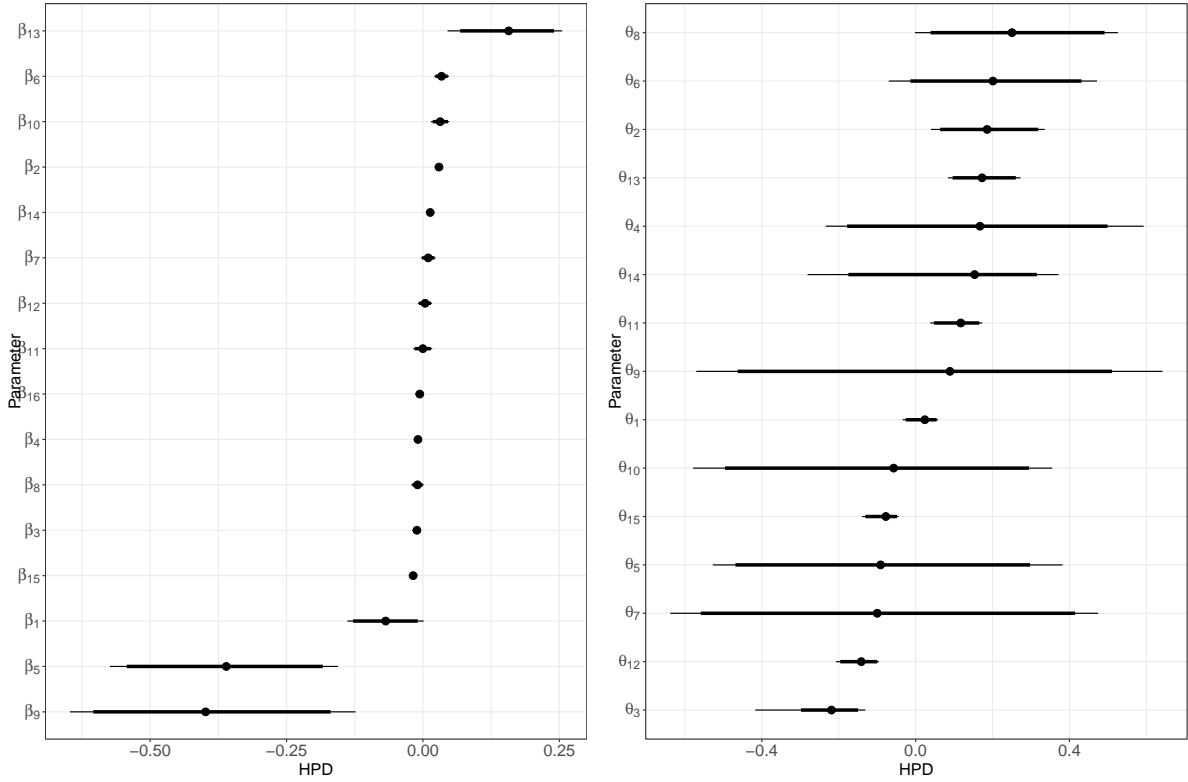


Figure 17: Highest posterior density (HPD) intervals at 90% (thick lines) and 95% (thin lines) levels for β (left panel) and θ (right panel). These are ordered according to their posterior medians. As with the posterior means in Table 10, we see the intercepts regarding esophageal and larynx (β_5 and β_9) having negative posterior medians with the 95% interval entirely to the left of 0, colorectal (β_{13}) having positive posterior medians with the 95% interval entirely to the right of 0 and lung (β_1) with a much smaller negative effect with the 95% interval almost including the 0. All of the others regression coefficients have much smaller intervals with the median estimates very close to 0. Turning to the right panel, we see about 3 atoms (θ_3 , θ_{12} and θ_{15}) to have their HPD intervals almost entirely to the left of 0, while 4 atoms (θ_2 , θ_8 , θ_{11} and θ_{13}) have intervals situated entirely to the right of 0. The remaining 8 atoms (out of a total of $K = 15$) are not significantly different from 0. The variation in the posterior distribution of these atoms reflect substantial posterior learning and information from the data that propagates to the spatial random effects.

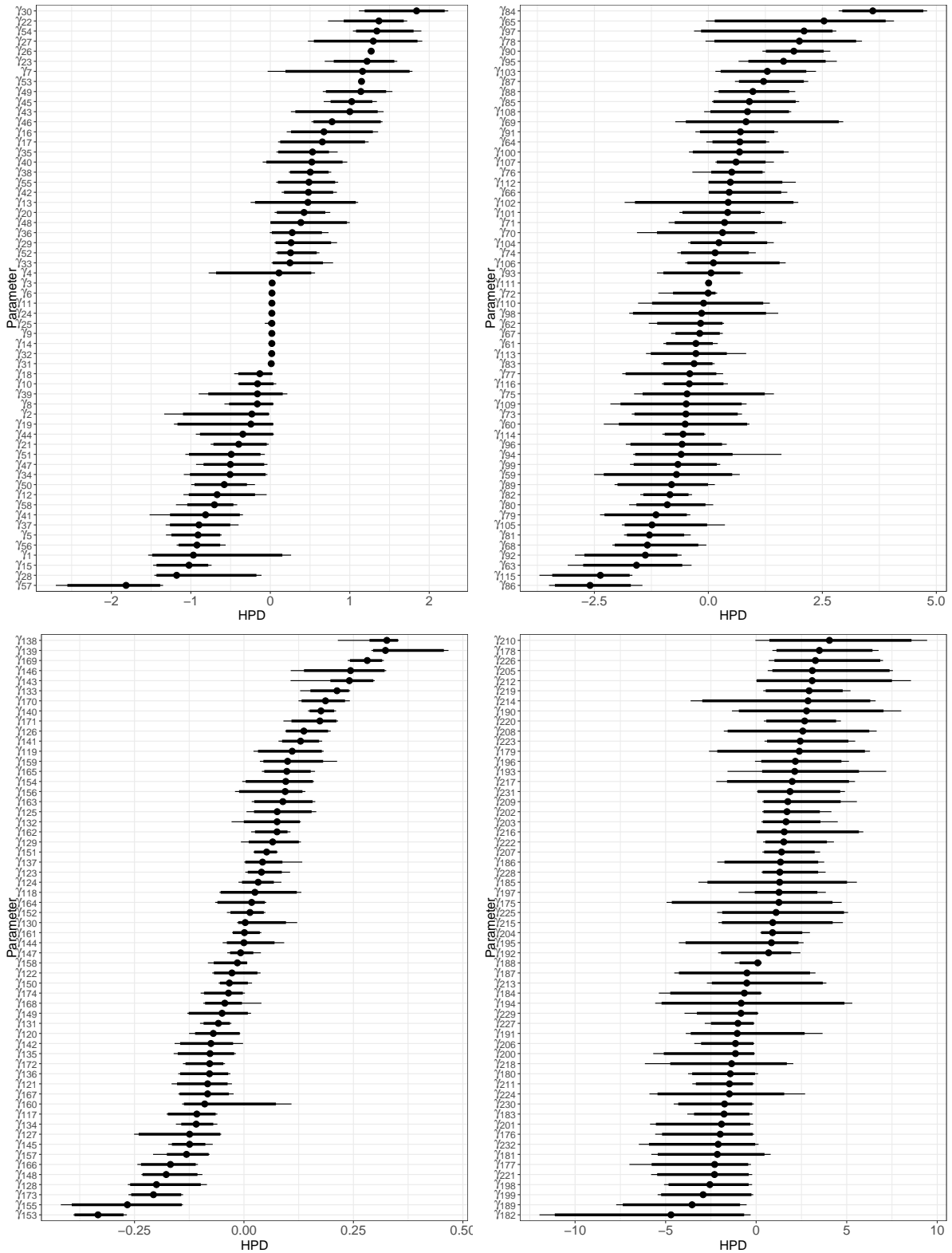


Figure 18: Highest posterior density (HPD) intervals at 90% (thick lines) and 95% (thin lines) levels for the elements of the disease-specific spatial effects in γ using the MDAGAR specification in Section 3.3.1 and the precision matrix given in Eq. 5. The four panels correspond to the 4 cancers: lung (top left), esophageal (top right), larynx (bottom left) and colorectal (bottom right). The intervals are arranged in increasing order of value for posterior medians. It is expected that the intervals for these random effects will mostly not be significantly different from 0, but they reveal substantial variation indicating enough information in the data to discern spatial patterns. It is worth pointing out that the degree of dispersion varies significantly among different cancers. For instance, the intervals for lung and esophageal cancers cover similar ranges, while those for laryngeal cancer are much narrower, and those for colorectal cancer are much wider.

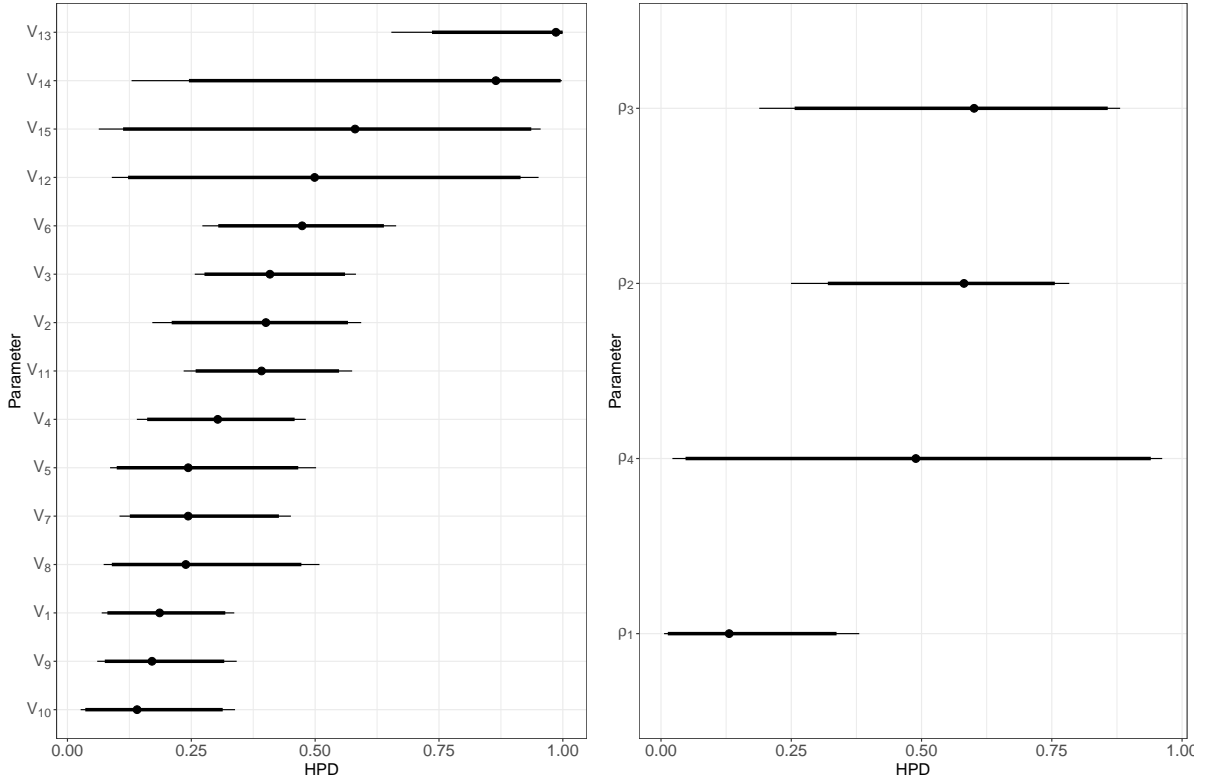


Figure 19: Highest posterior density (HPD) intervals at 90% (thick lines) and 95% (thin lines) levels for \mathbf{V} (left panel), which consists of the 15 stick-breaking weights used in Eq. (3.1), and for $\boldsymbol{\rho}$ (right panel), which consists of the 4 spatial autocorrelation parameters (one for each disease) in the MDAGAR model. These intervals are arranged in increasing order of posterior medians. The variations among these posterior intervals indicate substantial learning from the data that informs the joint distribution of the spatial effects through the stick-breaking probabilities and the baseline MDAGAR distribution in the DP.

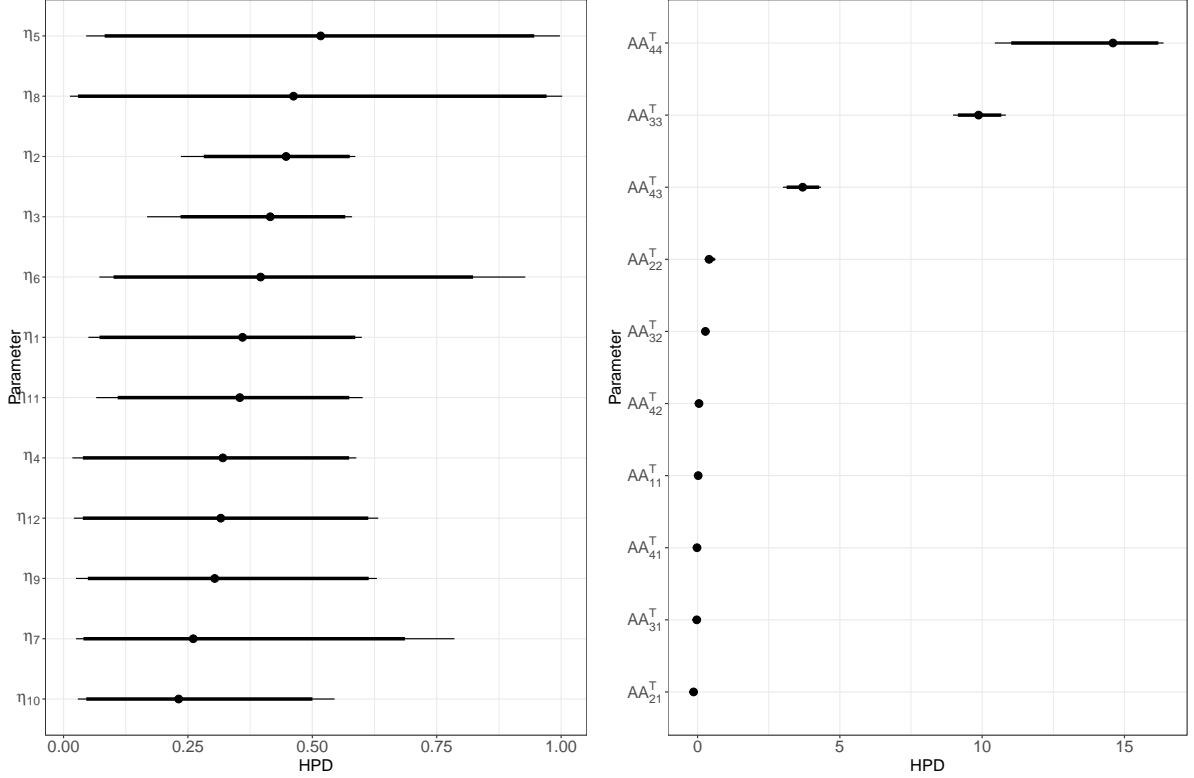


Figure 20: Highest posterior density (HPD) intervals at 90% (thick lines) and 95% (thin lines) levels for $\boldsymbol{\eta}$ (left panel) and \mathbf{A} (right panel). The 12 coefficients in $\boldsymbol{\eta}$ include 3 slopes for each of the 4 cancer types corresponding to the covariates shown in Figure 3. For each of the 4 cancers, these parameters appear in (4) as coefficients of the 3×1 vector \mathbf{z}_{ij} , where the elements of \mathbf{z}_{ij} are $|z_{ki} - z_{kj}|$ for $k = 1, 2, 3$ corresponding to the 3 covariates. The four slopes corresponding to smoking are denoted as η_1, η_4, η_7 , and η_{10} . For the variable 'population over 65', the corresponding slopes are η_2, η_5, η_8 , and η_{11} . The slopes related to poverty levels are η_3, η_6, η_9 , and η_{12} . For all cancers considered, these coefficients correspond respectively to lung, esophageal, laryngeal, and colorectal cancers. Here, the greater the η 's, the more likely two regions are not considered to be adjacent by the model. For example, the over 65 covariate influences the adjacency assessment similarly for both esophageal and larynx cancers (η_5 and η_8), while it plays a more significant role in determining adjacencies for lung cancer (η_2). Additionally, the below poverty covariate appears to have a considerable impact on the adjacencies associated with lung cancer as well (η_3). In the right panel, the HPD intervals for the elements of $\mathbf{A}\mathbf{A}^T$ are shown, representing the non-spatial covariance among the cancers. Colorectal and larynx cancers exhibit the highest variances ($(\mathbf{A}\mathbf{A}^T)_{44}$ and $(\mathbf{A}\mathbf{A}^T)_{33}$), with colorectal showing the widest interval. Colorectal and larynx reveal a significantly positive non-spatial component of their association ($(\mathbf{A}\mathbf{A}^T)_{43}$) but, as in Fig. 15, we recommend caution in interpreting the value of these associations since much of the positive associations among these aggregated data are explained by shared risk factors that are also absorbed into geographic neighbors.

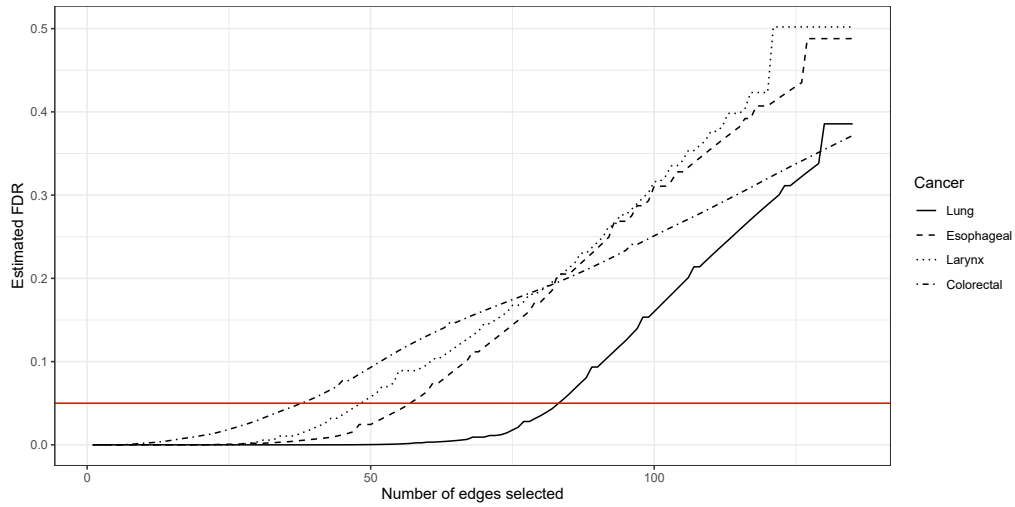


Figure 21: Estimated FDR curves plotted against the number of selected difference boundaries for the four cancers

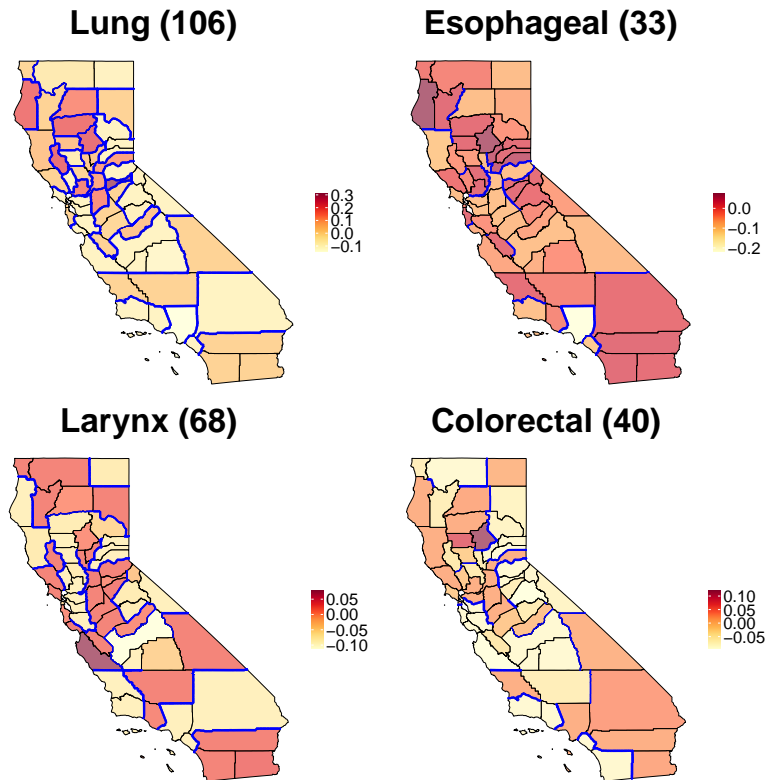


Figure 22: Difference boundaries (highlighted in red) detected by the model in the California map, colored according to the posterior mean of the corresponding ϕ_{id} , for four cancers individually when $\zeta = 0.05$. The values in brackets are the number of difference boundaries detected.

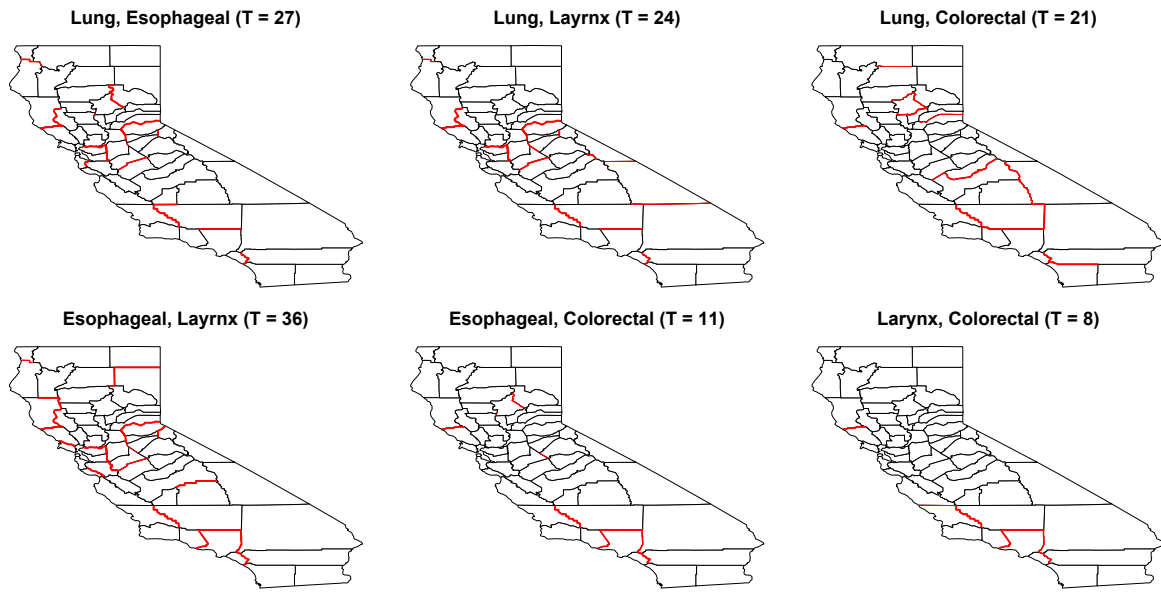


Figure 23: Shared difference boundaries (highlighted in red) detected by the model for each pair of cancers in California map when $\zeta = 0.05$. The values in brackets are the number of difference boundaries detected.

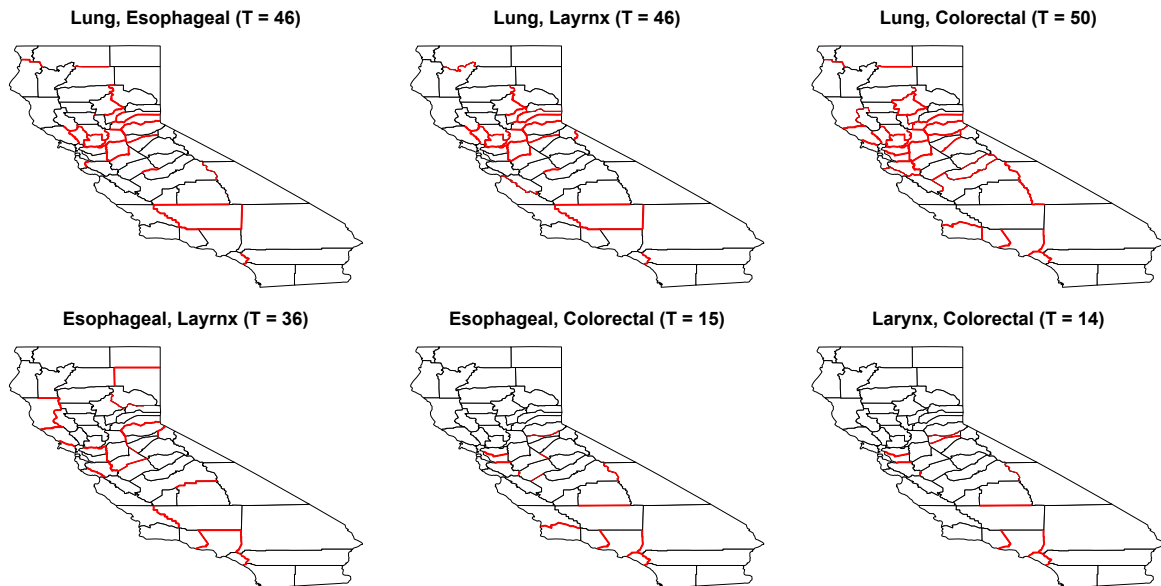


Figure 24: Mutual cross-difference boundaries (highlighted in red) detected by the model for each pair of cancers in California map when $\zeta = 0.05$. The values in brackets are the number of difference boundaries detected.

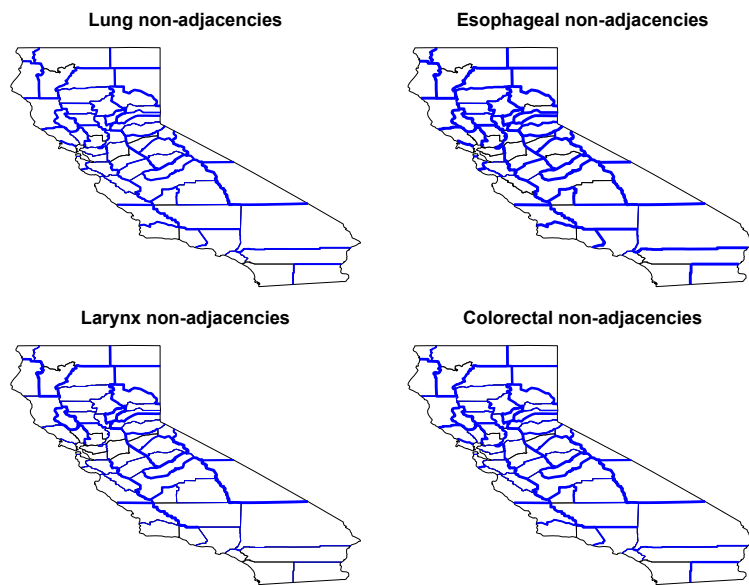


Figure 25: Non-adjacencies (shown in blue) over the California map. The thickness of the lines is proportional to the probability of being considered as a non-adjacency

F.2 Analysis with covariates in the mean with fixed adjacencies

We present inference from the model used in Section 5 of the main article, where we include cancer-specific intercepts and slopes for the three covariates described in Section 2 of the main article in the regression $\mathbf{x}_{ij}^T \boldsymbol{\beta}_j$, but exclude modeling adjacencies and keep them fixed. Table 11 presents the estimates of the model described in Section 5 including only cancer-specific intercepts in the regression model and the 3 covariates described in Section 2 of the main article in the adjacency model. The last column of Table 11 presents Monte Carlo standard errors corresponding to the parameter estimates.

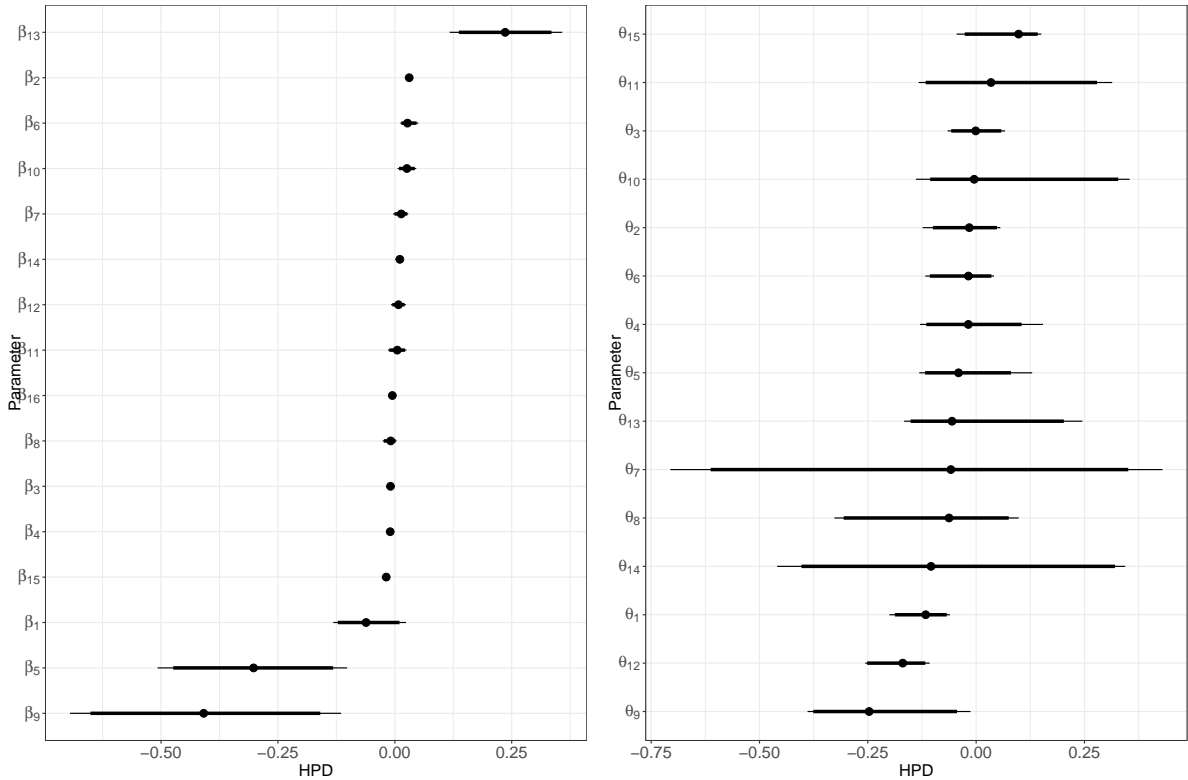


Figure 26: Highest posterior density (HPD) intervals at 90% (thick lines) and 95% (thin lines) levels for $\boldsymbol{\beta}$ (left panel) and $\boldsymbol{\theta}$ (right panel). These are ordered according to their posterior medians. As with the posterior means in Table 11, we see the intercepts regarding esophageal and larynx (β_5 and β_9) having negative posterior medians with the 95% interval entirely to the left of 0, colorectal (β_{13}) having positive posterior medians with the 95% interval entirely to the right of 0 and lung (β_1) with a much smaller negative effect with the 90% interval almost including the 0. All of the others regression coefficients have much smaller intervals with the median estimates very close to 0. Turning to the right panel, we see about 3 atoms (θ_1 , θ_9 and θ_{12}) to have their HPD intervals almost entirely to the left of 0, while none of the remaining 12 atoms (out of a total of $K = 15$) are significantly different from 0 since their 95% interval include 0. The variation in the posterior distribution of these atoms reflect substantial posterior learning and information from the data that propagates to the spatial random effects.

Table 11: Posterior estimates and standard deviations for the regression coefficients, atoms and their precision in the hierarchical model in (14). Here, β_1 through β_4 denote the regression coefficient corresponding to lung, β_5 through β_8 to esophageal, β_9 through β_{12} to larynx and β_{13} through β_{16} colorectal, respectively. The θ 's denote the atoms and τ is the precision in the prior of the θ_k 's as described in Section 3.1. While the intercepts regarding esophageal, larynx and colorectal (β_5 , β_9 and β_{13}) are significant, we note that lung intercept is not. Moreover, across cancers the smoking covariate always reveal positive estimates (β_2 , β_6 , β_{10} and β_{14}) while over 65 and below poverty covariates do not show such a consistent behavior. This indicates that the smoking covariate has a positive impact on the count means across the cancers.

Variable	Estimate	Standard deviation	Monte Carlo Standard Errors
β_1	-0.060	0.040	0.005
β_2	0.031	0.003	$< 10^{-3}$
β_3	-0.009	0.003	$< 10^{-3}$
β_4	-0.010	0.003	$< 10^{-3}$
β_5	-0.304	0.104	0.009
β_6	0.028	0.010	0.001
β_7	0.014	0.008	0.001
β_8	-0.009	0.008	0.001
β_9	-0.407	0.150	0.011
β_{10}	0.026	0.010	0.001
β_{11}	0.005	0.010	0.001
β_{12}	0.008	0.008	0.001
β_{13}	0.236	0.061	0.009
β_{14}	0.011	0.004	$< 10^{-3}$
β_{15}	-0.019	0.004	$< 10^{-3}$
β_{16}	-0.005	0.002	$< 10^{-3}$
θ_1	-0.122	0.038	0.014
θ_2	-0.019	0.045	0.013
θ_3	0.001	0.036	0.009
θ_4	-0.016	0.067	0.012
θ_5	-0.033	0.061	0.013
θ_6	-0.026	0.046	0.016
θ_7	-0.089	0.294	0.046
θ_8	-0.087	0.120	0.029
θ_9	-0.231	0.104	0.023
θ_{10}	0.038	0.137	0.054
θ_{11}	0.054	0.125	0.036
θ_{12}	-0.181	0.043	0.017
θ_{13}	-0.034	0.095	0.030
θ_{14}	-0.042	0.241	0.082
θ_{15}	0.082	0.052	0.021
τ	8.042	2.676	0.028

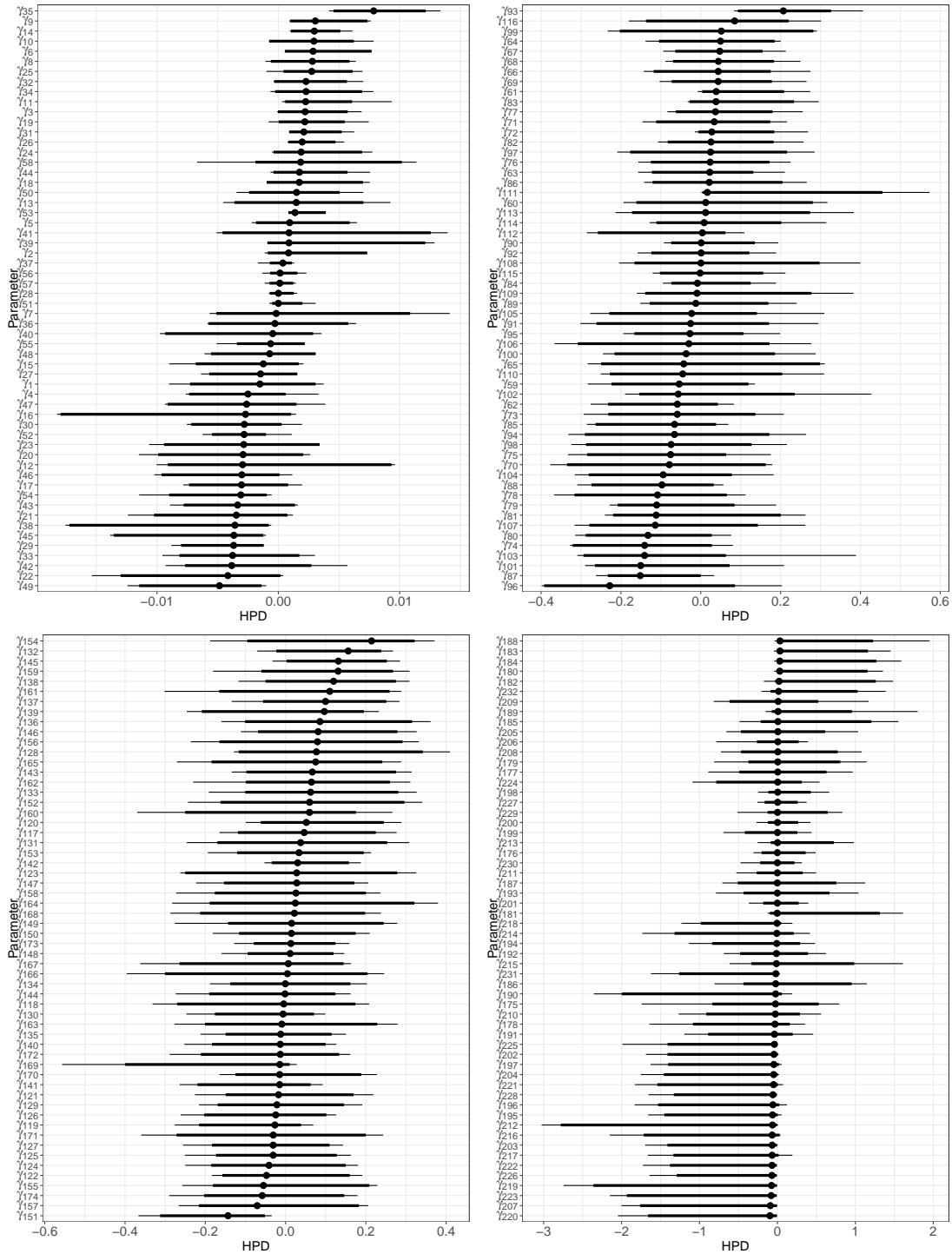


Figure 27: Highest posterior density (HPD) intervals at 90% (thick lines) and 95% (thin lines) levels for the elements of the disease-specific spatial effects in γ using the MDAGAR specification in Section 3.3.1 and the precision matrix given in Eq. 5. The four panels correspond to the 4 cancers: lung (top left), esophageal (top right), larynx (bottom left) and colorectal (bottom right). The intervals are arranged in increasing order of value for posterior medians. It is expected that the intervals for these random effects will mostly not be significantly different from 0, but they reveal substantial variation indicating enough information in the data to discern spatial patterns. It is important to note that the degree of dispersion varies significantly among different types of cancer. For example, lung cancer has the narrowest intervals, while esophageal and laryngeal cancers exhibit similar ranges. In contrast, colorectal cancer shows much wider intervals, with its medians being very close to 0.

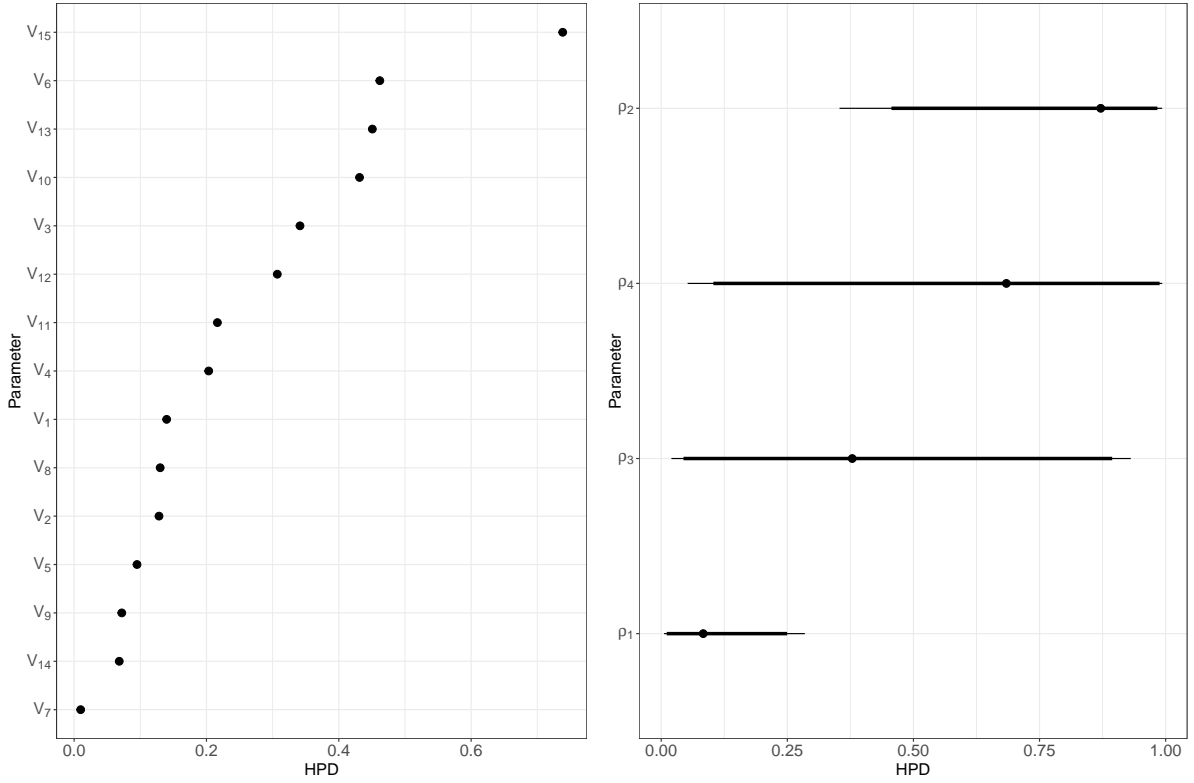


Figure 28: Highest posterior density (HPD) intervals at 90% (thick lines) and 95% (thin lines) levels for \mathbf{V} (left panel), which consists of the 15 stick-breaking weights used in Eq. (3.1), and for $\boldsymbol{\rho}$ (right panel), which consists of the 4 spatial autocorrelation parameters (one for each disease) in the MDAGAR model. These intervals are arranged in increasing order of posterior medians. The variations among these posterior intervals indicate substantial learning from the data that informs the joint distribution of the spatial effects through the stick-breaking probabilities and the baseline MDAGAR distribution in the DP. We notice that the intervals regarding \mathbf{V} are very narrow.

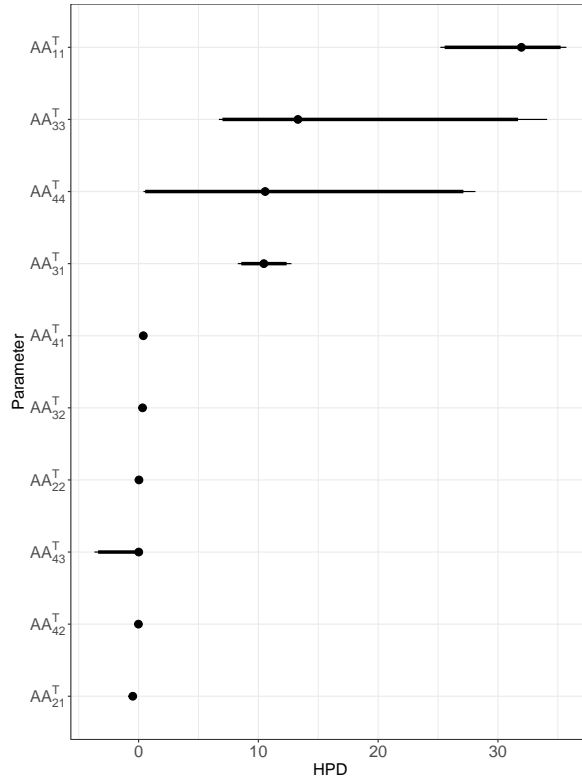


Figure 29: We provide the HPD intervals for the elements of \mathbf{AA}^T representing the non-spatial component of associations among the cancers. Lung, larynx and colorectal cancers reveal the highest variances ($(\mathbf{AA}^T)_{11}$, $(\mathbf{AA}^T)_{33}$ and $(\mathbf{AA}^T)_{44}$) with the last two having the widest intervals. Lung and larynx reveal significantly positive associations with the 95% interval for $(\mathbf{AA}^T)_{31}$ situated entirely above 0. As emphasized earlier, it is important to interpret the non-spatial component of these associations with caution, where much of the positive associations among these aggregated data are absorbed by the spatial associations arising from geographic proximity.

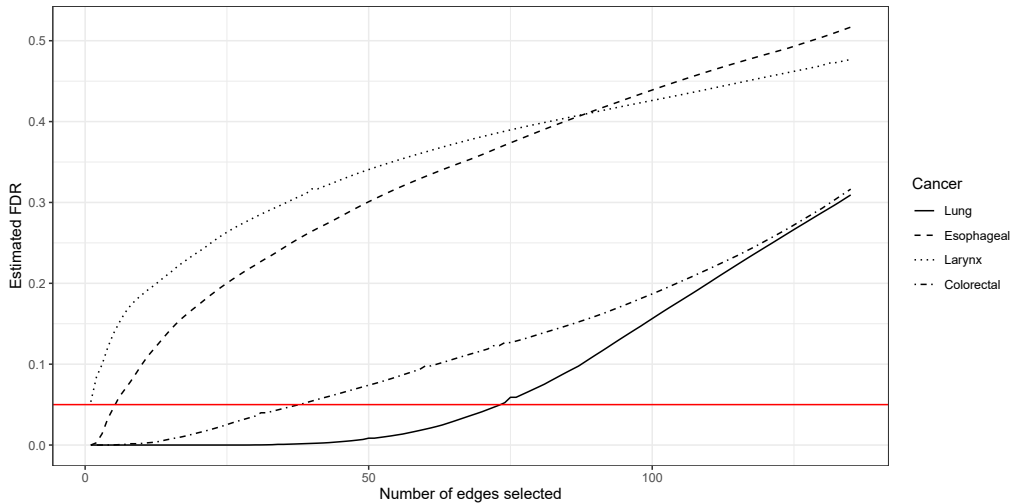


Figure 30: Estimated FDR curves plotted against the number of selected difference boundaries for four cancers

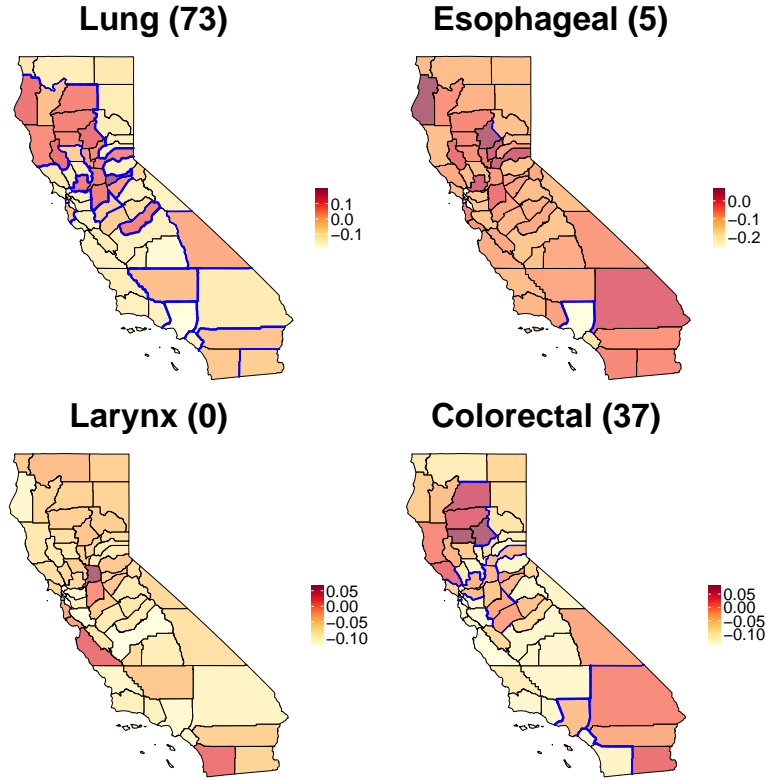


Figure 31: Difference boundaries (highlighted in red) detected by the model in the California map, colored according to the posterior mean of the corresponding ϕ_{id} , for four cancers individually when $\zeta = 0.05$. The values in brackets are the number of difference boundaries detected.

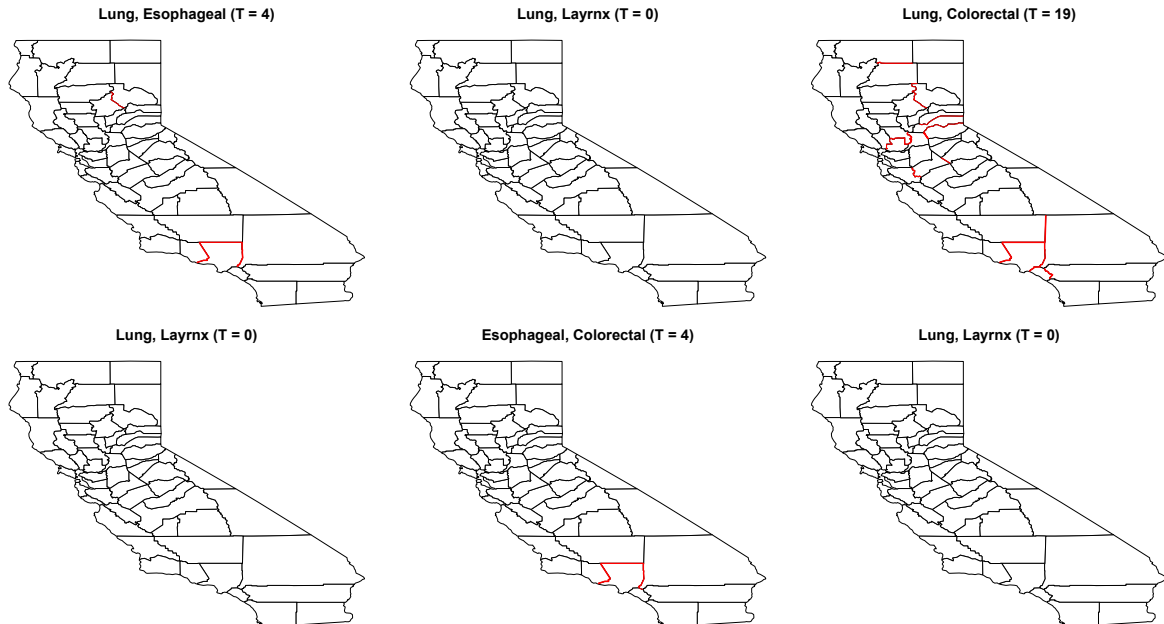


Figure 32: Shared difference boundaries (highlighted in red) detected by the model for each pair of cancers in California map when $\zeta = 0.05$. The values in brackets are the number of difference boundaries detected.

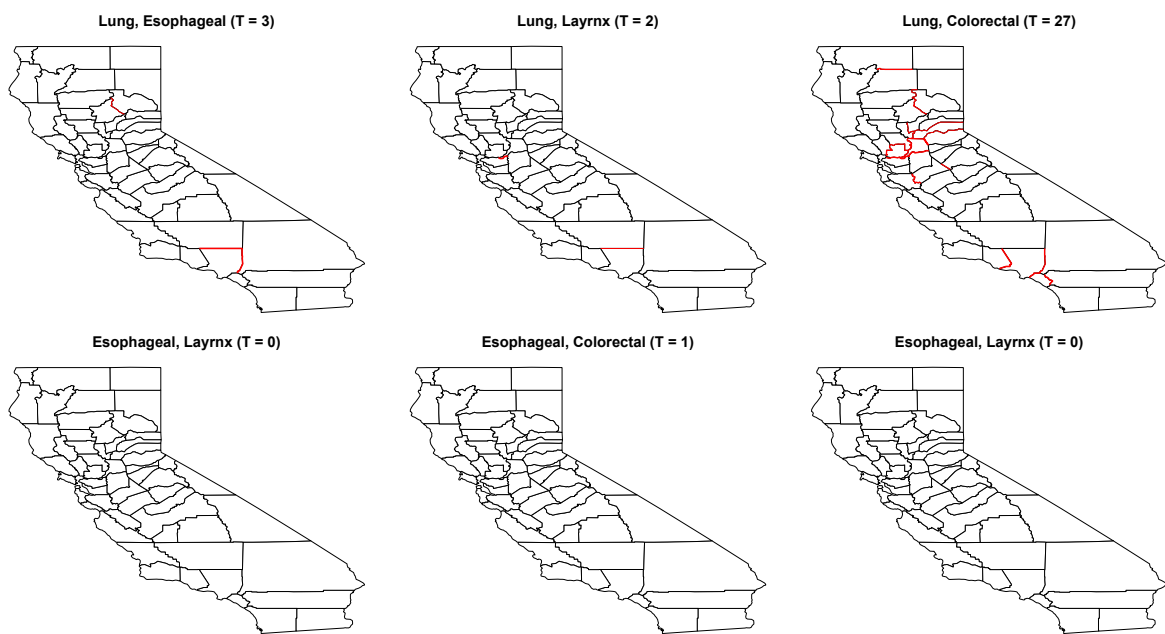


Figure 33: Mutual cross-difference boundaries (highlighted in red) detected by the model for each pair of cancers in California map when $\zeta = 0.05$. The values in brackets are the number of difference boundaries detected.